Diss. ETH No. 28556

Interfacial control of ferroic order in oxide heterostructures

A thesis submitted to attain the degree of

Doctor of Sciences of ETH Zurich
(Dr. sc. ETH Zurich)

presented by

Elzbieta Gradauskaite

MSci Chemistry and Physics, University of St Andrews

born on 02.08.1993
citizen of Lithuania

accepted on the recommendation of

Prof. Dr. Manfred Fiebig, examiner
Prof. Dr. Morgan Trassin, co-examiner
Prof. Dr. Gertjan Koster, co-examiner
Dr. Manuel Bibes, co-examiner

2022

To my mum, who is no longer here to see this.

Mamytei. Ačiū už dovanotą sėkmę lydinčią mane.

Declaration of originality

I hereby declare that the following submitted thesis is original work which I alone have authored and which is written in my own words.

Title: Interfacial control of ferroic order in oxide heterostructures

Author: Elzbieta Gradauskaite

Supervisor: Prof. Dr. Manfred Fiebig

With my signature I declare that I have been informed regarding normal academic citation rules and that I have read and understood the information on "Citation etiquette". The citation conventions usual to the discipline in question here have been respected.

Furthermore, I declare that I have truthfully documented all methods, data, and operational procedures and not manipulated any data. All persons who have substantially supported me in my work are identified in the Acknowledgement and Contributions to this thesis.

The above work may be tested electronically for plagiarism.

Zurich, 20.05.2022

Elzbieta Gradauskaite

Acknowledgements

All this work was only possible thanks to many, many people behind it, to whom I am immensely grateful.

First of all, I would like to express my gratitude to my supervisors Prof. Manfred Fiebig and Prof. Morgan Trassin. I am very thankful to Manfred for creating an exceptional environment in his group and having me be a part of it. Thank you for always giving the overarching edge to the results, finding more effective ways of communicating them, and, having infinite patience with my missing articles. I owe my deepest gratitude to Morgan for being an excellent mentor – your enthusiasm, ideas, and unconditional support made me excited for every single day of the doctorate. I will never forget how you often had more trust in my results than I did myself and never hesitated to help me in the lab. I cannot thank you enough for all the things you do for your students – acknowledging and promoting their work, making sure they are noticed and well-connected to the scientific community. Once you said "I dream of seeing success of my students" and I only hope we can live up to your expectation.

I would like to thank Prof. Gertjan Koster, Dr. Manuel Bibes, and Prof. Pietro Gambardella for being part of my thesis committee and taking their time to read this thesis. I am very grateful that they agreed to travel to participate in the thesis defense – it will be the first defense in our group held in-person since the pandemic!

I would like to recognize the invaluable input of all the collaborators that I had a chance to work with during my doctorate. A big thank you goes to Marta D. Rossell and Marco Campanini for their STEM work on our samples, which were often far from defect-free. I am very grateful to Quintin N. Meier for complementing our results with his theoretical work, specifically, for spotting the BFO homochirality in our data and getting us all excited about it. I appreciate the work performed by Natascha Gray during her master's project. I would like to also extend my acknowledgments to Banani Biswas and Christoph W. Schneider for the electrodes they designed and fabricated for our films, Thomas Moran and Bryan D. Huey for the magic of their tomographic AFM, Kasper A. Hunnestad and Dennis Meier for their atom probe tomography data, and Shovon Pal with Chia-Jung Yang for the optical conductivity measurements.

Dear Ferroics, I would like to thank every single one of you – for your friendship,

SOLA runs, pitcher nights in the alumni lounge... and the scientific discussions, of course. In particular, my heartfelt gratitude goes to everyone in the NEAT lab. Thanks to Jakob for the PLD and scanning-probe-microscopy training, to Johanna and Nives for introducing me to non-linear optics. I am grateful to Marvin for always kindly patterning my films, no matter how leaky they were. Thanks to Martin for being so caring with our PLD system and sharing joys and lows of manuscript writing. I am also very grateful to Ipek, my little BFTO sister, for diving into the complexity of Aurivillius compounds with me. Special thanks to Amadé, Lea, Ipek, Samir, Martin, Marvin, and Yannik for proofreading my thesis and everyone else contributing to the organization of my thesis defense *(read: dress shopping)*.

I was very lucky to have a big group of friends keeping me busy most of the evenings. Thanks to the IAESTE crowd for being one big family in Zurich. Thanks to my climbing partners, Janina and Scot, thanks to my past and present bouldering and hiking groups, my via ferrata (and not only) partner in crime Jenia, the girl groups, and everyone else dear – you know who you are!

I extend my gratitude to my family. *Ačiū, Šeima! Ačiū Tėveliui ir Mamytei, be jų pavyzdžio ir pagalbos niekada nebūčiau tiek daug pasiekusi. Dėkoju Pijukui už buvimą pačiu geriausiu broliu, draugu ir tiesiog giminiga siela, tiesiogine ir netiesiogine prasme. Dėkui Brigitai už tai, kad tapo tokia artima ir brangia šeimos dalimi. Merci Jutta und Beat, dass er mech in euchi familie ufgno hend.* And Quintin again, thanks for making me believe in myself as a scientist, for being my tutor in electrostatics, climbing, skiing, mountaineering, teaching me what the right amount of cheese is... and for simply existing.

Last but not least, I would like to extend my gratitude to inanimate objects that sustained me throughout my doctorate years. Thanks to Silsergipfeli and Crystal IPA du Mont Blanc. I'm grateful to Lago di Lugano, Schwyzer Voralpen, and Alpstein for being my favorite spots to recharge. Thanks to Nietsche's *"Amor Fati"* and *"Memento Mori"* of the Stoics for putting everything into perspective. And thanks to music, of course! "Tutta la vita" by Gazzelle for saving me in the time of loss. "Give me the rain" by Palace, "Brividi" by Blanco and Mahmood together with "As it was" by Harry Styles for keeping me company during the never-ending cycles of the thesis polishing.

Thank you, thank you, thank you!

Abstract

Oxide electronics have emerged as an alternative to replace the current silicon-based technology. Owing to a rich elemental composition compared to that of doped silicon, transition metal oxides can host a wide range of physical phenomena. This is especially true when oxides are integrated into ultrathin epitaxial heterostructures, in which additional properties arise from the created interfaces. Their crystal structure is, furthermore, compatible with long-range order. In particular, ferromagnetic and ferroelectric systems have gathered considerable attention due to their characteristic non-volatile response to applied external fields. While ferroic oxides are indisputable candidates for low-energy-consuming applications, there are still a few setbacks left to overcome in order to integrate them into competitive device schemes.

With the work performed during the course of this thesis, we strive to provide solutions for existing limitations to the implementation of ferroic states in nanoscale devices. We place emphasis on interfacial effects in epitaxial heterostructures and their influence on ferroic order. Making use of a non-conventional approach of epitaxially combining layers with different ferroic anisotropies, we uncover novel fundamental concepts likely to benefit the ever-evolving field of oxide electronics.

We identify the in-plane-polarized Aurivillius compounds as promising candidates for tuning interfacial electrostatics and achieving interfacial polar continuity in epitaxial hybrid heterostructures with ferroelectric perovskite oxides. The stabilized coalescent layer-by-layer growth mode ensures the single-crystallinity of these layered ferroelectrics, while the sub-unit-cell thickness control of the films enables detailed investigations of their polar state. For instance, the thickness-dependent in-plane-polarized domain configuration in the resulting epitaxial Aurivillius films prompts us to propose new means for ferroic domain and functional domain-wall engineering via structural defect ordering.

Moving ahead with the integration of Aurivillius films into perovskite-based heterostructures, we show that the Aurivillius compounds utilized as in-plane-polarized buffer layers can overcome the notorious limitation associated with the critical thickness for ferroelectricity in canonical out-of-plane-polarized perovskite ferroelectrics. We additionally demonstrate that buffers of the Aurivillius phase can be instrumental for domain and domain-wall engineering in the room-temperature multiferroic $BiFeO_3$.

In particular, we observe a uniform chirality stabilized in Néel-like domain walls in $BiFeO_3$ grown on our in-plane-polarized $Bi_5FeTi_3O_{15}$ Aurivillius layer. This likely constitutes one of the first experimental signatures of the electric counterpart to the Dzyaloshinskii-Moriya interaction in magnetically ordered compounds.

Lastly, we explore magnetoelectric phase control in heterostructures combining both ferroelectric and ferromagnetic order. In a proof-of-concept multiferroic heterostructure, we mimic magnetoelectric domain walls by inserting ultrathin ferromagnetic LSMO in between two ferroelectric layers. We show that its magnetization and conductivity can be controlled by changing polarization directions in the adjacent ferroelectric layers only. This opens up new possibilities for voltage-based tuning of magnetization and conductivity at the nanoscale.

All the effects investigated in this thesis highlight the role played by the interfaces in ultrathin complex oxide heterostructures. The results suggest that the selective tuning of interfacial polarization continuity, electrostatics, and structural discontinuities offers exciting opportunities for controlling ferromagnetic and ferroelectric order, as well as their interplay in multilayer systems for the next generation of oxide-based electronics.

Resumé

L'électronique basée sur les oxydes de métaux de transition émerge comme une alternative pour remplacer la technologie actuelle qui repose entièrement sur le silicium. En raison d'une composition élémentaire riche comparée à celle du silicium dopé, les oxydes de métaux de transition peuvent offrir un large éventail de phénomènes physiques. C'est tout particulièrement vrai lorsque ces oxydes sont intégrés dans des hétérostructures épitaxiées ultra minces, dans lesquelles des propriétés supplémentaires découlent des interfaces créées. Leur structure cristalline est, en outre, compatible avec l'établissement d'ordres à longue distance. En particulier, les systèmes ferromagnétiques et ferroélectriques ont suscité une attention considérable en raison de leur réponse caractéristique non volatile sous l'application d'un champ externe. Bien que les oxydes ferroïques représentent une opportunité incontestable pour les applications à faible consommation énergétique, il reste encore de nombreux obstacles à surmonter en vue de leur intégration dans des dispositifs compétitifs.

Avec le travail effectué au cours de cette thèse, nous nous efforçons de fournir des solutions aux limitations existantes pour l'insertion des matériaux ferroïques dans les dispositifs à l'échelle nanométrique. Nous mettons l'accent sur les effets d'interfaces dans les hétérostructures épitaxiées et leur influence sur l'ordre ferroïque. En utilisant une approche non conventionnelle consistant à combiner de façon épitaxiée des couches ayant des anisotropies ferroïques différentes, nous découvrons de nouveaux concepts fondamentaux susceptibles de bénéficier au domaine de l'électronique à base d'oxydes qui est en constante évolution.

Nous identifions les composés ferroélectriques Aurivillius, polarisés dans le plan, comme des candidats prometteurs pour moduler les effets électrostatiques aux interfaces et réaliser une continuité d'états de polarisation aux interfaces dans des hétérostructures hybrides intégrant des oxydes pérovskites ferroélectriques. Le mode de croissance couche par couche assure la monocristallinité de films minces Aurivillius, tout en rendant le contrôle de l'épaisseur des films à la demi-maille prêt possible pour permettre les études détaillées de leur état polaire. Par exemple, la configuration mise à jour au cours de cette thèse des domaines ferroélectriques polarisés dans le plan qui dépend fortement de l'épaisseur des couches minces, nous incite à proposer de nouveaux moyens

pour l'ingénierie de ces domaines ferroïques et des parois de domaines fonctionnels correspondants.

Nos progrès dans l'intégration des films Aurivillius dans les hétérostructures à base de pérovskite, démontrent que les composés Aurivillius utilisés comme couches tampons, polarisées dans le plan peuvent aider à surmonter la limitation notoire associée à l'épaisseur critique pour la ferroélectricité dans les ferroélectriques classiques tels que les pérovskites polarisées hors du plan. Nous démontrons en outre que ces couches Aurivillius peuvent jouer un rôle déterminant dans l'ingénierie des domaines et des parois de domaines dans le composé multiferroïque à température ambiante $BiFeO_3$. En particulier, nous y observons une chiralité uniforme dans des parois de domaine de type Néel lorsque la sous-couche Aurivillius est insérée. Ceci constitue probablement l'une des premières signatures expérimentales de l'équivalent électrique de l'interaction de type Dzyaloshinskii-Moriya.
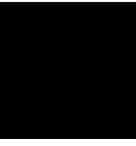
Enfin, nous explorons le contrôle d'une phase magnétoélectrique dans des hétérostructures combinant les ordres ferroélectrique et ferromagnétique. Dans une démonstration de concept basé sur une hétérostructure multiferroïque, nous reproduisons le comportement d'une paroi de domaine magnétoélectrique en insérant une couche ferromagnétique extrêmement mince de LSMO entre deux couches ferroélectriques. Nous montrons que l'aimantation et la conductivité cette paroi peuvent être contrôlées uniquement en changeant les directions de polarisation dans les couches ferroélectriques environnantes. Ceci ouvre de nouvelles perspectives pour la modulation d'états magnétiques à l'échelle nanométrique utilisant simplement une différence de potentiel.

Tous les effets étudiés dans cette thèse mettent en lumière le rôle des interfaces dans les hétérostructures d'oxydes ultra minces. Les résultats suggèrent que l'ingénierie de la continuité de la polarisation aux interfaces, les effets électrostatiques et l'impact des discontinuités dans la structure cristalline offrent des opportunités excitantes pour contrôler les ordres ferroïques et leur interaction dans les systèmes multicouches pour la prochaine génération d'électronique à base d'oxyde.

Contents

Introduction

The ever-increasing energy consumption of electronic devices and requirements for progressively more computing power are pushing the current silicon-based technologies beyond their capabilities. While functional elements in complementary metal oxide–semiconductor (CMOS) devices are in the process of being continuously miniaturized, the voltage required to operate them has already reached the lowest limit attainable[1,2]. This calls for alternative beyond-CMOS device platforms[3], which could offer superior energy efficiency, scalability, and non-volatility.

Electronics based on transition-metal oxides[4,5] have emerged as a viable option owing to the plethora of tunable phenomena they host, which, in turn, leads to numerous potential applications. This can be explained by the elemental diversity of oxide electronics, which may contain the majority of elements on the periodic table, unlike the Si-based electronics limited to group III–V elements. The properties of transition-metal oxides are often dictated by electrons (or lack thereof) in their d- and f-orbitals[6], which display strong interactions and can enable superconductivity, ionic conduction, ferromagnetism, or ferroelectricity. The interest in oxide electronics was additionally fueled by the research on oxide interfaces[7] that were shown to host novel effects not observed in the bulk.

Ferroic oxides are at the forefront of the research dedicated to oxide electronics[8,9]. Their energetically degenerate ferroic states can be interchangeably switched in a non-volatile fashion, making them attractive for data storage and logic devices characterized by low energy consumption. While originally envisioned as stand-alone device platforms in the form of magnetic hard-disk drives[10] or ferroelectric random access memories[11,12], now ferroic oxides are more commonly considered as the key components of spintronic memories[13–16], electroresistance-based tunnel junctions[17], memristors[18,19] as well as magnetoelectric spin-orbit logic elements[20,21]. To achieve this, ferroic oxides have to be prepared in the thin-film form and integrated into epi-

taxial heterostructures.

Despite the big strides in thin-film deposition and characterization achieved over the last few decades, the use of ultrathin ferroic films is still hindered by a few remaining setbacks. These functional materials suffer from surface dead layers, the lack of control over ferroic domain formation, fatigue and retention problems with increasing cycles of usage, instability of functional elements, as well as weak coupling between different ferroic orders. This thesis attempts to provide at least partial solutions to these problems by exploring interfacial effects in epitaxial heterostructures based on complex ferroic oxides. We investigate electrically and magnetically ordered ferroic layers by tracking their structural and symmetry-dependent properties during their thin-film epitaxial design. A variety of additional methods characterizing the film functionality are performed post-deposition. While highlighting ways of optimizing their functionality, we uncover unprecedented device-related and fundamental concepts.

Chapter 2 covers the necessary scientific background related to ferroic oxides, domains, domain walls, and ferroic thin-film integration into epitaxial heterostructures. **Chapter 3** introduces experimental and theoretical methods utilized for investigations centered around ferroic-oxide heterostructures. We place emphasis on in-situ second harmonic generation and piezoresponse force microscopy, which are the core experimental techniques of this thesis.

In **Chapter 4**, we introduce the epitaxial growth of single-crystalline in-plane-polarized thin films of the Aurivillius phase using pulsed laser deposition. We demonstrate that the films of $Bi_{n+1}Fe_{n-3}Ti_3O_{3n+3}$ homologues exhibit sub-unit-cell ferroelectricity accompanied by unmatched fatigue resilience. In ultrathin layers, we uncover the formation of unusual charged domain walls, which we further analyze in **Chapter 5**. This leads us to establish new means for domain engineering in anisotropic in-plane ferroelectrics and ferromagnets, whereby their domain size and domain-wall positions can be predefined by the substrate surface morphology.

Having established the high-quality growth of the Aurivillius thin films and the control of their ferroelectric properties, we proceed with their integration into hybrid epitaxial multilayers. **Chapters 6** and **7** explore heterostructures that combine the in-plane-polarized Aurivillius layers and the out-of-plane-polarized classical perovskite ferroelectrics. In **Chapter 6**, by inserting the in-plane-polarized Aurivillius buffer we eliminate critical thickness for ferroelectricity in the out-of-plane-polarized $BaTiO_3$ film, setting the stage for metal-free ferroelectric device paradigms. In **Chapter 7**, we investigate how the in-plane-polarized Aurivillius layers influence the domain configurations in the multiferroic $BiFeO_3$ film. We find that the buffer sets not only the allowed domain states in the film but also the chirality of $BiFeO_3$ domain walls. We demonstrate that the high-quality epitaxial hybrid heterostructures of the perovskite and Aurivillius phases host polar homochirality, which might be an experimental signature

of the recently proposed electric counterpart to the Dzyaloshinskii-Moriya interaction in magnetically ordered systems.

Lastly, in **Chapter 8**, we use our accumulated understanding of interfacial effects in oxide thin films to explore magnetoelectric coupling in multiferroic heterostructures. In a proof-of-concept study of artificial magnetoelectric domain walls that we create through interfacial charge coupling, we show that magnetization and conductivity of the $La_{0.7}Sr_{0.3}MnO_3$ functional elements can be deterministically tuned with polarization directions of the adjacent ferroelectric layers, providing new insights into the control of magnetization and conductivity in oxide-based heterostructures.

Chapter 9 contains the summary and outlook of the results provided in this thesis.

Ferroic thin films

Parts of this chapter are published as:

- N. Strkalj, E. Gradauskaite, J. Nordlander and M. Trassin. Design and Manipulation of Ferroic Domains in Complex Oxide Heterostructures. *Materials* **12**, 3108 (2019). [22]

- E. Gradauskaite, P. Meisenheimer, M. Müller, J. Heron, M. Trassin. Multiferroic heterostructures for spintronics. *Physical Sciences Reviews* **6**, 20190072 (2021). [23]

This chapter provides a brief introduction to ferroic order in oxide thin films and the scientific background necessary to describe the results of this thesis, presented in Chapters 4 to 8. We begin by recalling the definition of ferroic order, putting emphasis on magnetically and electrically ordered ferroics (Sec. 2.1). We then discuss the formation of ferroic domains (Sec. 2.2) and the resulting types of domain walls (Sec. 2.2). Lastly, we explore degrees of freedom for the control exerted over the two types of ferroic order in our epitaxial heterostructures (Sec. 2.5). The chapter is primarily based on the textbooks referenced as [12,24–27].

2.1 Ferroic materials

Ferroic crystals are defined by a special phase transition, during which the point-group symmetry of the crystal changes. This transition takes place at the transition temperature denoted as the Curie temperature T_C. Below this temperature, the lowered symmetry of the ferroic crystal leads to the emergence of a long-range macroscopic property of interest, referred to as order parameter or spontaneous property, see Figure 2.1a. Ferroic materials possess at least two orientational variants of the order
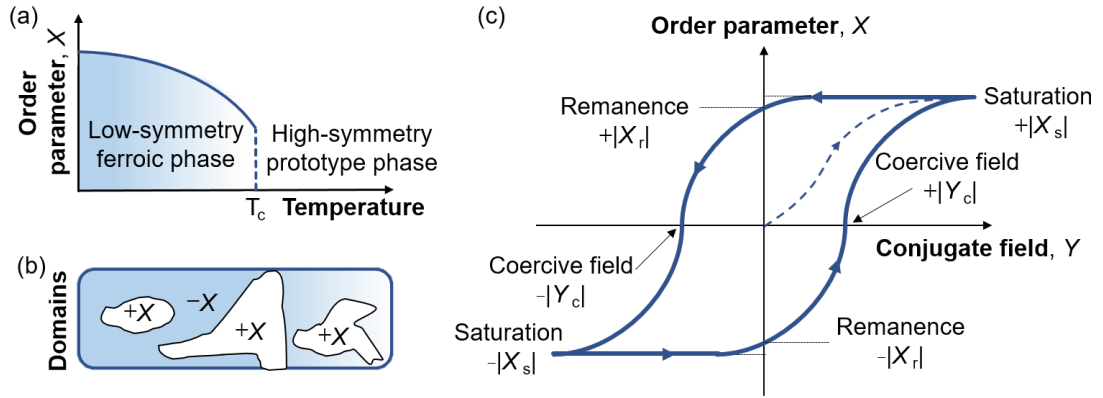
Figure 2.1: Properties of ferroic crystals. (a) Illustration of the phase transition close to T_C from high-symmetry prototype phase to ferroic low-symmetry state with an order parameter. (b) Visualization of ferroic domains in a ferroic crystal. (c) Hysteretic behavior of a ferroic under an applied conjugate field.

parameter that are energetically degenerate. Regions with a uniform order parameter are called domains (Fig. 2.1b), and one can switch the order parameter using a specific external field, referred to as the conjugate field.

A ferroic order can be characterized by its hysteretic behavior with respect to the conjugate field, as shown in Figure 2.1c. A hysteresis in ferroic crystals arises due to the energy barrier defined by the coercive field, which has to be overcome for the order parameter to reverse. By increasing the field past this coercive field, one achieves the saturation, associated with a uniform order across the entire crystal. Even when the field is removed, ferroics maintain a non-zero net value of the order parameter in their remanent state, the sign of which is dependent on the history of the sample. Most importantly, this sign (direction) can be used as an information bit for binary data storage, making ferroics particularly attractive for non-volatile memory applications. In addition to ferroic phases, antiferroic phases are also present. Antiferroic materials are characterized by the coexisting ferroic sublattices of the same order parameter that compensate each other.

Ferroic order	Ferromagnetic	Ferroelectric	Ferroelastic	Ferrotoroidic
Order parameter	Magnetization $\vec{M}$	Polarization $\vec{P}$	Strain $\vec{\sigma}$	Toroidization $\vec{T}$
Conjugate field	Magnetic field $\vec{H}$	Electric field $\vec{E}$	Stress $\vec{\varepsilon}$	Ferrotoroidic field $\vec{S}$

Table 2.1: Classes of ferroic crystals and the associated order parameters and conjugate fields.

There are four different classes of ferroic order: ferromagnetism, ferroelectricity,

ferroelasticity, and ferrotoroidicity. Table 2.1 lists all these with their corresponding order parameters and conjugate fields. This thesis will focus on ferroelectrics and ferromagnets. We will also consider multiferroic materials, with both (anti)ferromagnetic and ferroelectric orders occurring in the same phase.

2.1.1 Ferroelectrics

Ferroelectrics are electrically ordered ferroics with a non-zero electric polarization in the absence of external electric fields. They are non-centrosymmetric ionic solids that are insulating. The ferroelectric order parameter can arise when positively charged ions are off-centered with respect to those that are negatively charged. This creates a local electric dipole, which over the volume sums up to a net polarization. The spontaneous polarization $\vec{P}$ in ferroelectrics must be switchable by an applied electric field $\vec{E}$.
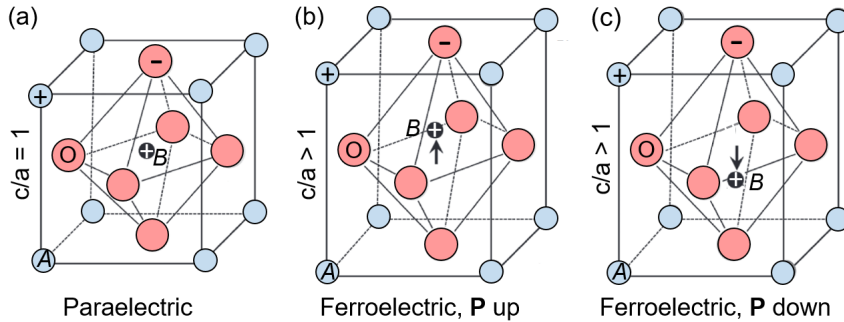
Figure 2.2: Crystal structure of a displacive ferroelectric above and below T$_C$. (a) High-temperature paraelectric, cubic phase. (b,c) Low-temperature ferroelectric, tetragonal phase with polarization pointing up (b) and down (c).

Displacive ferroelectricity is the most widespread mechanism leading to the emergence of spontaneous polarization. A perovskite crystal structure of the general formula ABO_3 is adopted by the majority of ferroelectric oxides. The ideal perovskite cubic structure has the B cation in an octahedral cage of oxygen anions, while the A cation is coordinated by twelve oxygen anions, as shown in Figure 2.2a. Cubic unit cells are characteristic of the paraelectric, high-symmetry phase, which ferroelectric perovskites commonly exhibit above T$_C$. Upon going through the phase transition, the unit cell loses the center of inversion. This takes place through atomic displacements, with that of the B cation being the most prominent one; it moves with respect to the oxygen octahedron and gives rise to a spontaneous polarization. For instance, the movement upwards leads to the up polarization (Fig. 2.2b) and the movement downwards to the down polarization (Fig. 2.2c). These two states are degenerate in energy. The B cation displacement towards one of the oxygen apexes lowers the energy of the system due to

the hybridization of the electron clouds that belong to the B cation and the oxygen ion that are now in close proximity. Additionally, these atomic deformations result in a tetragonal elongation of the unit cell ($c/a > 1$). The loss of inversion symmetry in ferroelectrics is critical in the context of this thesis: broken inversion symmetry enables optical second harmonic generation in the material, which allows tracking polarization with non-linear optics, see section 3.1.3.

2.1.2   Layer polarization in perovskite oxides

The recent developments in thin-film growth and characterization have led to the introduction of the concept of layer polarization[28]. Appreciable layer polarization can develop in uniformly oriented epitaxial crystals that are made up of charged planes in which ionic charges do not cancel out. Unlike spontaneous polarization, layer polarization is not switchable in external electric fields and is not solely restricted to ferroelectric crystals; layer polarization can develop in centrosymmetric compounds, too.

Let us consider a (001)-oriented perovskite film of general formula ABO_3 as shown in Figure 2.3a. The film consists of alternating AO and BO_2 atomic planes. If both A and B cations carry an ionic charge of $+3$ (e.g. $Bi^{+3}Fe^{+3}O^{-2}_3$ (BFO)), then AO and BO_2 planes have formal charges of $+1$ and -1, respectively. These charges are localized to the atomic planes. If the layer growth starts with the BO_2 layer and ends with the AO surface termination, the top interface has a positive charge, while the bottom interface is negatively charged, leading to the so-called layer polarization in the films (Fig. 2.3b).
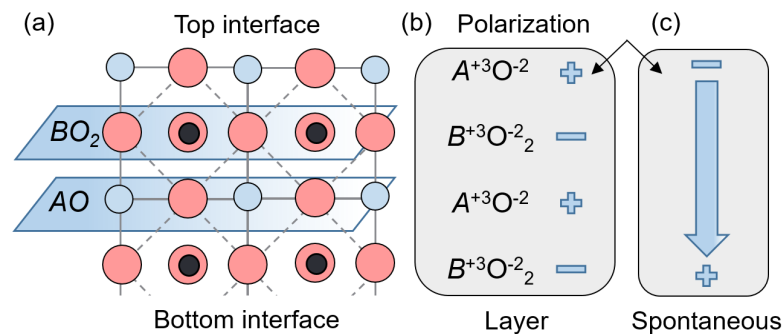
Figure 2.3: Crystal structure of layer charges in a perovskite giving rise to layer polarization. (a) Alternating ionic charges at the AO and BO_2 atomic planes in (001)-oriented crystalline film. This leads to layer polarization shown in (b). (c) If the crystal also possesses an out-of-plane-oriented spontaneous polarization, it will be oriented so that its surface-bound charges are screened by the charges of layer polarization at the bottom and top surfaces.

In films that are a couple of nanometers in thickness, the contribution of layer

polarization can significantly affect the spontaneous polarization. Its direction will be oriented so that the surface-bound charges can be screened by the charge localized at the top and bottom atomic planes, see Figure 2.3c. The understanding of layer polarization enables the selection of either upwards or downwards oriented polarization in the film that has charged planes by switching between its AO and BO_2 surface terminations[28–31]. This can be achieved by growing ferroelectric films on chemically etched substrates that have a defined surface termination[32]. Ferroelectrics with neutral planes such as $Ba^{+4}Ti^{+2}O^{-2}_3$ (BTO) have no layer polarization, but their polarization can still be controlled in a deterministic way through the use of a buffer layer that has charged planes. A commonly used metallic, non-polar $La_{0.7}Sr_{0.3}MnO_3$ (LSMO) buffer is made up of charged planes and, therefore, has a layer polarization. Even though it is a metal, the bound charge on its atomic planes is not fully compensated due to the existence of a screening length[33]. Its AO termination results in a positively-charged interface enforcing an upwards BTO polarization. When BO_2-terminated, in contrast, it directs the BTO polarization downwards. If both the ferroelectric film and its buffer layer exhibit a layer polarization, as is the case for LSMO and BFO, one has to consider the net charge at the interface for understanding the direction of polarization in the film.

2.1.3 Ferroelectric fatigue

The use of ferroelectrics in non-volatile memory devices relies on their spontaneous polarization to be able to withstand numerous switching cycles. In contrast to the magnetization of a ferromagnet, the polarization of a ferroelectric suffers from fatigue, which signifies a decrease in the switchable polarization with an increasing number of poling cycles[11,12]. Typically, the switchable polarization in capacitors decreases to half of its original value after as few as 10^6 cycles[11]. Charged defects in ferroelectrics are usually highlighted as the principal cause of ferroelectric fatigue. Point defects such as oxygen vacancies usually are limited to the film surface but get redistributed through the film volume upon polarization cycling. Their charges distort oxygen octahedra[34] and pin domain walls[35], which results in self-polarized regions that can no longer be switched upon voltage application[36,37]. The switchable polarization, as a result, is continuously decreasing until it ultimately gets completely suppressed. Some families of layered ferroelectrics[38], however, were demonstrated to have superior fatigue-resilience and hold promise for ferroelectric-based devices. In this thesis, the Aurivillius-phase[39] ferroelectrics will be investigated for their fatigue-free performance[38].

2.1.4   Finite-size effects in ferroelectric thin films

In order to integrate ferroelectrics into devices, they have to be prepared in the epitaxial thin-film form. However, when the dimensions of ferroelectrics are reduced down to the nanometer scale their observed properties start deviating from those known for the bulk crystals[30,40]. In uniformly out-of-plane-polarized films, bound charges are accumulating at the surfaces. When these surface-bound charges are not effectively screened by external charge carriers (e.g. charged defects, metal electrodes, or layer polarization) they create an electric field oriented opposite to the polarization referred to as the depolarizing field. With decreasing thickness, surface charges start playing a decisive role as surface contributions become dominant. In line with this, in very thin films the value of polarization is reduced by the depolarizing field[30]. In extreme cases where the film thickness is reduced below its so-called critical thickness for ferroelectricity, the depolarizing-field effects prevent the phase transition to the ferroelectric state entirely[30,41,42]. This can be rationalized by how the relevant energy costs are related to the sample dimensions. The energy that the system loses when the crystal remains paraelectric is proportional to its total volume, while the energy gained by not having to fight the depolarizing field is dependent on the surface charges, hence the surface area. This is why the films that are just a few unit cells in thickness but have large surface areas usually remain non-polar, giving rise to a critical thickness for ferroelectricity[30,41,42] in thin films. Finding strategies to stabilize a ferroelectric behavior in the ultrathin regime has been a long-standing challenge, which will also be addressed in this thesis.

2.1.5   Ferromagnets

Ferromagnets are magnetically ordered ferroics that possess non-zero magnetization even in absence of applied magnetic fields. While ferroelectrics are associated with the broken inversion symmetry, ferromagnets break the time-reversal invariance. In ferromagnets, magnetic moments are aligned parallel to one another, which lowers the energy of the system due to exchange interactions. This gives rise to the ferromagnetic order parameter referred to as spontaneous magnetization $\vec{M}$, which is switchable by an applied magnetic field $\vec{H}$. The most fundamental exchange interaction is the direct magnetic exchange. It describes the exchange between localized spins and involves overlap integrals of the atomic wave-functions, yielding a lowered energy in ferromagnets once their spins align. In ferromagnetic oxides, however, the magnetic ions are further away from each other. Metal ions are usually separated by a diamagnetic oxygen atom, which prevents the direct wave-function overlap and hence the direct exchange. Instead, long-range interactions, such as superexchange or double exchange are used to describe the magnetic order.
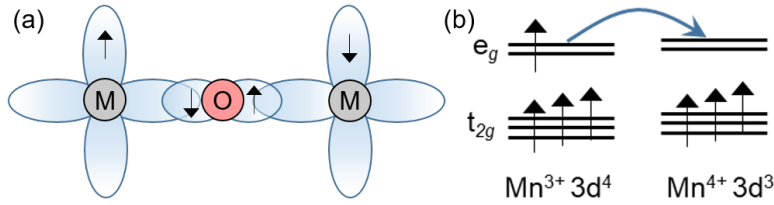
Figure 2.4: Long-range magnetic interactions in transition-metal oxides. (a) Superexchange. (b) Double-exchange interaction.

Superexchange occurs when the interaction between non-neighboring magnetic ions is mediated by the orbital overlap through the non-magnetic ion in between them. For instance, if transition-metal ions have one unpaired d-electron each, they can overlap with a filled outermost p-orbital of the oxygen ion, see Figure 2.4a. If the two metal ions have anti-parallel spins, the electron delocalization in the structure lowers the energy of the system. If the spins are parallel, such delocalization is prevented by the exclusion principle. Hence, in most cases, the superexchange interaction leads to antiferromagnetic order.

Double exchange can occur if magnetic ions exhibit different valence states. For instance, Mn^{3+} and Mn^{4+} have 4 and 3 d-electrons, respectively. The energy of the system with these two ions can be lowered by the inter-atomic transfer of the single spin in the higher-lying e_g orbital, see Figure 2.4c. This, however, can only occur if the two ions have their spins aligned parallel so that the high-spin state is maintained upon the electron transfer. As a result, the double exchange usually leads to ferromagnetism in oxides.
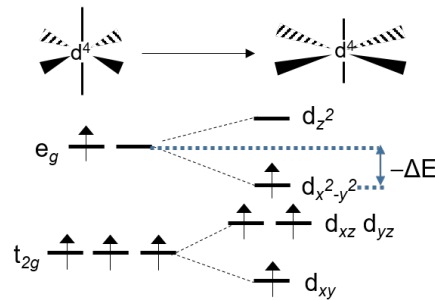
Figure 2.5: The Jahn-Teller effect for a d^4 ion. The oxygen octahedral cage distorts tetragonally to lower the energy of the higher-lying unpaired electron.

Lastly, the Jahn-Teller effect is related to the crystal field in perovskites and can also influence their magnetic order. It arises in high-spin d^4 and low-spin d^7 or d^9 octahedral compounds and manifests as a spontaneous tetragonal elongation or compression of a unit cell. It lowers the energy of the system for that one particular electronic configuration and, therefore, suppresses electron hopping from one ion to the

other[43] leading to insulating behavior and charge ordering in magnetic systems[44]. A similar tetragonal distortion of oxygen octahedra is also observed in ferroelectrics (see Fig. 2.2), but as they usually have no unpaired d-electrons the effect is called second-order (pseudo) Jahn-Teller distortion[45].

2.2 Domains and domain formation

Preserving ferroelectric and ferromagnetic order long-range in the absence of external fields is energetically costly, which leads to the formation of domains – regions with a uniform orientation of the relevant order parameter. This takes place to minimize electrostatic and magnetostatic energy, respectively. In ferromagnets every domain can be viewed as a macroscopic magnetic dipole with very high dipolar energy: the high density of magnetic stray field lines at the sample edges (Fig. 2.6a) is energetically costly and triggers the so-called demagnetizing field. This demagnetizing field gives rise to the formation of domains with oppositely oriented magnetization within the sample. This minimizes the dipolar energy and, hence, suppresses the stray field lines at the surface, see Figure 2.6b. A special domain configuration, shown in Figure 2.6c, is called flux-closure domains, which eliminates the dipolar energy completely. Domain formation, nonetheless, is not so easy to predict, as domain wall creation itself costs energy. In addition, many ferromagnets possess easy magnetization axes due to magnetocrystalline anisotropy. Therefore, the domain formation is dictated by a delicate energy balance, reflected in the Landau-Lifshitz-Kittel scaling law[24], which states that the domain width is proportional to the square root of film thickness.

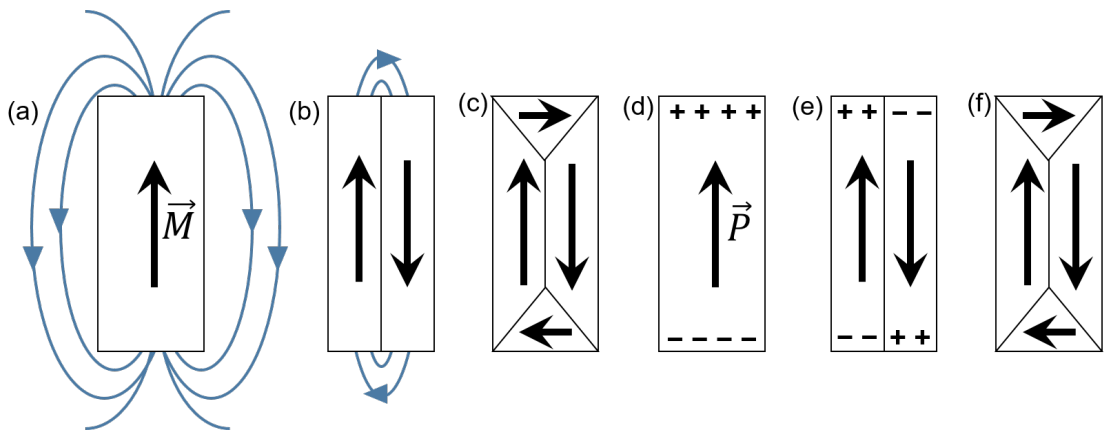**Figure 2.6: Domain formation in ferromagnets and ferroelectrics.** In ferromagnets: (a) single domain, (b) 180° domains and (c) flux-closure domains. In ferroelectrics: (d) single domain, (e) 180° domains and (f) flux-closure domains.

The ferroelectric domains sometimes take a similar shape as their magnetic counterparts, but, in contrast to ferromagnetic domains, their formation is driven by stray

fields arising from non-screened surface-bound charges (Fig. 2.6d). A net surface-charge accumulation can be commonly minimized by the formation of 180° domain walls, see Figure 2.6e. Flux-closure domains that eliminate bound charges completely are, however, rarely observed (Fig. 2.6f). This is because polarization exerts a directional lattice distortion and is related to the elastic strain in the system. Therefore, non-180° ferroelectric domain walls usually create significant strain fields that cannot be accommodated in some crystal lattices unless dislocations, cracks, or voids are introduced to the crystal. Epitaxial strain in thin ferroelectric films also plays a decisive role by imposing a uniform strain from the substrate and hence selecting allowed polarization directions. Lastly, it is worth noting that in ferroelectrics, unlike in ferromagnets, the surface polarization charges can be screened externally with charged defects and impurities or even layer polarization (see section 2.1.2) offering an alternative pathway to the stabilization of domain patterns, that would otherwise be too costly energetically.

2.3 Domain walls

Domain walls are 2D-like objects separating regions of different order parameter orientations. This zone, in which the order parameter has to reorient, cannot be described by any of the discrete points in the order-parameter space. Domain walls can be as narrow as a few nanometers (this is especially true for ferroelectrics) and have anomalous properties compared to the rest of the bulk matrix, enabling domain wall nanoelectronics.

2.3.1 Domain wall types
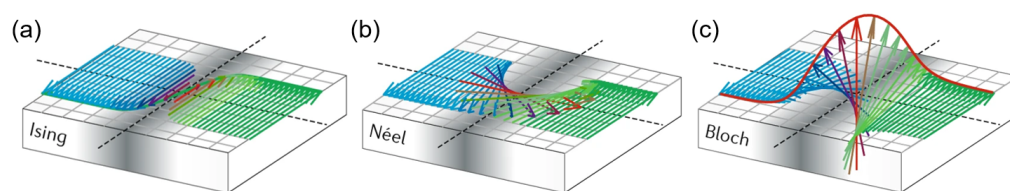
Figure 2.7: Domain wall types. (a) Ising type, (b) Néel type, (c) Bloch type. Reprinted with permission from[46]. Copyright (2020) Springer US.

The domain wall type is determined by the path that the order parameter adopts between two domains. In Ising walls, the order parameter does not reorient but vanishes and then reemerges in the opposite direction, as shown in Figure 2.7a. Néel walls are defined by the order-parameter rotation in the plane perpendicular to the domain wall, see Figure 2.7b. In Bloch walls, in contrast, the order parameter rotates

in the plane parallel to the domain walls, see Figure 2.7c. Bloch walls are commonly encountered in bulk ferromagnets, while Néel walls are preferred in very thin ferromagnetic films, where the shape anisotropy enforces in-plane magnetization. Ferroelectric walls have been traditionally thought to be Ising-like, due to the lattice-polarization coupling and high elastic-energy costs of polarization rotation. Nevertheless, an increasing number of reports are now showing that ferroelectric domain walls can also exhibit Bloch or Néel character. Understanding the internal structure of domain walls is critical as it can define the switching mechanisms in ferroic thin films[47].

2.3.2 Charged ferroelectric domain walls
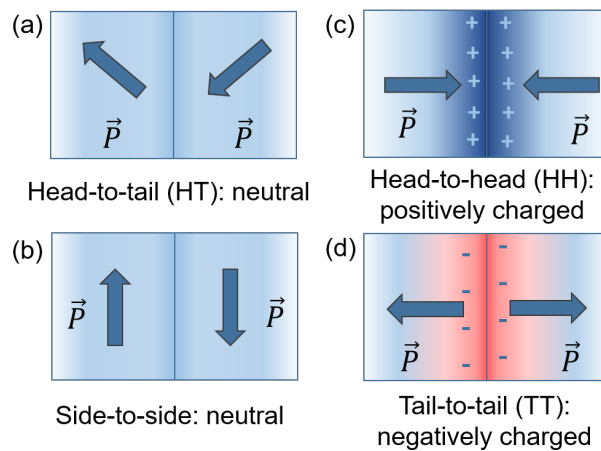
Figure 2.8: Neutral and charged ferroelectric domain walls. (a) Head-to-tail, (b) side-to-side, (c) head-to-head, and (d) tail-to-tail.

Domain walls in ferromagnets have been long investigated owing to their potential for race-track memories[48]. Magnetic domain walls with uniform chirality, so-called homochiral domain walls, exhibit deterministic motion upon external-field application[47]. Ferroelectric and multiferroic domain walls, in contrast, have only received more attention very recently[49] when they were found to have different conduction properties than the bulk[50]. Ferroelectric walls are generally narrower (by 1-2 orders of magnitude[51]) than their magnetic counterparts because of the high energy of a reorienting polarization. The divergence of polarization at the walls can enable anomalous properties. Seminal work on the domain-wall functionality uncovered the exotic conductivity at charged domain walls, first measured in BFO[50]. Altered conductivity of domain walls can be associated with intrinsic changes, such as shifts of the valence and conduction bands at the charged domain walls, as well as the extrinsic accumulation of mobile screening charge carriers there[49,52,53]. While head-to-tail (Fig. 2.8a) or side-by-side walls (Fig. 2.8b) are neutral and exhibit no changes in conduction, head-to-head (HH) walls possess an accumulation of positive bound charges (Fig. 2.8c) and tail-to-tail

(TT) walls have a surplus of negative bound charges (Fig. 2.8d). These bound charges attract extrinsic screening carriers, making the conductivity of HH and TT walls different from that of the surrounding bulk material[53] and, hence, of interest for device applications, such as domain-wall nanocircuitry[54].

2.4 Selected materials

In this thesis, we investigate a variety of ferroic oxide thin films. Among the ferroelectric materials, we select the in-plane-polarized layered ferroelectrics of the Aurivillius phase and canonical perovskite oxides: out-of-plane polarized $BaTiO_3$ and multiferroic $BiFeO_3$. We explore how the unconventional epitaxial combination of these polar phases can lead to improved and novel functionalities. Metallic $La_{1-x}Sr_xMnO_3$ is selected as a model ferromagnet based on its rich phase diagram.

2.4.1 Aurivillius phases
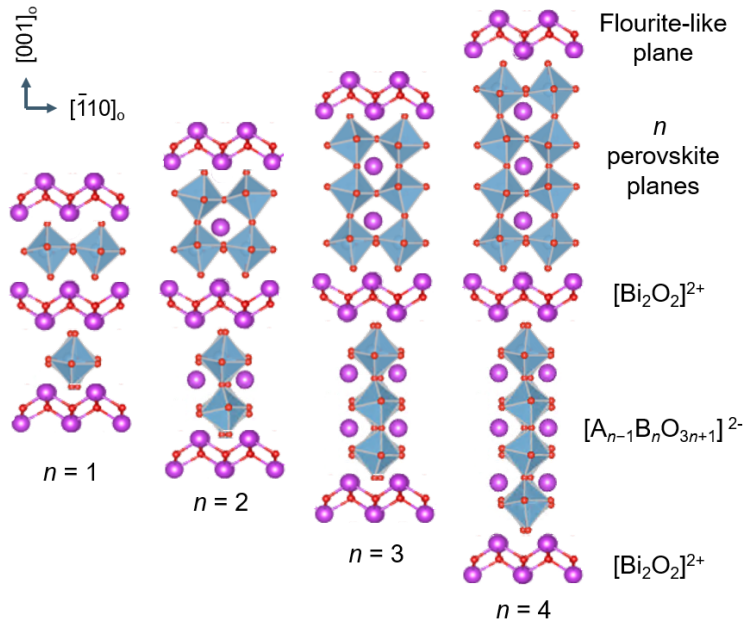
Figure 2.9: Crystal structure of layered Aurivillius ferroelectrics. Prototypical unit cells are shown for homologues with n=1,2,3,4.

Aurivillius compounds are layered ferroelectrics with $Bi_2A_{n-1}B_nO_{3n+3}$ as empirical formula, where A and B are differently sized 12- and 6-coordinated cations, respectively[39,55]. Their orthorhombic unit cell is made up of alternating layers of a variable number n of perovskite-octahedra planes interleaved between fluorite-like $[Bi_2O_2]^{2+}$

layers along the c-axis (corresponds to the out-of-plane component in the films), see Figure 2.9.

Aurivillius compounds are mostly renowned for their fatigue resilience[38], as their crystal structure can convert detrimental charged defects into structural defects, which do not affect their switching properties. For instance, in response to synthesis-related off-stoichiometry, the crystal structure forms out-of-phase boundaries[56,57] (i.e. crystal stacking faults) to preserve the charge neutrality of the system. Additionally, Bi can accommodate different formal ionic charges and therefore can create additional bonds in the flourite-like layer to bypass any charge imbalances[56].The highly anisotropic unit cell of Aurivillius compounds leads to unusual polar anisotropy[58]: in n=even compounds, polarization is restricted to the in-plane a-axis only, while n=odd compounds have additionally allowed c-component. As lead-free materials with high T_C values[55,59,60], they are attractive for device applications. However, the achievement of epitaxial single-crystalline Aurivillius films has long remained elusive.

Among the Aurivillius compounds, the $Bi_{n+1}Fe_{n-3}Ti_3O_{3n+3}$ (BFTO) homologous series[61–64] is one of the most studied families. The interest in BFTO thin films has been fueled by the potential they hold for room-temperature multiferroic device applications[65,66]. This motivates our choice of BFTO as our model system of the Aurivillius phase for this thesis.

2.4.2 BaTiO$_3$ (BTO)

BTO is a classical perovskite ferroelectric. It exhibits displacive ferroelectricity with a polar tetragonal unit cell at room temperature, identical to that shown in Figure 2.2. In thin coherently strained films, the BTO is already polar at deposition temperature[30,67] and, when c-oriented, the films can only be either upwards polarized or downwards polarized. As BTO has no charged planes, the charged surface termination of a buffer determines the polarization orientation of the pristine film.

2.4.3 BiFeO$_3$ (BFO)

BFO is likely the most investigated perovskite multiferroic. Not only does it have a strong polarization of up to 130 μC cm^{-2}[68,69], but it also has an antiferromagnetic order coupled to it. Its antiferromagnetic order is described by an incommensurate cycloidal modulation, i.e. spin cycloid[70], arising from the antisymmetric exchange interaction, called the Dzyaloshinskii–Moriya interaction (DMI). This results in a canted magnetic moment, which, unfortunately, over the cycloid periodicity mostly cancels out, making it too weak for device applications. However, if a ferromagnet is deposited

on top of the BFO film, one can achieve exchange coupling between the antiferromagnetic and ferromagnetic orders, enabling electric-field control of magnetization[71–73].
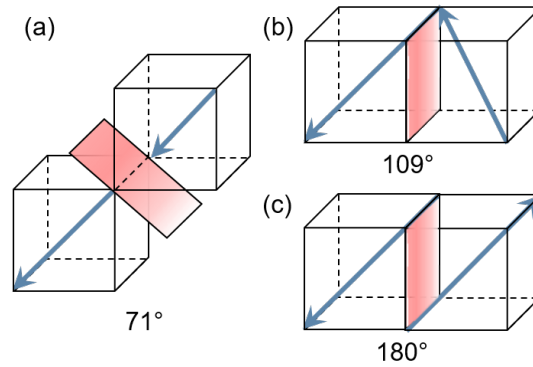
Figure 2.10: Schematics of three different domain walls that appear in BFO thin films.
(a) 71°, (b) 109°, and (c) 180° domain walls.

Recently, it was demonstrated that the spin-cycloid is sensitive to epitaxial strain[74] in thin films and can even be suppressed completely, giving rise to an appreciable canted-ferromagnetic moment[75]. Achieving a large magnetization in BFO films could potentially enable the electrical control of BFO net magnetic moment within a single layer, without a requirement to interface it with another ferromagnetic layer[70].

BFO has a rhombohedrally-distorted perovskite structure and in epitaxial thin films, its unit cells are often approximated as pseudocubic (pc). Ferroelectricity in BFO arises from Bi lone pairs that are active stereochemically and cause polar displacements of Bi and O ions along $[111]_{pc}$[68], while Fe magnetic moments are responsible for the antiferromagnetic order. BFO polarization can point along any of the eight degenerate $\langle 111 \rangle_{pc}$-related directions[76], giving rise to eight possible domain states. This, in turn, suggests the existence of three different domain walls, namely 71°, 109° and 180° domain walls, which are defined by the angle formed between polarization vectors on both sides of the wall, see Figure 2.10.

2.4.4 La$_{1-x}$Sr$_x$MnO$_3$ (LSMO)

LSMO is a manganese oxide with a perovskite structure, known for its colossal magnetoresistance[77], i.e. drastic changes in resistance upon magnetic-field application. The compound shows a rich phase diagram with a variety of ground states. La is trivalent, while Sr is divalent, which results in mixed Mn valency for $0 < x < 1$. Different magnetic orders and conduction properties can be accessed by varying temperature and Sr substitution, see Figure 2.11. Undoped LaMnO$_3$ is an insulating antiferromagnet as the Jahn-Teller distortion prevents electron hopping and the superexchange interaction enforces an antiparallel ordering of Mn^{3+} magnetic moments with a slight

canting of magnetic moments (marked as CI in Fig. 2.11). Sr substitution reduces the Jahn-Teller distortion and introduces holes to the system. The ferromagnetic order with increasing Sr content arises due to the double-exchange interaction between neighboring Mn^{3+} and Mn^{4+} ions. The hopping of electrons between manganese ions of different valency induces simultaneous ferromagnetism and electronic conduction (marked as FM in Fig. 2.11). The highest T_C is achieved with x=0.3 Sr substitution, which is a standard composition used for the LSMO thin-film deposition. When the majority of La is substituted by Sr, manganese ions once again exhibit mostly uniform valency and the antiferromagnetic order is mediated by the superexchange (marked as AFM in Fig. 2.11).
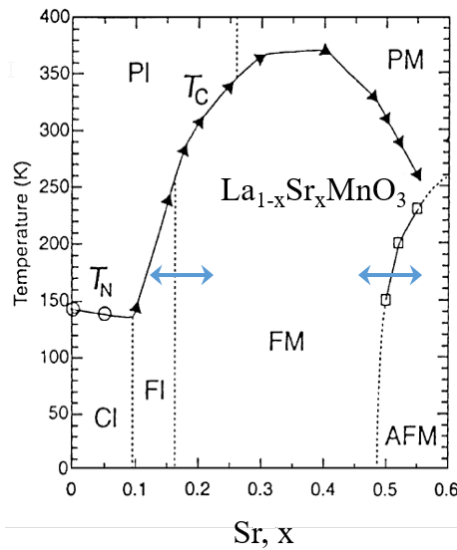
Figure 2.11: LSMO phase diagram with respect to Sr doping concentration (*x*). Abbreviations that denote phases: PM - paramagnetic metal, PI - paramagnetic insulator, FM - ferromagnetic metal, FI - ferromagnetic insulator, AFM - antiferromagnetic metal, CI - spin-canted insulator states. Blue arrows mark doping level ranges, in which phase transitions can be accessed with interfacial charge doping induced by adjacent ferrolectric layers (see section 2.5.2). Reprinted with permission from[78]. Copyright (2001) Elsevier Science B.V.

2.5   Epitaxial heterostructures of ferroic oxides

Recent developments in the modern thin-film deposition techniques allow the preparation of oxide heterostructures with atomic precision and full control over the strain state, chemical stoichiometry, crystallographic symmetry, valence of elements, domain configuration, and thickness with unit-cell accuracy. During this thesis, we will investigate properties of ultrathin oxide thin films. Henceforth, with the use of *"ultrathin films"* we refer to layers that are under 10 nm in thickness. We will explore the aston-

ishing effects taking place at their interfaces, arising due to broken inversion symmetry and enhanced electronic correlation effects induced by confinement [7,79]. It is also important to note that although these effects arise at the interface, they are not limited to it and often extend over a couple of unit cells on both sides of the interface (e.g. over the screening length in metals). This leads to interface properties dominating in the ultrathin regime, which enables exploiting them for device applications.

2.5.1 Epitaxial strain

For this thesis, ferroic thin films were grown epitaxially. During epitaxial growth, the film grows on oriented single-crystal substrates to maximize the control of the film crystallinity and orientation. The substrate is a template for the film if their lattice parameters match (or are integers/diagonals of one another) or only differ by a few percent. Coherent epitaxial strain not only ensures that the films are uniformly oriented and phase-pure but also allows to control their ferroic order [80].

The films are considered to be compressively strained, when they have larger unit cell parameters in the bulk form than those of the substrate (for simplicity let us consider both unit cells as cubic), see Figure 2.12a. In this strain state, the out-of-plane lattice parameter of the film becomes elongated, leading to an increase in the unit-cell tetragonality. As polarization is strongly coupled to the lattice, this triggers the out-of-plane polarization in the films to emerge with a higher T_C compared to the bulk value [67,80,81]. In most of the cases this implies that the films are already polar at their epitaxial deposition temperature, which enables polarization monitoring with non-linear optics during the growth process itself (see section 3.1.3). Tensile epitaxial strain is achieved in films that have smaller lattice parameters than the crystalline substrate. This, in turn, leads to in-plane-polarized films with biaxial in-plane polarization, see Figure 2.12b. In extreme cases, a considerable tensile strain was even shown to induce polarization in otherwise non-polar materials [82–84]. When the cubic approximation no longer applies to the substrate with dissimilar in-plane lattice parameters, e.g. orthorhombic substrates, a special case of anisotropic epitaxial strain is observed. It can induce uniaxial in-plane polarization as well as the formation of ferroelectric stripe domains [85]. Note that the epitaxial strain exerted by the substrate results in the same polar anisotropy in all perovskite constituents of a multilayer, i.e. compressive strain leads to all ferroelectric layers being out-of-plane-polarized, while tensile strain imposes the in-plane polarization in polar constituents of the multilayer.

The magnetization of a ferromagnetic thin film usually lies in-plane as a consequence of the magnetic shape anisotropy, but can also be tuned with epitaxial strain. It has been shown that the stress-induced anisotropy achieved with a high tensile strain can overcome the shape anisotropy and lead to technologically-relevant perpendicular
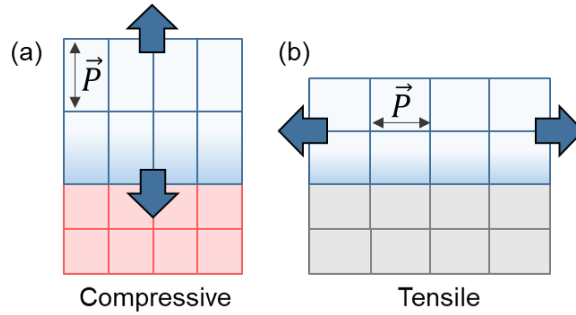
Figure 2.12: Epitaxial strain types.

magnetic anisotropy (out-of-plane magnetization) in garnet thin films[86,87]. LSMO films were also reported to be very sensitive to epitaxial strain due to strong orbital interactions in the system. Compressive strain leads to out-of-plane-magnetized LSMO films, while tensile strain enhances their in-plane magnetization. Anisotropic strain can even stabilize a uniaxial in-plane LSMO magnetization[88]. In the multiferroic BFO films, epitaxial strain not only controls the ferroelectric domain pattern[89,90] but also influences the configuration of the spin cycloid[91] and can even completely suppress it[74,92].

2.5.2 Combining ferroic orders in heterostructures

The epitaxy of complex oxides enables phenomena that are absent in bulk crystals. With regard to ferroic oxides, interfaces between ferroelectrics and ferromagnets are of high interest as they can enable coupling between polarization and magnetization. Materials that combine coupled ferroelectricity and ferromagnetism in the same phase, so-called magnetoelectric multiferroics, are very scarce due to the exclusive conditions for transition-metal d-electrons: they are required for ferromagnetism, but reduce the tendency for displacive ferroelectric distortions in perovskite oxides[93]. This scarcity can be overcome by artificial multiferroics – heterostructures made up of ferroelectric and ferromagnetic layers. The epitaxial interface between the two orders acts as a medium linking polarization to magnetization and thus enables magnetoelectric coupling between the two layers artificially.

There are three distinct ways to achieve artificial magnetoelectric coupling[8]: via (i) strain, (ii) magnetic exchange, and (iii) charge coupling. In strain-coupled artificial multiferroics, a piezoelectric layer and a magnetostrictive layer are epitaxially grown together leading to a controllable magnetoelastic anisotropy explained by the propagation of electrostrain, see Figure 2.13a. In artificial multiferroics coupled via the magnetic exchange, the interaction is considered between a ferromagnet and an intrinsic multiferroic with an antiferromagnetic order, such as BFO. The magnetic exchange coupling at the interface enables the correlation between the antiferromagnetic and

ferromagnetic spin orders, see Figure 2.13b.
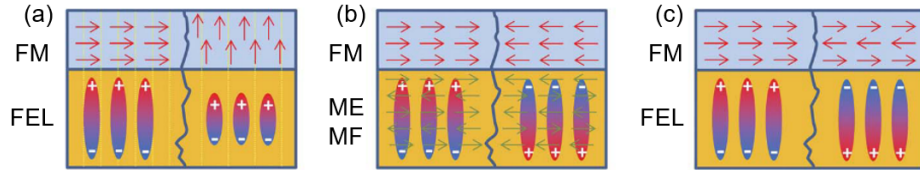
Figure 2.13: Interfacial magnetoelectric coupling in artificial multiferroic heterostructures. (a) Strain-coupling between a ferromagnet (FM) and a ferroelectric (FEL). (b) Magnetic exchange between a ferromagnet and a magnetoelectric multiferroic (ME MF). (c) Charge coupling between a ferromagnet and a ferroelectric. Reprinted with permission from [8]. Copyright (2013) RSC Publishing.

Charge-coupled artificial multiferroics make use of the ferroelectric field effect: bound charge at the ferroelectric interface is screened by the ferromagnetic metallic layer, leading to either hole-doped or electron-doped interfacial states in the ferromagnet when the polarization is pointing away from or towards the ferromagnet, respectively. If the ferromagnet is sensitive to charge doping, such as LSMO (see section 2.4.4), this might result in drastic magnetization alterations due to the local charge doping at the interface. If the chosen stoichiometry is characterized by phase transitions, as marked with blue arrows in Figure 2.11, the film interface can be switched between different magnetic phases by simply inverting the polarization direction of the neighboring ferroelectric layer [94–96], see Figure 2.13c. Microscopically this is explained by the change in the relative weights of the superexchange and double exchange energy terms as a function of electrostatic doping in the interfacial region [97].

CHAPTER 3

Methods

Parts of this chapter are published as:

- M. F. Sarott*, E. Gradauskaite*, J. Nordlander, N. Strkalj and M. Trassin. In situ monitoring of epitaxial ferroelectric thin-film growth. *Journal of Physics Condensed Matter* **33**, 293001 (2021).[98] * – equal author contributions.

All the oxide thin-film samples investigated in this thesis were prepared using pulsed laser deposition (PLD). The sample growth was monitored using reflection high-energy electron diffraction (RHEED) and in-situ optical second harmonic generation (ISHG). Structural and ferroic properties of the films were further analyzed with X-ray diffraction, scanning probe microscopy, electrical polarization measurements, and superconducting quantum interference device (SQUID)-based magnetometry after the deposition was completed.

3.1 In-situ monitoring of oxide thin-film growth

While the thin-film growth is often only seen as a simple synthesis step, in this thesis, a lot of emphasis will be placed on monitoring the growth process itself. In-situ monitoring with RHEED and ISHG provides users with invaluable knowledge on how both structure and the ferroelectric functionality evolve during synthesis. RHEED is predominantly used to establish the desired growth mode and monitor the thin-film thickness with (sub-)unit-cell precision. ISHG is used to track the onset of inversion symmetry breaking during the ferroelectric thin-film deposition, which can be related to the emergence of polarization.

3.1.1   Pulsed Laser Deposition (PLD)

The PLD growth of oxide thin films is performed in a high-vacuum growth chamber with a base pressure of 10^{-6} to 10^{-9} mbar in a custom-designed deposition system by TSST. A high-energy, pulsed (1–8 Hz) nanosecond excimer laser beam (KrF, $\lambda = 248$ nm) is focused on a spinning target inside the growth chamber, see Figure 3.1. The target is a dense ceramic that usually possesses the stoichiometry of the desired thin film. When the laser pulse hits the target, an ablation process takes place: a plasma plume of particulates is created and propagates towards the substrate. The oxygen gas flow (10^{-1}–10^{-2} mbar) is supplied to the chamber as a transfer medium to control the particle flux and to prevent oxygen off-stoichiometry. The substrate is kept at elevated temperatures (500–750°C) during the growth to increase the mobility of the ablated species, allowing them to cover the substrate evenly and reach their lowest free-energy, nearly defect-free state. The fluence of the laser pulses, their repetition rate, the substrate temperature, and the oxygen pressure are all vital factors for achieving high-quality oxide thin films.
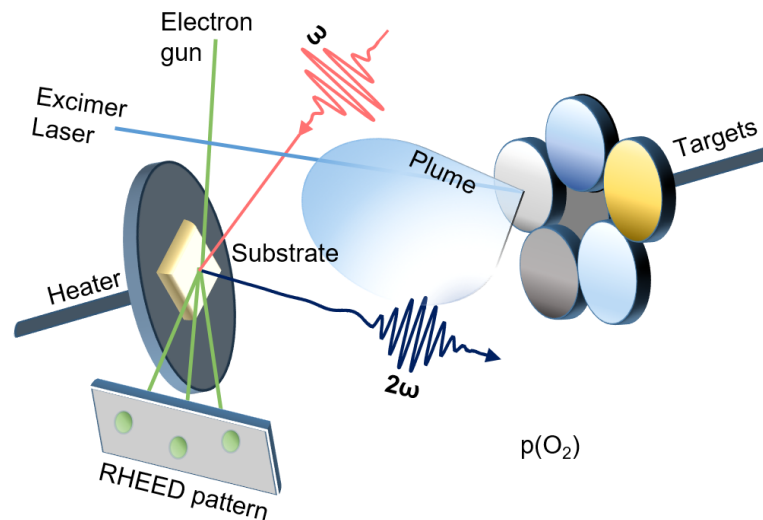
Figure 3.1: Schematic of the PLD setup. In-situ monitoring with RHEED and ISHG is performed simultaneously during the deposition of oxide thin films.

3.1.2   Reflection High-Energy Electron Diffraction (RHEED)

The high-vacuum chamber used for the PLD growth is equipped with RHEED monitoring capabilities, as shown in Figure 3.1. We use a high-pressure RHEED with differential pumping to make it compatible with the high oxygen pressure required for oxide growth. RHEED is primarily used to control the thickness of oxide films, but it also reveals the growth mode and the strain state. A high-energy electron beam is

incident on the substrate and the diffracted electrons hit a fluorescent screen, allowing diffraction patterns to be monitored. The incidence angle of the beam is as low as 0.1–2.0 degrees, which makes the technique surface sensitive (only a few atomic layers are probed at a time). The electron diffraction patterns are images of the reciprocal lattice of the surface structure in accordance with the Bragg law.
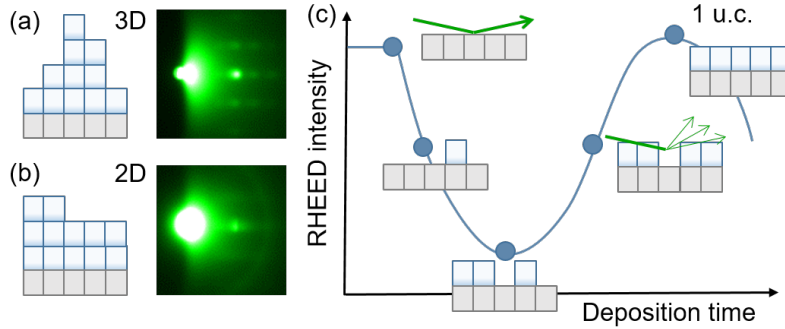
Figure 3.2: In-situ RHEED monitoring. RHEED diffraction patterns characteristic of 3D growth (a) and 2D growth (b). (c) RHEED monitoring of a 2D layer-by-layer growth results in integrated intensity oscillations. Their period corresponds to full one-layer coverage.

During a non-optimized deposition, numerous diffraction spots, characteristic of a three-dimensional scattering, are observed, see Figure 3.2a. This suggests an unwanted 3D film growth, during which three-dimensional islands nucleate on the substrate. By tuning the substrate temperature and the incoming flux of the particles, one can reach the desired 2D growth. When the planes of atoms are no longer disordered, a discrete set of the allowed 2D reciprocal lattice wavevectors gives rise to a collection of rods on the RHEED screen perpendicular to the film surface, as shown in Figure 3.2b.

The roughness of the film surface is monitored too: diffracted electrons are coherent when reflected from a flat surface and form bright features on the RHEED screen, while roughness results in a loss of intensity. If the growth mode is 2D layer-by-layer, the integrated intensity of a diffraction spot will oscillate with a period of one layer and the peak values will be reached with the completion of each layer, see Figure 3.2c.

3.1.3 In-situ Second Harmonic Generation (ISHG)

Epitaxial strain enhances the ferroelectric T_C of the films above their deposition temperature (see section 2.5.1), which makes it possible to access ferroelectric polarization during the thin-film growth using ISHG. It is a non-linear optical technique, which requires high-intensity light fields to access higher orders of electric susceptibility. During the SHG process, in a material with broken inversion symmetry, two photons are absorbed and re-emitted as a single photon with doubled frequency (Fig. 3.3a), expressed as:

$$P_i(2\omega) = \varepsilon_0 \chi_{ijk}^{(2)} E_j(\omega) E_k(\omega) \qquad (3.1)$$

where $E_j(\omega)$ and $E_k(\omega)$ are electric field components of the incident light and $P_i(2\omega)$ is the induced polarization of doubled frequency, which acts as a source for the SHG wave emitted from the sample. $\chi_{ijk}^{(2)}$ is the second-order non-linear susceptibility term that relates the geometry of the incident light to that of the SHG signal. The symmetry of the material determines which of the tensor components are allowed. The intensity of the SHG wave can be directly related to the induced polarization in the material as:

$$I(2\omega) \propto |P_i(2\omega)|^2 \qquad (3.2)$$

ISHG is sensitive to inversion-symmetry breaking and therefore is an ideal probe for polarization, as all ferroelectric crystals are non-centrosymmetric. ISHG is usually performed with a Ti:Sapphire femtosecond laser, as ultrashort pulses with high-peak intensities allow limited beam exposure to the sample and hence prevent any damage to it. Figure 3.2b shows a simplified schematic of the optical setup used for our measurements. Here, an optical parametric amplifier (OPA) is employed to tune the wavelength from the initial 800 nm beam to 1200 nm used as the fundamental frequency ω to perform the ISHG characterization of BTO and BFO. The incident light polarization is set at the angle α with a polarizer, comprising a Glan-Taylor prism and a half-wave plate. A long-pass filter is used before the sample to filter out any frequency-doubled light in the beam path. A laser beam of typically 10–30 µJ is focused on a sample area with a diameter of 250 µm, hence probing any macroscopic symmetry breaking in the sample. A high-pass filter is inserted after the sample to filter out any remaining light of the fundamental frequency and transmit only the sample SHG. The polarization of the resulting SHG light is analyzed at the angle β with another Glan-Taylor prism referred to as the analyzer. A monochromator selects the SHG light with 2ω frequency, which is collected in a photomultiplier tube (PMT).
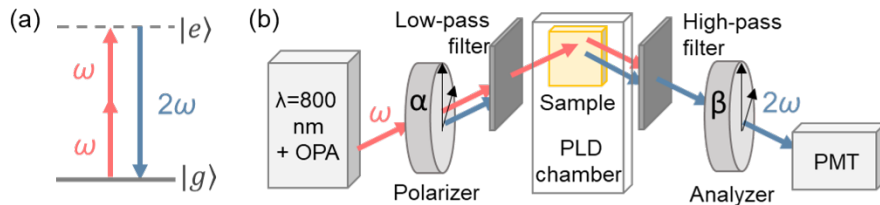

Figure 3.3: SHG measurement. (a) SHG process is defined by the conversion of two photons with ω frequency into one with 2ω frequency. (b) Schematic of the ISHG setup. α is the polarized angle and β is the analyzer detection angle, both defined clockwise in the plane perpendicular to the beam path.

Due to the limitations imposed by the growth-chamber geometry, the measurements can only be performed in reflection. This makes the ISHG experiments sensitive to the out-of-plane polarization component in the films when we track the 90°/90° component (i.e. α=90°, β=90°) in our ISHG measurements[30,99]. All thin layers in the heterostructure can be probed simultaneously as long as they transmit both the fundamental and frequency-doubled light. The SHG signal emitted from the different ferroelectric layers interferes either constructively or destructively, depending on whether their polarization directions are parallel or anti-parallel[100]. This is because a reversal of the polarization corresponds to a 180° shift in the phase of the SHG light wave[100]. This gives us information not only on whether the constituent layers are polar or not, but also on what their relative polarization directions are[30].

Additionally, one can identify the particular crystal symmetry of the film by determining its $\chi_{ijk}^{(2)}$ tensor. This can be achieved with so-called polarimetry measurements during which the SHG light associated with different $\chi^{(2)}$ components is disentangled by varying the polarizer angle α and the analyzer angle β independently. The allowed components of the $\chi_{ijk}^{(2)}$ tensor are then related to the point-group symmetry of the material.

When RHEED and ISHG monitoring are performed simultaneously, changes in spontaneous polarization can be directly related to the thickness of the ferroelectric film. Most importantly, it is a non-invasive technique, which gives access to the phenomena occurring in ultrathin ferroelectric films during their integration into complex heterostructures.

3.2 Ex-situ characterization of oxide thin films

While in-situ monitoring allows us to know the crystallinity, thickness of the films, and whether they are ferroelectric or not already at the growth temperature, a variety of additional measurements may be performed post-deposition. The full crystalline structure of the films can be determined using X-ray diffraction (XRD). Scanning probe microscopy (SPM) is used for evaluating the film topography and ferroic domain states on the microscale. Positive-up-negative-down (PUND) and SQUID-based measurements are employed to characterize macroscopic ferroelectric and ferromagnetic properties, respectively.

In some cases, our in-situ and ex-situ measurements were complemented by further experiments enabled through the support of other group members or external collaborations. Cryogenic magnetic force microscopy measurements were performed by Lukas Kürten at ETH Zurich. Scanning transmission electron microscopy (STEM) was carried out by Marta D. Rossell and Marco Campanini at Empa, Terahertz time-

domain spectroscopy by Chia-Jung Yang and Shovon Pal at ETH Zurich, while AFM tomography by Thomas Moran and Bryan Huey at the University of Connecticut.

3.2.1 X-ray diffraction (XRD)

A four-cycle diffractometer (Panalytical X'Pert Pro-MRD) is used to investigate the macroscopic crystalline structure of the thin films in more detail. As the wavelength of X-rays is comparable to the interplanar spacing in the crystalline thin films, they cause the incident X-ray radiation to diffract. The Bragg law defines the condition for constructive interference of diffracted X-rays:

$$n\lambda = 2d_{hkl}\sin\theta \qquad \text{for} \quad n = 1, 2, 3, ... \qquad (3.3)$$

where λ is the monochromatic X-ray wavelength, d_{hkl} is the interplanar spacing for a set of planes with the specific Miller indices hkl and θ is the angle of X-ray diffraction. Constructive interference results in accumulations of high-intensity that appear in the diffraction pattern obtained by varying θ and are referred to as Bragg peaks.
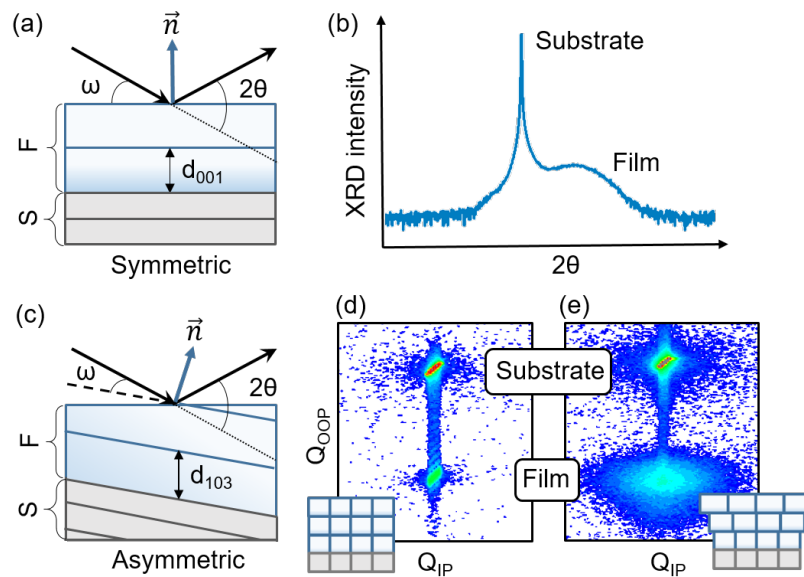
Figure 3.4: Thin-film XRD. (a) Symmetric scan geometry. (b) $\theta - 2\theta$ diffraction pattern of oriented epitaxial film. (c) Asymmetric scan geometry. RSM of coherently strained (d) and partially relaxed (e) films. S and F stand for substrate and film, respectively.

Thin-film XRD experiments are performed in two different configurations: symmetric and asymmetric. In the symmetric measurements, the light impinges onto the film with an angle ω and gets diffracted at the angle $2\theta = 2\omega$, see Figure 3.4a. In this measurement geometry, all the d_{00l} spacings, perpendicular to the sample surface, are

probed. As a result, in the $\theta - 2\theta$ diffraction pattern of oriented epitaxial films, one sees high-intensity sharp $(00l)$ reflections corresponding to the substrate and, next to them, the peaks of lower intensity related to the $(00l)$ reflections of the film. The separation between the two peaks is explained by the difference between the out-of-plane lattice parameters of the film and the substrate. In perovskite-based heterostructures, where the two unit cells are similar, $\theta - 2\theta$ scans are relatively simple and contain pairs of $(00l)$ peaks, as shown in Figure 3.4b, which reveal the epitaxial orientation of the film. In layered films of the Aurivillius phase, however, the diffraction patterns are more complex. Its anisotropic unit cell with a significantly larger c-parameter compared to that of the perovskite unit cells gives rise to numerous film peaks around each of the perovskite substrate reflections (e.g. Fig. 4.4). This provides additional information about the film layering and the existence of any potential stacking faults along the c-axis[57].

The asymmetric measurement geometry is required to gain access to the crystallinity in the plane of the film and involves a tilt of the sample with respect to ω, as shown in Figure 3.4c. In these measurements, 2θ is no longer dependent on ω, which allows mapping the off-symmetric $(h0l)$ or $(0kl)$ points in the reciprocal space and extracting the in-plane lattice parameters. Additionally, reciprocal space mapping (RSM) can be performed with so-called two-axis measurements, during which the asymmetric $\omega - 2\theta$ scans are collected for a range of ω values. This gives a two-dimensional map in reciprocal space vectors also referred to as scattering vectors Q that can be related back to the real space as $Q = 2\pi/d_{hkl}$. The goal is to capture the asymmetric reflections of both the substrate and the film in one 2D scan (as in Fig. 3.4d,e), which can then be used to evaluate the strain state of the film. The perfectly matching Q_{IP} (In-plane Q vector) values of the film and the substrate suggest a coherently strained epitaxial film, see Figure 3.4d. The film that shows a larger spread of Q_{IP} values compared to the substrate (Fig. 3.4e) is partially relaxed. In extreme cases, where the Q_{IP} differ completely, the film is fully relaxed. RSM also gives information about the crystallographic phases present, domain configuration, and its periodicity.

The in-plane symmetry of the unit cell can be further investigated by performing the ϕ scan, during which the off-axis reflections are tracked upon the sample rotation in-plane. It reveals the in-plane orientation of the film with respect to the substrate and is especially useful for finding the epitaxial relationship between different crystallographic phases, e.g. an orthorhombic Aurivillius film and a cubic perovskite substrate.

X-ray reflectivity (XRR) measurements are used to measure the thickness of each layer in a heterostructure. The measurement is performed in grazing incidence and X-rays get reflected from the interfaces separating materials with different densities. The interference of these reflected X-rays with respect to the grazing incidence angle creates a reflectometry pattern, which can be analyzed to extract the thickness of the

layers. XRR measurements can be used to confirm the growth mode and the layer thicknesses inferred from the RHEED oscillations.

3.2.2   Scanning probe microscopy (SPM)

SPM is a general term for microscopic, surface-sensitive techniques that utilize the movement of a tip brought to very close proximity to the film surface and then rastered line by line. During scanning force microscopy measurements, a tip attached to a cantilever experiences forces from the sample resulting in vertical deflection (DFL) and lateral (LF) movements, see Figure 3.5. The movements are tracked with a laser beam that impinges on the cantilever and gets reflected to a quadrant photodiode and recorded for each data point in a two-dimensional scan. The cantilever is connected to piezoscanners and a feedback controller, which ensures the precision of the tip motion and a constant tip-sample interaction throughout the measurement.

The arsing forces from the tip interaction with the sample surface are repulsive Pauli and attractive van-der-Waals forces described by the Lennard-Jones potential. These interactions characterize the sample topography in the basic measurement mode referred to as atomic force microscopy (AFM). The topography is constructed from the vertical displacements of the piezoelements required to maintain the constant tip-sample interaction.

In addition to sample surface morphology, the tip can sense magnetic stray fields, current flow, piezoresponse, electrostatic forces, etc. This leads to a multitude of measurement options that allow the mapping of the physical properties of the film on the nano- to microscale. Piezoresponse force microscopy (PFM) and magnetic force microscopy (MFM) are the two techniques most commonly performed on ferroic crystals as they characterize their ferroelectric and ferromagnetic order, respectively. We use an NT-MDT Ntegra Prima microscope, which allows these measurement modes and more, e.g. conducting AFM, resonance PFM, electrostatic force microscopy, etc.

3.2.2.1   Piezoresponse force microscopy (PFM)

PFM is used to image ferroelectric domains[101] and is based on the converse piezoelectric effect characteristic of all ferroelectrics. PFM measurements are performed with a conducting tip in contact mode. When voltage is applied between the tip and the grounded back electrode, the sample undergoes piezoelectric deformations when under the influence of the tip. These deformations are dependent on the domain state since they are described by the piezoelectric deformation tensor d_{ijk} related to the crystal symmetry (similarly as $\chi^{(2)}_{ijk}$ in SHG measurements). The laser signal recorded with

the photodiode captures the difference in piezoresponse between different ferroelectric domains enabling their two-dimensional mapping.

Lock-in amplifiers (LIA) are used to distinguish the piezoresponse-related forces from those arising from other sources. This is achieved by applying an AC voltage of frequency ω to the sample and analyzing only ω-modulated LF and DFL signals of the photodiode. The analyzed signals are recorded as lateral piezoresponse (LPFM) and vertical piezoresponse (VPFM) scans, see Figure 3.5. LPFM signal is related to the tip torsion sideways, which occurs when the in-plane-polarized domains are oriented perpendicular to the cantilever. VPFM is based on vertical tip motion, which is associated with tip deflection and buckling. Deflection originates at the out-of-plane-polarized domains, while buckling is associated with in-plane-polarization oriented parallel to the cantilever axis.

While the orientation of out-of-plane-polarized samples with respect to the cantilever is not important, films with in-plane polarization have to be oriented carefully as the piezoresponse originating from their in-plane-polarized domains can be recorded in both LPFM and VPFM channels depending on the sample mounting in the setup. Therefore, to find the direction of polarization in in-plane-polarized domains, the vectorial PFM is routinely employed. The technique relies on measuring the VPFM and LPFM images of the domain pattern at different sample orientations with respect to the cantilever. Samples are usually incrementally rotated by 45° or 90° and the resulting data sets enable unambiguous assignment of polarization directions in the sample.

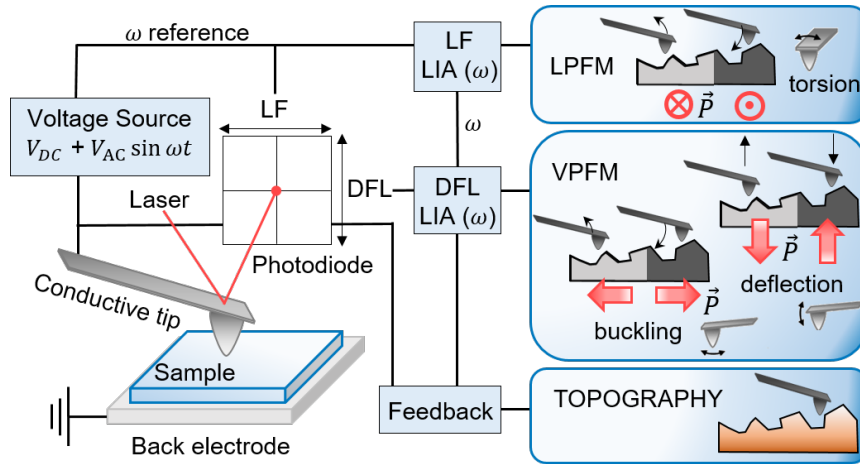**Figure 3.5: Setup for AFM and PFM measurements.** A feedback loop controls the vertical piezoelement in order to maintain constant tip-sample interaction and is used to reconstruct the sample topography. LIA-based analysis of LF and DFL laser signals at frequency ω is employed for recording LPFM and VPFM, respectively.

While primarily used to locate domains, PFM, in some instances, can also capture

the reorientation of polarization at non-Ising ferroelectric domain walls (see section 2.3). This results in additional PFM contrast exactly at the domain-wall position. The dimensions of the signal, however, cannot be related to the domain-wall width as the AFM resolution is defined by the tip radius ($\sim$30 nm), which is usually broader than the actual domain walls. It should be taken into account that the signal appearing at the domain walls can also be a measurement artifact. When scanning across c-oriented 180° domains, due to the sudden change in deflection, the tip undergoes sideways torsion exactly at the domain wall and this motion is recorded as the LPFM signal[102]. This signal no longer appears when the scanning direction is perpendicular, i.e. parallel to the domain walls, allowing to identify this signal as an artifact. The elastic response of the crystal to stress across charged domain walls can also appear as the VPFM signal[103]. At HH walls, where polar displacements meet head-on, the surface deformation is comparable to a height increase, while a reduction in height appears at TT walls, where polar displacements point away from each other.

An AFM setup can be used not only to measure but also to design ferroelectric domains. Applying DC voltage between the tip and the grounded bottom electrode allows to switch the out-of-plane polarization and write domains by scanning the selected area in contact mode. In-plane-polarized domains can be written with the so-called "trailing field"[104,105] oriented along the slow-scan axis. It arises as a consequence of the anisotropy in the electric field produced by the moving tip.

3.2.2.2   Magnetic force microscopy (MFM)

Ferromagnetic domains are imaged with MFM. It is a two-pass technique sensitive to magnetic stray fields. First, the magnetic tip is used to measure topography. After that, the tip is lifted up and, while retracing the topography, it measures the long-range magnetic response of the sample. During the second pass, the tip is oscillating at its resonance frequency and senses the stray field of out-of-plane-magnetized domains or the domain walls of in-plane-magnetized films. Repulsive magnetic forces will increase the magnitude and phase of the tip oscillations, while attractive magnetic forces will reduce both of them, allowing to distinguish and map ferromagnetic domains. Ultrathin ferromagnetic LSMO (x=0.3) films have their T_c below room temperature and necessitate MFM measurements at cryogenic temperatures, for which we use an Attocube AFM system.

3.2.3   Electrical polarization measurements

Measurements of macroscopic polarization are invasive and require metal contacts that permit the direct measurement of switching currents, which arise from bound-charge reversal during the switching events[106]. Saturation polarization can be calculated by

integrating the switched charge upon voltage application. This, however, applies to perfect insulators only. Most ferroelectrics suffer from leakage currents due to impurities[107] or defects[108], that are hard to separate from real switching currents[106]. To bypass this, the PUND technique is employed to measure switched charges associated with remanent polarization only. The experiment records current flow during five consecutive electrical pulses: the first one sets the polarization direction, the second and the third one have the opposite polarity and the last two pulses again have the initial polarity. Subtracting the currents measured during the two successive pulses with identical polarity evaluates the leakage current, which can then be subtracted from the currents measured upon voltage reversal. The integration of the resulting current is used for plotting the *P-E* hysteresis loops. A ferroelectric tester is utilized to record PUND measurements required for evaluating polarization hysteresis loops as well as fatigue and aging of the films.

3.2.4 Superconducting quantum interference device (SQUID) magnetometry

Magnetization in ferromagnets is measured without any contacts by simply applying an external magnetic field in a magnetometer. We use an MPMS3 measurement system, equipped with SQUID magnetometry, which allows macroscopic magnetization measurements in broad temperature (1 K–400 K) and magnetic field (1 Oe–7 T) ranges. SQUID is a cryogenic superconducting magnetometer, which detects magnetic flux quanta threading superconducting loops containing Josephson junctions when the sample is moved up and down. SQUID magnetometry is specifically used for thin-film samples because of its sensitivity; it can detect magnetization as low as 10^{-8} emu. Magnetization measurements can be used to determine the temperature dependence of magnetic properties and evaluate the T_c. Magnetic hysteresis loops can be recorded at any temperature to extract the coercive field or the saturation magnetization as well as to deduce the magnetic anisotropy of the film.

3.2.5 Scanning transmission electron microscopy (STEM)

In STEM experiments, a focused electron beam is scanned across a thin oriented lamella lifted out from the film of interest, here using an FEI Titan Themis microscope. The images are recorded by collecting the transmitted and scattered electrons as a function of the beam position. The resolution is limited by the electron-beam diameter, which is usually below 1 Å and thus allows the microscopy of single atoms. The diffraction angle is dependent on the scattering properties, hence, different sets of data are collected using detectors at different locations, see Figure 3.6.

The bright-field (BF) detector col-
lects the directly transmitted electrons
only. The annular dark-field (ADF) de-
tector records coherently Bragg-scattered
electrons. The electrons recorded with a
high-angle annular dark-field (HAADF)
detector, in contrast, are no longer coher-
ent and result from Rutherford scattering
from the atomic nuclei. The intensity of
these images scales with a square of the
atomic number.
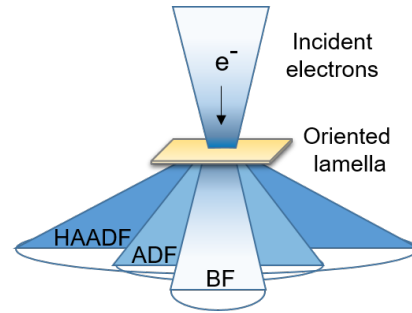
Figure 3.6: Schematic of STEM setup. Detectors at different locations are employed to collect complementary data sets.

STEM measurements can assess the quality of interfaces and evaluate the atomic displacements associated with the emergence of the ferroelectric polarization. The technique is invaluable for the structural analysis of layered ferroelectrics of the Auriv-illius phase: it can map the stacking of atomic planes and reveal any growth defects, such as out-of-phase boundaries[57,109] or intergrowths exhibiting different n of pseudo-perovskite layers[57].

3.2.6   AFM tomography

AFM tomography is an SPM-based technique used to retrieve three-dimensional prop-erty maps on the microscale. It is achieved by performing standard two-dimensional AFM scans while simultaneously milling down the film with the tip in contact mode, using relatively high loads[110]. This produces a data set with many two-dimensional slices that can be used for the reconstruction of the property of interest in all three dimensions. In this way, the technique allows obtaining spatially resolved maps of ferroelectric domains and domain walls[42], conductivity channels[111], etc.

3.2.7   Terahertz time-domain spectroscopy (THz-TDS)

THz light pulses can be generated through the optical rectification of the Ti:Sapphire 800 nm laser light. THz light interaction with semiconducting thin films has proven to be a great resource for investigating their optoelectronic properties. THz-TDS is a spectroscopic technique during which samples are probed with short pulses of THz radiation. It can be used as a non-invasive measurement of optical conductivity $\sigma(\omega)$ with respect to the THz frequency ω without the need for metal contacts or electrical wiring[112–114]. THz reflection is measured from the sample and compared to the measurement performed using a reference mirror. Changes to both the amplitude and the phase of the terahertz radiation are evaluated and the type of conductivity in the

film can be established by fitting different conductivity models (e.g. Drude free-electron model) to the collected data.

3.3 Numerical Methods

Theory-based calculations and simulations were performed to give more insight into our experimental data. Density-functional theory calculations and phase-field simulations complementing the experiments were performed by Quintin N. Meier at CEA Grenoble.

3.3.1 Density-functional theory (DFT) calculations

DFT calculations are used to find the ground-state electronic structure of a material of interest. The calculations are fully based on the quantum mechanical principles, without any empirical input, hence often referred to as "ab-initio". Instead of providing the solution to the many-body Hamiltonian of a crystal, the calculations aim to find the electron density that minimizes the total energy of the system. DFT can be used to find optimal atomic positions of a given crystal as a response to a change in electrostatic boundary conditions, epitaxial strain, as well as the inclusion of structural or stoichiometric defects. When applied to ferroelectric materials, this allows to determine the distribution of electric dipoles in the unit cell of a material.

3.3.2 Phase-field simulations

Phase-field simulations are a method to study the evolution of a system with many different phases over time and space. It is based on the simulation of the temporal evolution of a free-energy functional described by a set of classical fields such as order parameters, external fields, etc. The free-energy functional can be derived from crystal symmetry alone, but also by using the parameters calculated with DFT. In ferroic materials, phase-field simulations are invaluable for simulating the formation and evolution of domains and domain walls. The simulations can take into account interactions between different order parameters[115], emerging magnetostatic or electrostatic fields[116], or elastic deformations[117].

Robust in-plane polarization of single-crystalline Aurivillius films

Parts of this chapter are published as:

- E. Gradauskaite, M. Campanini, B. Biswas, C. W. Schneider, M. Fiebig, M. D. Rossell, M. Trassin. Robust In-Plane Ferroelectricity in Ultrathin Epitaxial Aurivillius Films. *Advanced Materials Interfaces* **7**, 2000202 (2020).[118]

- E. Gradauskaite, N. Gray, M. Campanini, M. D. Rossell, M. Trassin. Nanoscale Design of High-Quality Epitaxial Aurivillius Thin Films. *Chemistry of Materials* **33**, 9439-9446 (2021).[119]

The vast majority of research on non-volatile, low-energy-consuming ferroelectric memory up to this date has been focusing on the use of classical perovskite oxides. The emergence of polarization in their unit cells can be easily understood as an out-of-phase movement of cations and anions, which leads to an off-centering of positive charges within the oxygen octahedral cages. The simple, close-to-cubic unit cell of perovskite oxides expedites their preparation in the epitaxial thin-film form and enables integration into epitaxial heterostructures. Unfortunately, perovskite oxides suffer from ferroelectric fatigue and finite-size effects that both hinder their down-scaling for nanodevices (see sections 2.1.3 and 2.1.4). These principal drawbacks motivate the quest for alternative classes of compounds that could offer polar properties that are more robust and versatile.

The past few years have witnessed the growth of interest in non-classical ferroelectrics that retain polarization at the nanoscale, such as improper ferroelectrics[120,121], HfO_2-based ferroelectric thin films[122], two-dimensional polar materials[123], organic-inorganic hybrid ferroelectrics[124], as well as several classes of layered ferroelectrics[125]. Among the latter, those with an Aurivillius structure[39,126] stand out by virtue of their

excellent ferroelectric fatigue resilience[38] and potential for hosting multiferroicity[66]. The Aurivillius compounds of general formula $Bi_2A_{n-1}B_nO_{3n+3}$ (see section 2.4.1) were proclaimed to be fatigue-free back in the 1990s as their ceramic specimen showed no degradation in ferroelectric performance for more than 10^{12} poling cycles[38]. Their preparation in a single-crystalline thin-film form, has, however, remained challenging even thirty years later. This chapter will focus on the achievement of epitaxial, single-crystal films of the Aurivillius phase and the characterization of their polar properties. This knowledge will be indispensable in the three following chapters of this thesis, in which Aurivillius layers are shown to be the key component for advancing the ferroelectric functionality of complex oxide heterostructures.

4.1 Oxide epitaxy of single-crystalline Aurivillius phase

Despite the great potential for device applications, the highly anisotropic and layered crystal structure of Aurivillius phases renders their epitaxy all but trivial. Up until now, the crystalline Aurivillius thin-film growth has been reported via means of atomic vapor deposition[127,128] and PLD[129–132]. These films, however, were not all epitaxial, let alone single-crystalline: the epitaxy between the substrate and the film unit cells was often achieved but the presence of crystal twinning rendered them not single-crystalline. Additionally, stacking faults along the out-of-plane lattice parameter[57] were reported as another obstacle to obtaining high-quality single-crystalline Aurivillius films.

Single-crystallinity in Aurivillius thin films is highly desired in order to make use of its unusual unit cell for achieving thin films with an unconventional polar anisotropy. As a consequence of the marked anisotropy of its unit cell, the polarization in the Aurivillius phases lies along the a-axis only (for homologues of even n, see section 4.3 for a detailed explanation). Therefore, the single-crystallinity of the Aurivillius layers enables the concept of uniaxial in-plane-polarized films, with their polarization pinned along one of the substrate axis only.

	Lattice parameters (Å)			Mismatch (%)	
	a	b	c	a_{NGO}	b_{NGO}
NGO[133]	5.428	5.498	7.708		
BFTO n=4[134]	5.470	5.439	41.197	-0.21	0.51
BFTO n=6[61]	5.470	5.492	57.551	-0.77	0.10
BFTO n=8[135]	5.504	5.610	76.373	-1.40	-2.00

Table 4.1: Epitaxial relationship between BFTO family members and NdGaO₃ (NGO) substrate. BFTO n=4 films display the $a_{BFTO}\|b_{NGO}$ matching, while n=6, 8 homologues are $a_{BFTO}\|a_{NGO}$ matched.
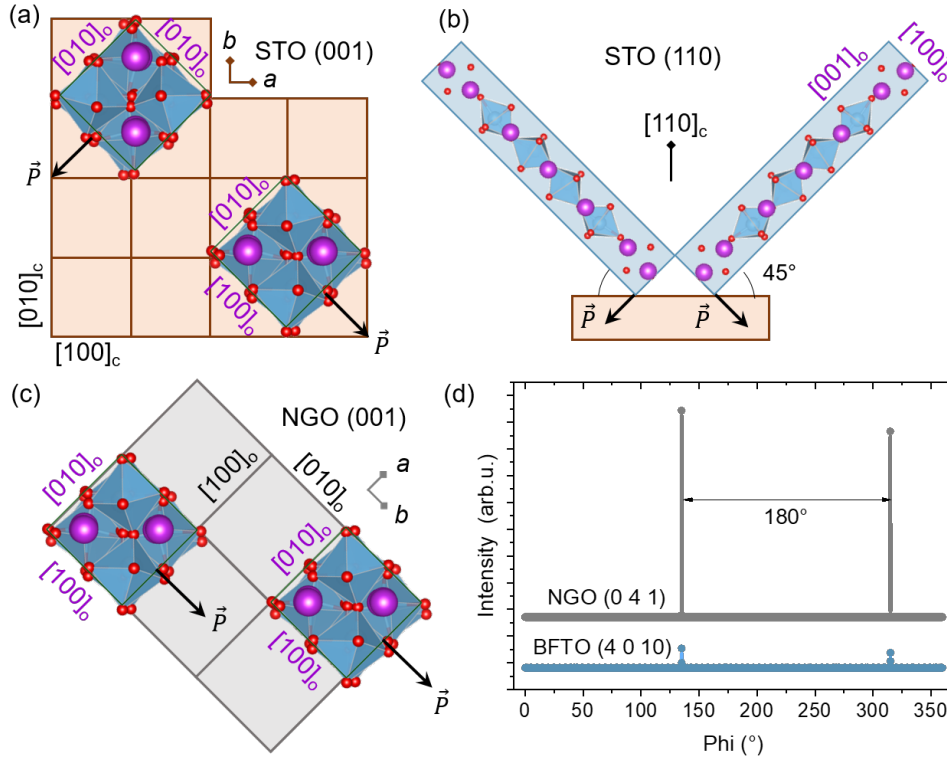
Figure 4.1: Epitaxial matching between the Aurivillius compound BFTO and cubic as well orthorhombic single-crystal substrates (a) Visualization of the epitaxial relationship between the orthorhombic BFTO unit cell and a cubic (001)-oriented substrate such as STO (001), in the plane of the film. (b) Visualization of the epitaxial relationship between the orthorhombic BFTO unit cell and a cubic (110)-oriented substrate such as STO (110), along the normal of the film plane. (c) Visualization of the epitaxial relationship between the orthorhombic BFTO unit cell and an orthorhombic NGO (001)-oriented substrate in the plane of the film. (d) XRD ϕ-scans performed on our BFTO films deposited onto NGO (001). NGO (0 4 1) and BFTO n=4 (4 0 10) peaks exhibit the two-fold symmetry of both the film and the substrate and, hence, the full epitaxial matching between the two orthorhombic unit cells.

The achievement of single-crystallinity is usually prevented by in-plane crystal twinning, which arises when the orthorhombic unit cell parameters of the Aurivillius compounds cannot be matched by common cubic single crystal substrates. By choosing $Bi_{n+1}Fe_{n-3}Ti_3O_{3n+3}$ (BFTO) as a model family of Aurivillius homologues one can see that on a standard cubic (001)-oriented substrate, such as $SrTiO_3$ (STO) (001), there are two ways of achieving epitaxy. The a and b lattice parameters of BFTO homologues only differ by around 1% in length (see Table 4.1), hence, both of them can epitaxially match the diagonal of the STO cubic unit cell, see Figure 4.1a. This, in turn, leads to the formation of two 90° Aurivillius crystal twins[130]. Up to four types of crystal twins are observed for (110)-oriented STO[58,129] as the Aurivillius unit cell adopts a 45° tilt away from the substrate plane as sketched in Figure 4.1b. In both of these cases Aurivillius films thus can be regarded as epitaxial but not single-crystalline.

In order to achieve the single-crystallinity of BFTO films, orthorhombic substrates with two different in-plane lattice parameters that closely match those of BFTO are required. We identify (001)-oriented orthorhombic $NdGaO_3$ (NGO) crystals as suitable substrates for our growth of BFTO homologues, see Table 4.1. The epitaxial strain as low as 0.2% renders the unit cell matching close to perfect, which is essential to prevent the crystal twinning, as shown in Figure 4.1c. We deposit our BFTO $n{=}4$ films onto NGO from a ceramic $Bi_5FeTi_3O_{15}$ target using PLD (see section 4.2 for more details on the growth optimization). We perform XRD analysis on one of the representative films to confirm in-plane epitaxy. ϕ-scans of XRD peaks associated with NGO and BFTO in-plane reflexes, shown in Figure 4.1d, confirm the matching two-fold in-plane symmetry of the orthorhombic film and the substrate. This rules out crystal twinning in our BFTO films grown on NGO (001).

4.2   Coalescent layer-by-layer growth mode

While the epitaxial matching prevents crystal twin formation, single crystallinity of the Aurivillius films must be additionally maintained along their c-axis. This is usually hindered by stacking faults, namely intergrowths of different n, which arise due to the large unit cell parameter and its layering along the growth direction. Fortunately, the stacking faults can be controlled and prevented with a fine-tuned set of PLD growth parameters, where both the incident atom flux and the substrate temperature are adjusted for the optimal balance between the thermodynamics of adsorption and the kinetics of crystal growth[136]. RHEED constitutes an ideal real-time tool for probing how the layering of Aurivillius film develops. Specifically, the layer-by-layer growth mode is usually desired for the growth of epitaxial thin films. It enables real-time thickness tracking, for which each peak of the integrated RHEED intensity corresponds to a complete layer of the material deposited.

In our quest for optimal BFTO growth conditions we varied the deposition temperature from 550°C to 750°C, partial oxygen pressure from $7.5{\cdot}10^{-3}$ mbar to $2.0{\cdot}10^{-1}$ mbar and the excimer laser intensity from 0.7 J cm^{-2} to 1.1 J cm^{-2}. In non-optimized BFTO growth conditions, the RHEED monitoring reveals a mixture of oscillating contributions during the film deposition as shown in Figure 4.2a. The collected signal comprises two different oscillating contributions: low-frequency oscillations labeled L superimposed with higher-frequency oscillations of lower amplitude labeled L' (Fig. 4.2a,b). In standard perovskite oxides, each periodic RHEED oscillation amounts to a layer of a cubic perovskite unit cell[98]. However, the complex RHEED pattern we obtain suggests that it does not hold true for layered unit cells of the Aurivillius phase. We use ex-situ XRR and AFM in combination with RHEED monitoring to shed light on the growth mechanism.
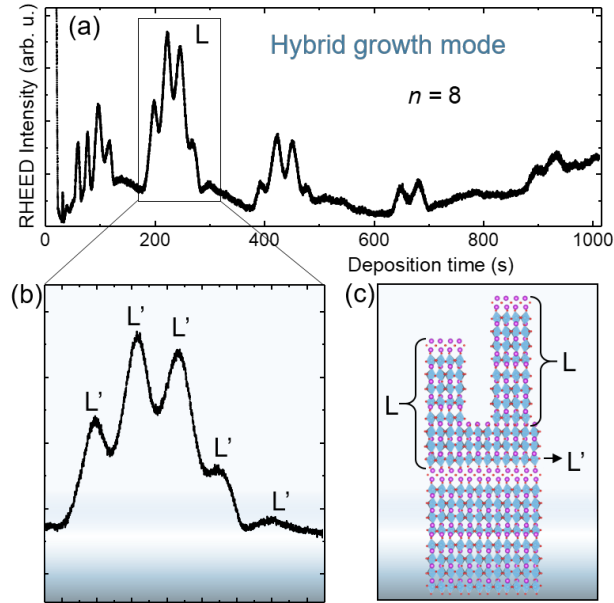
Figure 4.2: Non-optimized BFTO growth resulting in stacking faults along the *c*-axis. (a) Oscillations in RHEED intensity during the hybrid BFTO *n*=8 growth. (b) High-frequency oscillations (L') superimposed with a low-frequency high-amplitude oscillation (L) characteristic of the deposition of one half-unit-cell. (c) Flaws in the stacking sequence due to the hybrid growth mode. L and L′ denote half-unit-cell blocks and additional perovskite planes, respectively.

Ex-situ XRR measurements were performed after interrupting the growth at different stages of RHEED monitoring to find how the oscillations relate to the thickness of the film. AFM was used to measure the height of features in the topography, which we subsequently related to the growth units. We found that the high amplitude oscillations L can be linked to half-unit-cell blocks that coalesce to form full layers. However, the simple count of L oscillations is not sufficient to arrive at the measured thickness and additional layers of perovskite-type planes have to be taken into account. This suggests the presence of stacking faults resulting from the incorrect layering of perovskite and flourite-like planes in the films along the *c*-axis and allows us to deduce that the higher-period oscillations L' correspond to the secondary layering of perovskite-type planes. These observations are consistent with a hybrid growth mode, during which the film grows via the simultaneous coalescence of half-unit-cell blocks (L) and perovskite planes (L'), as sketched in Figure 4.2c. In this growth mode, unfortunately, the number of perovskite layers in the structure is not governed by the target stoichiometry and varies from one unit cell to the other. This is evidenced by the inconsistent count of low amplitude peaks L' that appear simultaneously with high amplitude oscillations L. All this suggests a lack of single crystallinity in the films along the *c*-axis due to the absence of a coherent, deterministic growth mode.

With our growth optimization, we aimed to prevent the additional layering of perovskite planes (L') in order to obtain a growth mode in which only blocks that are

half-unit-cell in height coalesce to form atomically flat layers. Layer-by-layer growth mode in a PLD setup can be achieved by optimizing the incident particle flux and the substrate temperature[136]. The particle flux is tuned by adjusting the laser fluence and the oxygen partial pressure in the high-vacuum chamber. Therefore, we systematically varied these three parameters (temperature, laser fluence, pressure) and followed the changes in the resulting RHEED patterns until we achieved the pure layer-by-layer growth of the BFTO films characterized by the coalescence of half-unit-cell blocks (L) only. Specifically, we found that an increase in the oxygen partial pressure and the higher substrate temperature were favorable for suppressing the non-stoichiometric layering of perovskite-like planes (L').
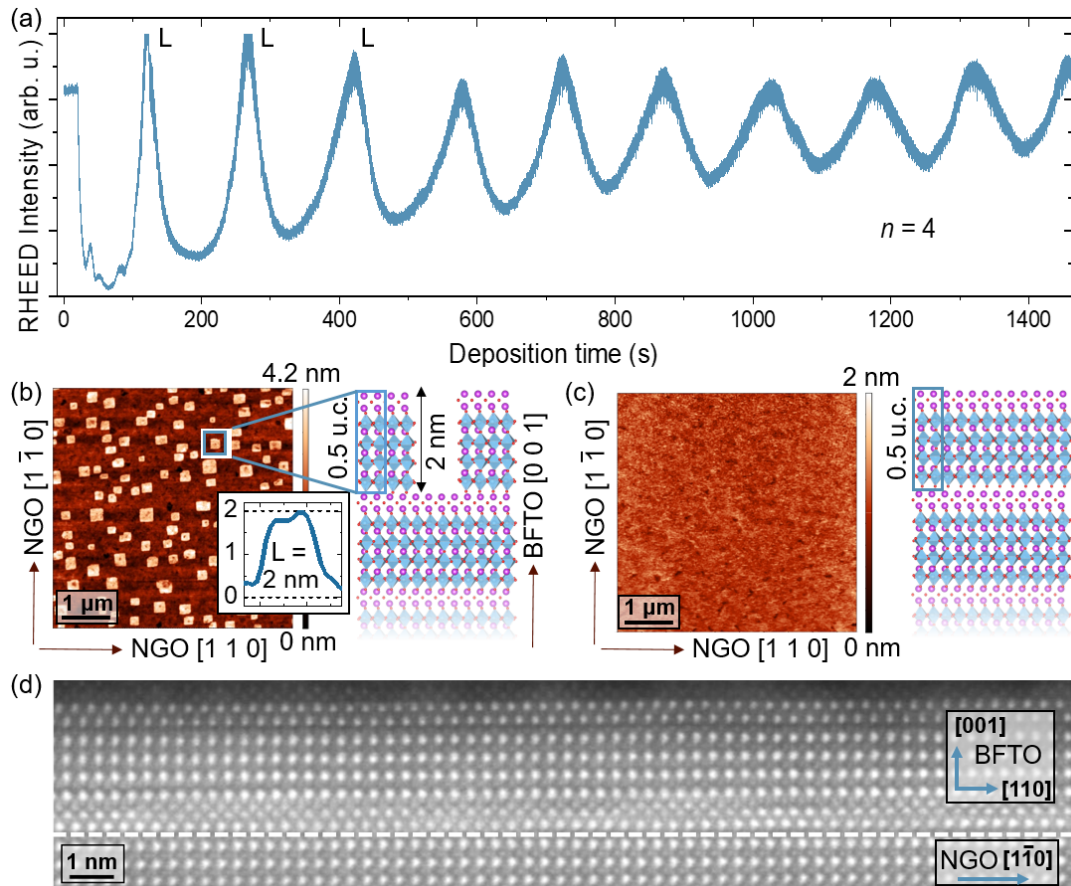
Figure 4.3: Tracking the coalescent layer-by-layer growth mode of BFTO *n*=4 thin films.
(a) Oscillations in RHEED intensity during the BFTO growth. (b) AFM topography scan of a BFTO film together with a schematic (side view) depicting the corresponding stage of the coalescent growth (i.e. an incomplete layer resulting in cuboids that are 2 nm in height). (c) AFM topography scan of the BFTO film after completion of the half unit cell together with a schematic (side view) depicting the corresponding stage of the coalescent growth (i.e. a complete layer resulting in a flat surface). (d) High-resolution HAADF-STEM image of a completed half unit cell coverage BFTO film grown on NGO.

The RHEED pattern recorded during the growth of the BFTO *n*=4 homologue

(for conditions see Table 4.2), shown in Figure 4.3a, consists of high-amplitude oscillations (L) that were recorded exclusively. To confirm the nature of the coalescent layer-by-layer growth mode, we halted the deposition away from the RHEED intensity maxima and performed AFM on the resulting film. The topography scan shown in Figure 4.3b features sharply pronounced cuboids protruding the atomically flat surface. We ruled out the possibility of a bismuth-rich parasitic phase[11,137,138] segregated to the film surface as the height of each cuboid was determined to be 2.0±0.3 nm (see inset). This is very close to one-half of the BFTO unit cell height, which is equal to 2.1 nm[134] corroborating the coalescence of growth blocks that are half-unit-cell in height. Hence, the presence of the cuboids can be explained by the incomplete layer coverage shown schematically in Figure 4.3b. Atomically flat layers, in contrast, were achieved with the deposition stopped exactly at the peak RHEED intensity, providing the full layer coverage, as shown in Figure 4.3c.
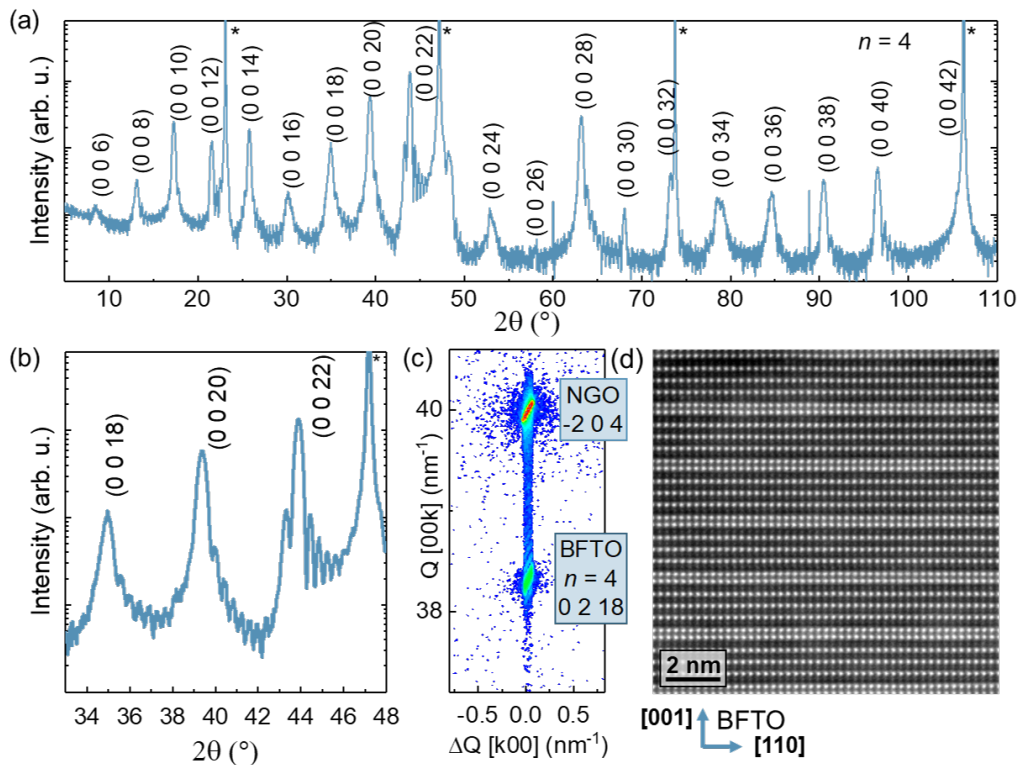
Figure 4.4: Structural analysis of BFTO *n*=4 films. (a) θ-2θ X-ray diffraction pattern indicating a (001)-oriented epitaxial orthorhombic Aurivillius thin film with no detectable impurity phases (* marks the substrate peaks). (b) Laue thickness fringes around BFTO peaks. (c) RSM of NGO (-2 0 4) and BFTO (0 2 18) peaks. (d) High-resolution HAADF-STEM image of a BFTO *n*=4 film grown on NGO (001).

The layer-by-layer growth mode we observe for BFTO is extraordinary. Unlike in perovskite films where unit cells get deposited one layer after the other, blocks of a few nanometers in height first form along the *c*-axis and only then coalesce to

form full layers. The formation of half-unit-cell islands reported for $SrBi_2Ta_2O_9$[58], a member of another Aurivillius family, suggests the generality of this growth mode for the entire compound class. It likely relates to the layered and charged structure of the Aurivillius phase: positively charged $[Bi_2O_2]^{2+}$ layers alternating with negatively charged $[A_{n-1}B_nO_{3n+1}]^{2-}$ perovskite planes. In order to preserve unit cell neutrality, the deposited species preferentially form full half-unit-cell islands before their subsequent coalescence, giving rise to the *coalescent* layer-by-layer growth mode. RHEED monitoring of such a growth process gives us a meticulous degree of control over the film thickness enabling a full film coverage as thin as 0.5 u.c. The cross-sectional HAADF-STEM image, shown in Figure 4.3d, confirms the crystalline quality of such ultrathin atomically flat layers obtained thanks to the established coalescent layer-by-layer growth mode.

In order to confirm the crystalline quality of the films, we performed their structural analysis using XRD and STEM, as detailed in Figure 4.4. A typical diffractogram of a 25-nm film (Fig. 4.4a) shows that the films are single-phase and *c*-axis-oriented. The Laue thickness fringes around the (0 0 *l*) reflexes suggest an abrupt interface to the substrate and a smooth film surface (Fig. 4.4b). The coherent epitaxial strain in the BFTO films is reflected in the RSM around NGO (-2 0 4), shown in Figure 4.4c. While XRD gives access to the global crystallinity of the film, HAADF-STEM was employed to examine the single-crystal nature of the films locally with atomic resolution. The imaging of atomic rows in the BFTO film (Fig. 4.4d) reveals the defect-free layering of four perovskite-based layers and Bi-rich flourite-like planes in line with the anticipated natural superlattice of the *n*=4 Aurivillius phase.

Figure 4.5: Stabilization of the coalescent layer-by-layer growth mode for *n*=6 and 8 BFTO homologues. Oscillations in RHEED intensity during the growth of BFTO *n*=6 (a) and *n*=8 (b). AFM topogra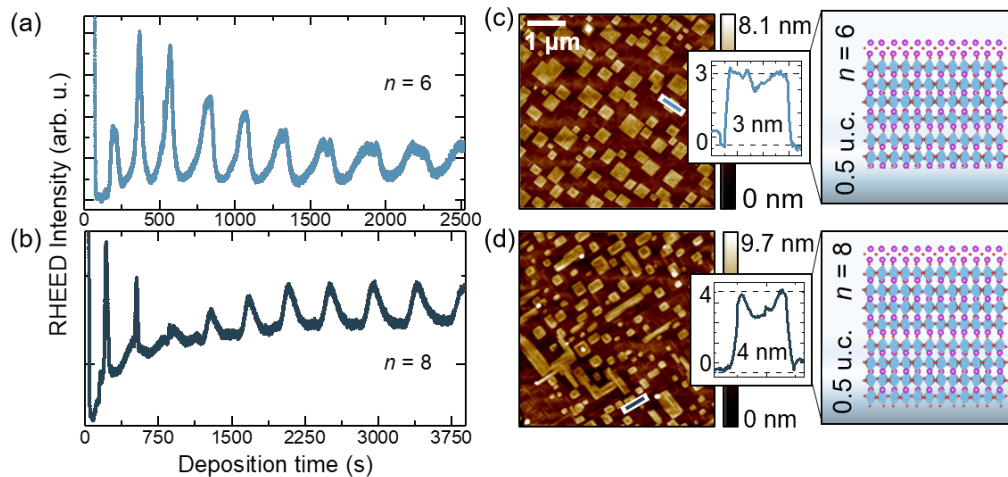phy scans of BFTO *n*=6 (c) and *n*=8 (d) films revealing the formation of cuboids with schematics that depict their structural composition.

Our approach to the achievement of single-crystal films of the Aurivillius phase can be generalized for other members of the BFTO homologous series. Additional two BFTO ceramic targets with even n, 6, and 8, are selected for film preparation, granting the uniaxial in-plane polarization along the a-axis of their unit cells. While the homologues differ substantially in their out-of-plane (c) lattice parameters, the variation in their base parameters (a and b) can be neglected, keeping NGO (001) as the substrate of choice. The coalescent layer-by-layer growth was successfully stabilized for both of the additional BFTO compositions, as shown in Figure 4.5. We note that higher oxygen partial pressure and higher laser fluence were required with the increase in n. See Table 4.2 for optimal growth conditions established for all three homologues. The periodic RHEED intensity oscillations (Fig. 4.5a,b) were once more correlated with the growth mode based on a coalescence of half-unit-cell-height blocks. The cuboids appearing in the resulting film morphologies (Fig. 4.5c,d) were measured to be 3 and 4 nm in height for the n=6 and 8 homologues, respectively. As anticipated, these values match the half c-axis lattice parameter of the two compounds, i.e. 2.9 nm[61] and 3.9 nm[135], respectively. XRD studies confirm that both films are coherently strained to the substrate and contain no detectable impurity phases, corroborating their single crystallinity. In summary, we accomplished the growth of high-quality, single-crystalline thin film of the Aurivillius phase by selecting a lattice-matching substrate with an appropriate unit-cell geometry and by stabilizing the coalescent layer-by-layer growth mode owing to a fine-tuned set of the PLD growth parameters.

Homologues	Temperature	Oxygen pressure	Laser energy
BFTO n=4	700°C	1.5·10^{-2} mbar	0.9 J cm^{-2}
BFTO n=6	700°C	5.0·10^{-2} mbar	0.9 J cm^{-2}
BFTO n=8	700°C	7.5·10^{-2} mbar	1.1 J cm^{-2}

Table 4.2: The optimized PLD parameters for a coalescent layer-by-layer growth mode of BFTO homologues.

4.3 Uniaxial in-plane-polarization in fatigue-free BFTO films

The single-crystallinity of our BFTO films implies a uniaxial in-plane polarization in epitaxial thin films, which has not been investigated before. Our established layer-by-layer growth enables the investigation of both macroscopic and microscopic polar properties in the films that are atomically flat and have a defined thickness in half-unit-cell integers. Polarization in the four-layered BFTO bulk crystals sets in at around 730°C[139], when the tetragonal paraelectric phase $I4/mmm$ transforms into the orthorhombic ferroelectric phase $A2_1am$ through polar displacements of Bi in the flourite-like layers and cooperative tilting of oxygen octahedra in between them[55,66,134]. Hence,

even though the unit cell has a non-zero net polarization along its a-lattice parameter only, the electric-dipole components along the c-axis are also present.
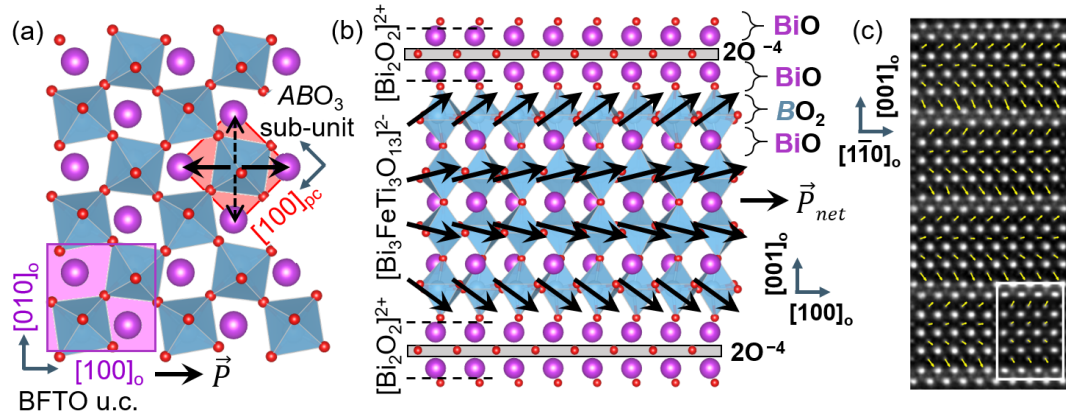
Figure 4.6: Microscopic makeup of the net polarization in BFTO $n=4$, pointing along its a-axis. (a) Top-view of one of the perovskite layers in BFTO. Pseudocubic sub-units (red) are 45° rotated in-plane with respect to the BFTO unit cell (purple). Anisotropy of the in-plane parameters leads to uniaxial in-plane polarization components only. (b) Traditionally, BFTO structure is dissected as pseudoperovskite units $[Bi_3FeTi_3O_{13}]^{2-}$ and flourite-like planes $[Bi_2O_2]^{2+}$. The two Bi layers in the flourite-like plane could alternatively be assigned to the BiO planes of perovskites leaving a single $2O^{-4}$ atomic layer in between (grey), which directs the out-of-plane polarization of the perovskite blocks. (c) Polarization maps, as obtained from the off-centering of the B-site cations, superimposed to HAADF-STEM images of BFTO films. Reprinted with permission from[109]. Copyright (2019) American Chemical Society.

To explain the origin of the uniaxial Aurivillius in-plane polarization in a qualitative, intuitive way, one could approximate Aurivillius unit cells as pseudocubic perovskite layers in between highly charged $[Bi_2O_2]^{2+}$ flourite-like planes. BFO is chosen as a representative composition for the perovskite ABO_3 sub-units as it accounts for one-quarter of all pseudoperovskite units in BFTO and the remaining $BiTiO_3$ units would not be stable as stand-alone unit cells. The pseudocubic unit cells approximating the perovskite-like sub-units are rotated by 45° with respect to the unit-cell base of BFTO. The top view of the BFTO crystal showing the in-plane relation between the BFTO unit cell and the perovskite-like sub-unit is shown in Figure 4.6a. While BFO itself has an intrinsically strong ferroelectric instability with a preferred polarization direction along the $\langle 111 \rangle_{pc}$ directions[76], the orthorhombic BFTO unit cell exerts structural anisotropic in-plane strain allowing only two in-plane polarization components oriented along its longer a-axis. The perovskite blocks are additionally subject to the electrostatics of charged planes of the layered Aurivillius phase. The negatively charged $2O^{-4}$ atomic layer in the center of flourite-like planes pulls the polarization of perovskite-like units towards it[28] as shown in Figure 4.6b. This results in perovskite layers that are polarized towards the nearest $[Bi_2O_2]^{2+}$ layer[28,109]. These out-of-plane displacements form an anti-polar pattern and cancel out in a BFTO with

$n=4$ half-unit-cell, which has a mirror plane along the c-axis. Thus, we arrive at a net polarization along the BFTO a-axis only. The described electric-dipole components in the BFTO unit cell are in agreement with polarization maps obtained from the off-centering of the B-site cations in BFTO $n=4$ acquired by STEM[109,140] (Fig. 4.6c). This basic model also illustrates why Aurivillius compounds with odd n have two polar axes. In such compounds, the central row of pseudoperovskites is under identical influence from both top and bottom $[Bi_2O_2]^{2+}$ layers. As the perovskite-like units can only adopt polarization along their diagonals, this puts the central layer in the frustrated polar state with alternating up and down polarization components[140], leading to another allowed polarization axis parallel to the c-axis[58,65].

For probing and poling out-of-plane polarized films, one uses a standard capacitor architecture (electrode|ferroelectric|electrode). Here, however, the in-plane polarization of the BFTO $n=4$ films necessitates a different measurement geometry. Two sets of gold top electrodes were deposited onto our films in an interdigitated geometry. Interdigitated electrodes allow probing the polarization switching along both the a and b axes of the film. Figure 4.7a shows the corresponding P-E loops measured for a BFTO film of 2.5 u.c. A saturation polarization of 16.5 μC cm^{-2} was measured along the a-axis in the absence of leakage currents. In contrast, no switching was recorded orthogonal to it, along the b-axis, under identical field application, confirming the uniaxial nature of the film macroscopically. We demonstrated an excellent fatigue resilience of BFTO films by recording both the positive and negative remanent polarization as a function of the number of reversal cycles (Fig. 4.7b). The ferroelectric properties of the film remain virtually unchanged for at least 10^{10} cycles suggesting that the fatigue-free behavior of Aurivillius ceramics[38] can be readily transferred to ultrathin single-crystalline films.
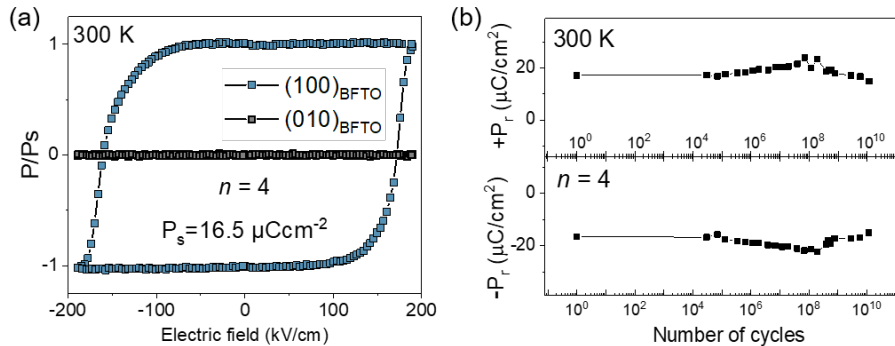
Figure 4.7: Macroscopic polarization switching properties of BFTO films of 2.5 u.c.
(a) Anisotropic switching behavior along and perpendicular to the a-axis of the BFTO films. (b) Fatigue endurance in the films measured for 10^{10} switching cycles.

4.4   Microscopic confirmation of sub-unit cell polarization

The uniaxial polarization in our Aurivillius films and their thickness control with half-unit-cell precision allow us to analyze their domain state at different thicknesses using PFM. Atomically flat surfaces eliminate the topographic cross-talk, which enables the achievement of high-resolution measurements. To begin with, we confirm the uniaxial nature of the films on the microscale. When 5-u.c.-thick BFTO films are probed with their polarization parallel to the cantilever, the domain contrast appears predominantly in the vertical channel due to upwards and downwards buckling of the cantilever[141] as shown in Figure 4.8a. Upon 90° rotation of the film when the cantilever lies perpendicular to the polar axis of the film, the domain pattern is recorded in the lateral channel through sideways buckling of the cantilever[141] (Fig. 4.8b). The vertical channel now shows a homogeneous signal only. Marked differences in the piezoresponse upon the 90° sample rotation validate the uniaxial film polarization. This experiment also allows us to conclude that BFTO films possess no net out-of-plane polarization as the associated piezoresponse would not vary upon in-plane sample rotation.
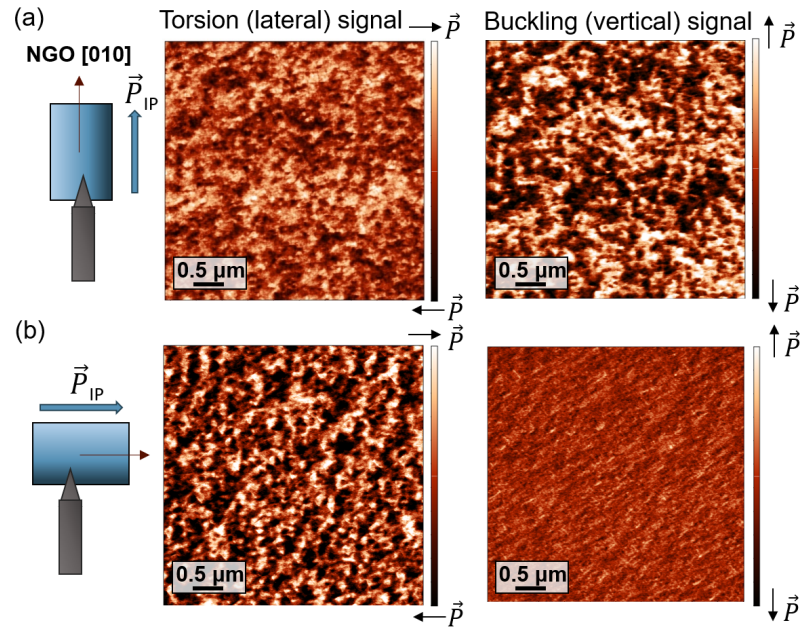
Figure 4.8: Uniaxial polar properties of the BFTO films confirmed on the microscale with vectorial PFM. VPFM and LPFM signals recorded with the cantilever parallel (a) and perpendicular (b) to the in-plane polarization axis.

Let us now have a closer look at the BFTO domain configuration. LPFM measurements performed on a 5-u.c.-thick BFTO film reveal a multidomain pattern with randomly oriented in-plane-polarized domains that have lateral dimensions smaller
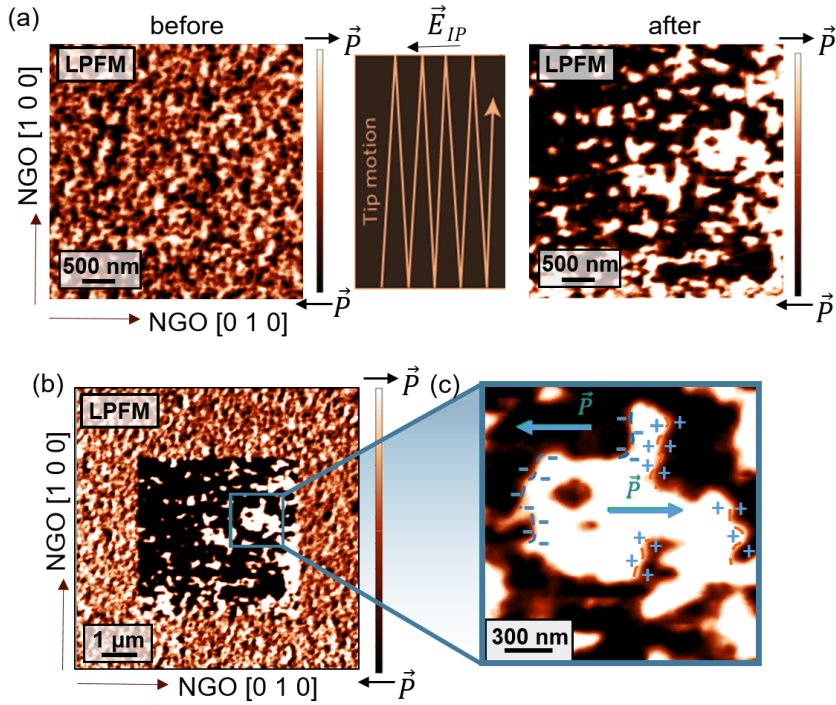
Figure 4.9: Changes in BFTO domain configuration upon the application of the in-plane trailing field. (a) LPFM measurements on a 5-u.c. BFTO film prior (left) and after (right) in-plane poling with a trailing field of the SPM tip (center). (b) Comparison of pristine and altered domain configurations. (c) Close-up of the switched area with enlarged charged domain wall sections.

than 100 nm (Fig. 4.9a). Despite the absence of a metallic bottom electrode, an in-plane trailing field can still be generated through the movement of the biased (5V) scanning-probe tip. This field is directed opposite to the slow scanning direction and, when it matches the polar axis of the film, it significantly influences the domain pattern as schematized in Figure 4.9a. Domain walls become mobile under the trailing field and lead to the formation of larger domains. Figure 4.9b shows the comparison of pristine and altered domain patterns. Even though this method does not produce uniformly switched areas but modifies the ratio of domain populations, its strength lies in the elongation of domain-wall sections that are charged (Fig. 4.9c) and as such potentially useful for domain wall nanoelectronics [50,51,142].

Our achievement of a coalescent layer-by-layer growth mode in three different BFTO homologues allows us to see how their domain configurations differ at a constant film thickness and whether the domain pattern is influenced by the number n of perovskite layers in the structure. Figure 4.10a shows LPFM scans recorded for BFTO $n=4$, 6, and 8 films of exactly 2.5 u.c. All three domain configurations are composed of randomly oriented in-plane-polarized domains of similar size, with some of the walls neutral and some of them charged, as sketched in Figure 4.10b, suggesting that the domain configuration is universal throughout the homologous BFTO series.
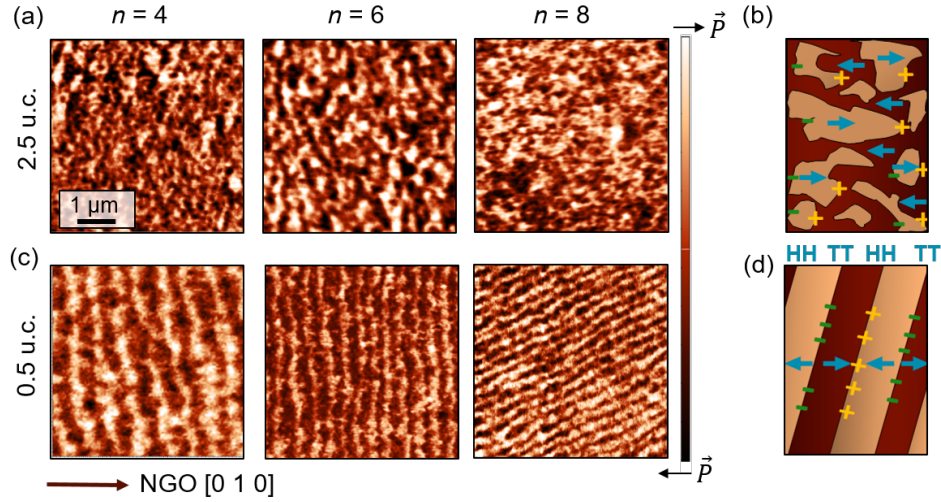
Figure 4.10: Domain configuration in BFTO *n*=4, 6, and 8 homologues. (a) LPFM measurements of 2.5-u.c.-thick films of the three BFTO homologues. The resulting small, randomly-distributed in-plane-polarized domains are represented in (b). (c) LPFM measurements of 0.5-u.c.-thick films of the three BFTO homologues. The resulting stripe domains with TT and HH domain walls are depicted in (d).

Lastly, we investigate how robust the polarization of BFTO films remains when their thickness is less than a unit cell. Out-of-plane ferroelectrics normally possess a critical thickness of a few unit cells because of the depolarizing field[30,41] (see section 2.1.4). In contrast, in-plane-polarized films are expected to be less susceptible to the depolarizing field since their polarization is now constricted not by the film thickness but rather by the lateral size of the domains, which in this case is around 100 nm. A single half-unit-cell layer is the thinnest continuous BFTO coverage achievable through the layer-by-layer growth mode and corresponds to one maximum of the RHEED intensity. It already contains four perovskite layers and their polar displacements define the in-plane polarization of the BFTO compound, see Figure 4.6. LPFM scans of these deposited ultrathin layers are shown in Figure 4.10c. A clear piezoresponse of the ferroelectric domains corroborates the absence of a critical thickness for ferroelectricity in the in-plane BFTO and suggests that one half-unit-cell coverage already exhibits the full material functionality. Additionally, in-plane stripe domains were uncovered in the films of all three homologues. Surprisingly, we found that these stripe domains are approximately orthogonal to the uniaxial polarization direction. This gives rise to periodic arrays of charged 180° walls, where HH and TT walls alternate along the $[010]_{NGO}$ direction, as schematized in Figure 4.10d. The formation of these charged domain walls is undoubtedly surprising. Due to their unfavorable electrostatic boundary conditions, charged domain walls do not ordinarily occur in proper ferroelectrics[49]. Therefore, the stripe domains in the BFTO homologues constitute an unprecedented example of spontaneous formation and periodic arrangement of charged domain walls,

which will be further scrutinized in the following chapter.

4.5 Discussion and outlook

The design of single-crystalline epitaxial Aurivillius films lays the foundation for fatigue-free and sub-unit-cell-thick ferroelectric layers exhibiting charged domain walls. The coalescent layer-by-layer growth mode, introduced with our work, enables a reproducible control of structural and polar properties of the BFTO homologous series. Such growth mode is usually associated with classical perovskite compounds[143] with only a few expectations of layered compounds, including iron garnets[144,145], hexagonal manganites[146] or gallium ferrite[147]. We now expand this list with Aurivillius layered ferroelectrics.

The established coalescent layer-by-layer growth mode of BFTO compounds opens up many experimental avenues. It enables an epitaxial combination of different n homologues from single-composition PLD targets to construct artificial phases, which was previously only possible by oxide MBE[148,149]. Such artificial heterostructures of Aurivillius phases could lead to the tunability of the spontaneous polarization and the ferroelectric Curie temperature[58,62]. In particular, mixing odd and even n homologues would create layers with in-plane and out-of-plane polarization components. This could tune the interlayer interactions and allow preserving the same domain pattern (e.g. stripe domains characteristic of ultrathin layers only) through the film thickness. Furthermore, the controlled layering of the BFTO unit cell allows tracking the evolution of polarization during the growth using ISHG. In section 4.3, we saw how the charge of flourite-like planes impacts the polarization in perovskite-like layers. Using ISHG we could probe the resulting dynamic changes in electrostatics and the net polarization of the heterostructure throughout the deposition of Aurivillius thin films.

Our approach toward single-crystallinity of the BFTO ultrathin films is likely to be generally effective with Aurivillius phases as well as with other layered compounds[125] of general interest like Ruddlesden–Popper phases[150] or Dion-Jacobson[151] compounds. Thinking beyond single-phase films, our nanoscale design of Aurivillius layers is also a prerequisite for heterostructures that epitaxially combine Aurivillius layers with classical perovskites. This could enable the conception of hybrid functional oxide multilayers, such as multiferroic memories[152,153] or in-plane ferroelectric tunnel junctions[154], and we will explore these options in Chapters 6 and 7.

CHAPTER 5

Domain engineering using structural defect ordering

Parts of this chapter are published as:

- E. Gradauskaite, K. A. Hunnestad, Q. N. Meier, D. Meier, M. Trassin. Ferroelectric domain engineering using structural defect ordering, *Chemistry of Materials* **34**, 6468–6475 (2022).[155]

- E. Gradauskaite, M. Campanini, B. Biswas, C. W. Schneider, M. Fiebig, M. D. Rossell, M. Trassin. Robust In-Plane Ferroelectricity in Ultrathin Epitaxial Aurivillius Films. *Advanced Materials Interfaces* **7**, 2000202 (2020).[118]

Ferroelectric materials possess spontaneous polarization as their order parameter, which makes them attractive for technological applications. In many cases, the uniform direction of polarization cannot be preserved long range in order to prevent the accumulation of uncompensated bound charges (see section 2.2), which leads to the formation of domains - regions with differently oriented order parameter. Domains are closely linked to the desired device functionality. Single-domain ferroelectric thin films, for instance, are required for tunnel-junction-based functionality[154,156], while a multidomain state is preferred for memristors[18,157], domain-wall memories[158,159], or nanocircuitry[50,160,161]. This suggests that the control of domain formation is of crucial importance for the integration of ferroic oxides into nanoscale devices.

The two most frequently explored methods for ferroelectric domain engineering rely on epitaxial strain[80] and interfacial electrostatics[22]. These approaches enable selectivity over macroscopic functional properties in the thin films, such as the polar anisotropy[162,163], allowed domain states and their populations[162,163], as well as domain wall types[164,165]. Unfortunately, up to this date, the ways to achieve the deterministic nucleation of domains at predefined locations with controlled dimensions

microscopically remain very scarce. In this chapter, we show that this can be achieved through the ordering of structural defects induced by atomic substrate steps. Substrate steps serve as nucleation sites for charged domain wall formation in ferroelectric BFTO films. In this way, tuning of substrate morphology allows for the precise positioning of domains and domain walls in the film. Thus, we establish a new structural approach to domain and domain-wall engineering and we show that it can be extended to other classes of ferroic oxides, likely to benefit the ever-evolving field of oxide electronics.

5.1 Periodic arrays of HH and TT walls in BFTO
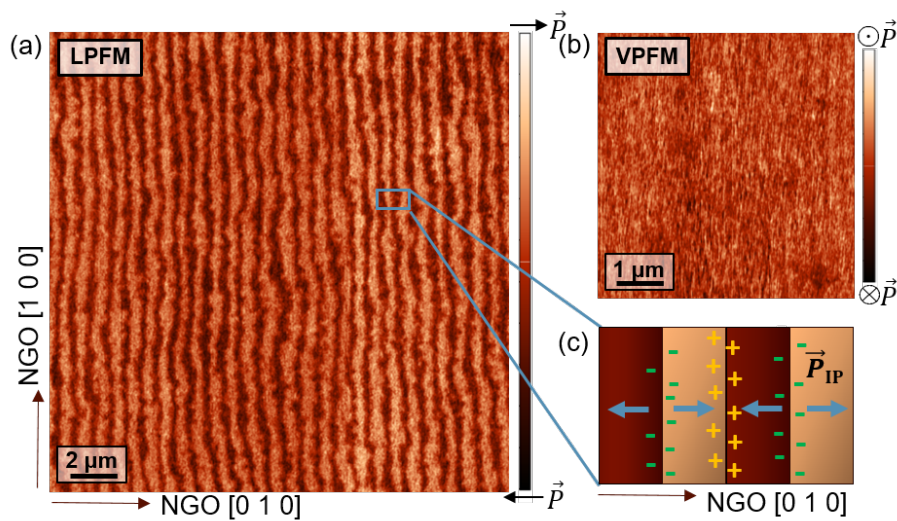
Figure 5.1: Array of periodic charged domain walls in 0.5-u.c.-thick BFTO _n_=4 thin films. (a) LPFM and (b) VPFM images recorded with the cantilever aligned perpendicular to the polar axis corroborate uniaxial in-plane ferroelectricity and fully in-plane-polarized domains. c) Sketch of charged domain walls and of the corresponding bound-charge accumulation.

In the previous chapter, we witnessed the unusual formation of charged domain walls in ultrathin BFTO layers grown on NGO (001). Here, we take a closer look at the domain configuration in 0.5-u.c.-thick BFTO n=4 films using PFM. The PFM signal corresponding to ferroelectric domains is maximized in the LPFM channel when measured with a cantilever perpendicular to the in-plane polarization, while the VPFM channel contains no domain information (Fig. 5.1a,b, performed similarly to Fig. 4.8). This allows us to confirm the uniaxial in-plane polarization along the $[010]_{NGO}$ direction (see section 4.3). Strikingly, the domain walls are running perpendicular to the uniaxial in-plane polarization of the film, This leads to a periodic array of alternating functional HH and TT domain walls, sketched in Figure 5.1c. Charged domain walls hold promise for domain-wall nanoelectronics as they exhibit conduction different from the rest of the surrounding bulk[49–51,160] (see section 2.3.2). They are, however, energetically

unfavorable in proper ferroelectrics and can only be created via the special treatment of the samples[166]. This suggests that the observed stripe-domain formation in BFTO is unique and calls for further investigations into the driving force behind it as well as ways of tuning it.

5.2 Domain engineering based on structural defect ordering in ferroelectrics

The stripe domains in BFTO are highly ordered, with a width of ca. 250 nm (Fig. 5.1a), and expand over more than 100 μm in both lateral directions. All these features are reminiscent of substrate atomic terraces that result from the substrate miscut angle[32]. While BFTO stripe domains show piezoresponse along one substrate axis only and, therefore, cannot be artifacts arising from the topography, their formation is likely related to the structural perturbations to the BFTO crystal lattice that occur at every substrate step. At each substrate step, the film deposited on top has to adopt a shift in the c lattice parameter equal to the substrate step height $\frac{c_o}{2}$ [32] as sketched in Figure 5.2a. While in perovskite heterostructures, the step height is approximately equal to the unit-cell height of the film itself and can be neglected, here the shift is equal to a fraction of the BFTO unit-cell parameter c, creating an appreciable mismatch in the atomic layering. These structural defects are called out-of-phase boundaries (OPBs) and are abundant in layered materials with anisotropic unit cells[57,167]. OPBs usually form spontaneously during synthesis and induce local strain fields in the lattice, creating non-uniform electrostatics and hence affecting the physical properties of the films[140,168–170], e.g. resulting in domain formation[140,171]. In our case, the OPBs are introduced into the Aurivillius lattice at every substrate step in a controlled fashion and are referred to as steric OPBs[57,172].

The correlation between the substrate morphology and the domain pattern suggests the possibility to define the exact location of the domain walls and even tune the size of the domains by substrate treatment. In order to demonstrate such control, we varied thermal annealing conditions and chose different miscut angles α, sketched in Figure 5.2b. Substrate annealing or chemical etching can determine the shape of the step edges (e.g. straight or wavy), while the miscut angle selection defines the spacing between step edges. We performed AFM on differently treated NGO substrates and then deposited 1-u.c.-thick BFTO films onto them. LPFM is performed after the deposition to evaluate how the substrate morphology influences the domain pattern. Figure 5.2c shows the topography of the as-received NGO (001) substrate (ca. 0.02° miscut) with its terraces of variable width arranged in a random fashion. The corresponding PFM scan performed after the BFTO deposition (Fig. 5.2d) reveals a ferroelectric domain pattern, which closely resembles the substrate terrace morphology. Figure 5.2e
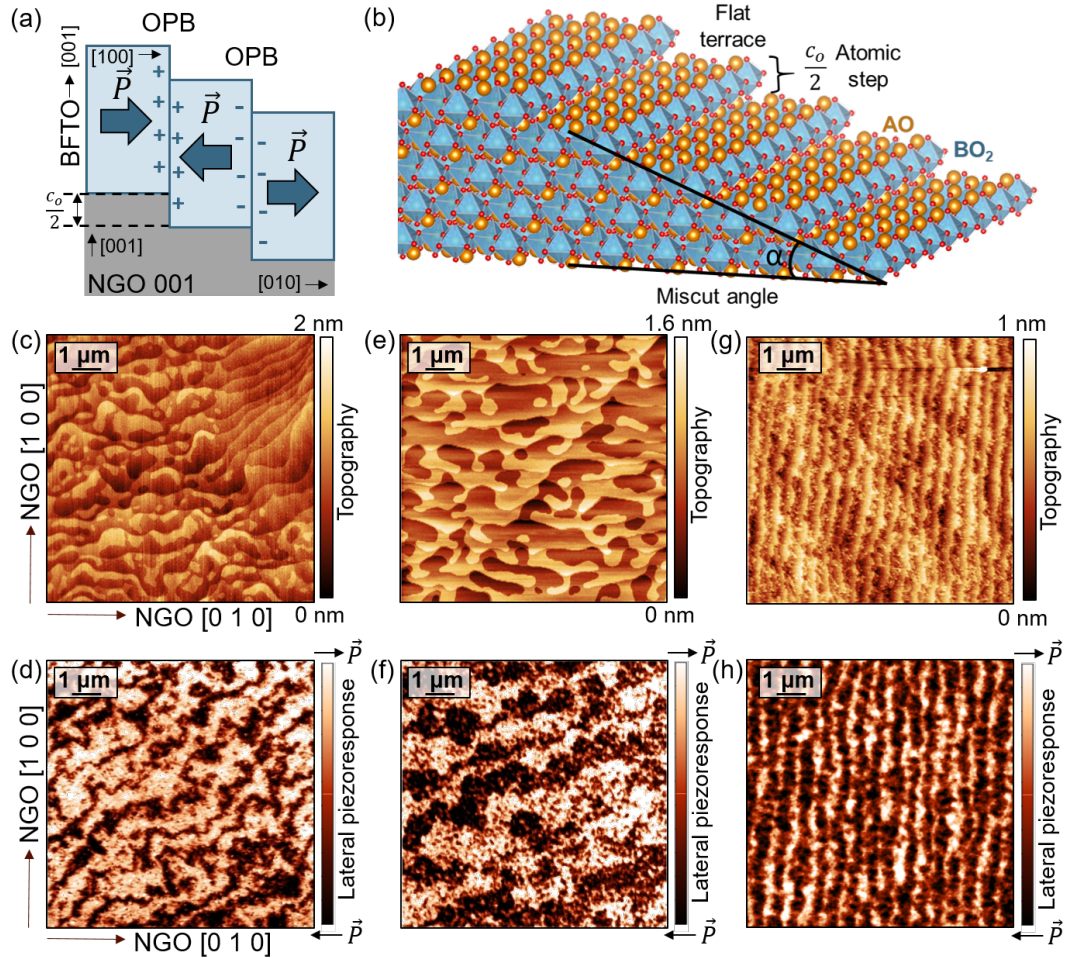
Figure 5.2: Ferroelectric domain engineering with structural defects at substrate steps.
(a) Schematic depicting steric OPBs in BFTO at every substrate step, leading to the formation of ferroelectric domain walls. (b) Schematic of atomically flat terraces and substrate steps of a perovskite-type ABO_3 crystal. (c,d) Topography of the NGO (001) substrate (c) and the corresponding domain configuration (d) in 1-u.c.-thick BFTO grown onto it. (e,f) Topography of the annealed NGO (001) substrate (e) and the resulting domains (f) in 1-u.c.-thick BFTO. (g,h) Topography of the chemically-etched NGO (001) substrate with aligned narrow terraces (g) and the resulting domains (h) in 1-u.c.-thick BFTO.

shows an image of the AFM scan of the NGO substrate topography after thermal annealing at 1200°C in an oxygen atmosphere. Thermal treatment leads to wider substrate terraces that directly translate to wider ferroelectric domains that appear in the PFM scan (Fig. 5.2f). Lastly, Figure 5.2g shows the topography of NGO substrate with a higher 0.05° miscut angle giving rise to straight, short-period step edges. The LPFM scan (Fig. 5.2h) recorded on a 1-u.c.-thick BFTO layer deposited onto it yields straight and closely packed stripe domains proving the effectiveness and tunability of the domain formation driven by steric OPBs. This provides us with compelling proof that substrate step edges can be used for the design of domain walls.

5.3 Steric out-of-phase boundaries (OPBs) as nucleation sites for charged domain walls

In order to understand the mechanism behind the observed domain-wall nucleation at every substrate step, we use DFT calculations for which we construct a unit cell made up of 384 atoms and comprising one OPB, shown in Figure 5.3a. We calculate the electric-dipole configuration in the unit cell and how it is affected by a shift in the BFTO crystal lattice, equivalent to a perovskite NGO unit-cell height along the out-of-plane c-axis. Figure 5.3b shows the calculated local B-site polar displacements in the a-c plane around the created OPB. While the out-of-plane components adjust to match the anti-polar ordering of the neighboring unit cells on the other side of the OPB, the orientation of the net in-plane polarization component remains unchanged across the OPB. This suggests that the structural changes alone are not sufficient to enforce the polarization reversal at the OPB.
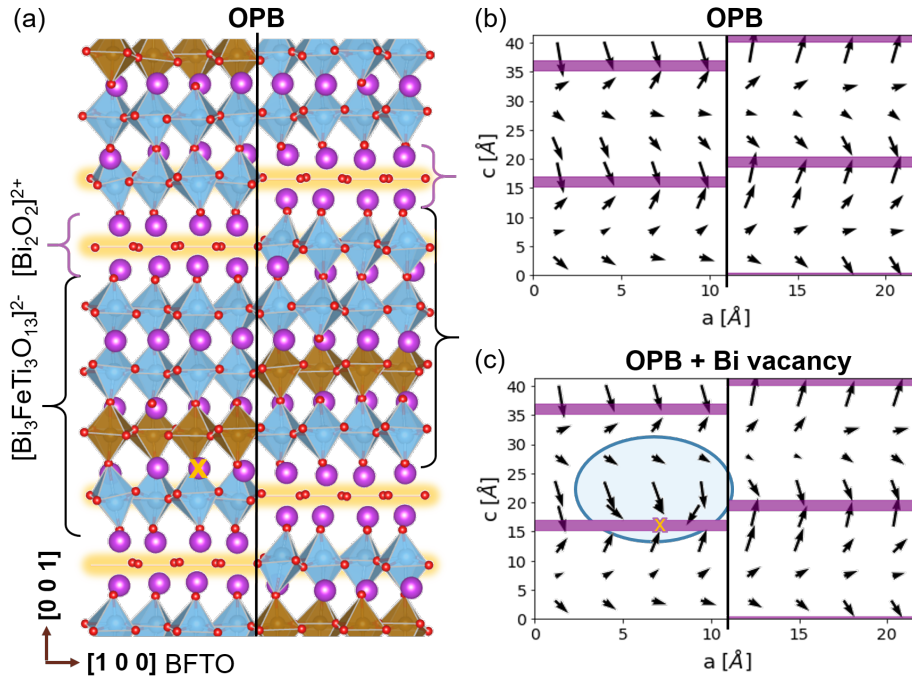
Figure 5.3: Stabilization mechanisms of BFTO charged domain walls nucleated at OPBs.
(a) Atomic structure of BFTO lattice at the OPB. The Bi atom marked with an orange cross corresponds to the defect site analyzed in (c). Brown and blue octahedra represent Fe and Ti atoms in the B-sites, respectively. The selected *inner* distribution of Fe ions is implemented as it is the lowest energy configuration[66]. Yellow shading highlights the discontinuity in the crystal structure across the OPB. (b) Local off-centering of the Fe/Ti B-site ions around the OPB. Purple bars correspond to Bi_2O_2 layers. (c) Local off-centering of the Fe/Ti B-site ions around the OPB with a single Bi vacancy marked with an orange cross. Local polarization reversal is observed.

A closer look at the atomic structure around the OPB reveals large octahedral distortions where flourite-like Bi_2O_2 layers are in the same crystal plane as the perovskite-like layers (highlighted in yellow in Figure 5.3a). The large strain gradients arise as a consequence of different Bi-Bi bond lengths in the flourite-like Bi_2O_2 and the pseudoperovskite growth blocks. One way to relieve such strain fields is by vacancy creation[173]. The notorious Bi volatility[137,174] motivates us to quantify the formation energies of Bi vacancies at the OPB sites using DFT calculations. Indeed, we find that Bi vacancies are energetically predisposed to form at the highly-strained Bi_2O_2-perovskite interface. As charged defects are known to influence the arrangement of electric dipoles[35,175], we now investigate how the pattern of local B-site displacements around the OPB changes after a single Bi atom is removed. DFT calculations of local displacements around the OPB (Fig. 5.3c) reveal that a negative charge at the vacancy site induces a local polarization reversal, creating a local HH meeting of polarization. This is in agreement with a previous report of oxygen-vacancy driven TT-wall stabilization in $BaTiO_3$[176]. A similar mechanism of non-stoichiometric defects stabilizing charged domain boundaries has recently been proposed for an improper ferroelectric of Ruddlesden-Popper phase, in which the excess of Sr atoms segregates at charged TT domain walls[171]. Mass spectra of our films reveal that they are deficient in both bismuth and oxygen compared to the nominal BFTO stoichiometry, suggesting vacancies of both Bi and O. The Bi vacancies provide negative screening charges that stabilize the HH walls, while the oxygen vacancies, in contrast, carry positive charge required to stabilize the TT walls. In Figure 5.3c we see that a single vacancy already heavily influences the arrangement of electric dipole moments, hence it is reasonable to assume that a higher vacancy concentration could reverse the polarization fully and form a domain wall. Therefore, we can conclude that the domain wall formation at each substrate step observed in our BFTO films results from the combination of structural changes and chemical off-stoichiometry at the OPB defects.

5.4 Integration of engineered domains into heterostructures

So far, we have only investigated the domain formation in a single BFTO layer. Nonetheless, in order to harness the system for domain-wall nanoelectronics or photovoltaics,[177,178] it is advantageous to have it epitaxially integrated into oxide heterostructures. Therefore, we proceed with BFTO deposition onto buffer layers to find out how much the stripe pattern is dependent on the NGO substrate. Choosing dielectric and metallic buffers additionally allows us to check whether the domain formation is affected by changes in strain and electrostatics, respectively. For reference, Figure 5.4a shows stripe domains in a 1-u.c.-thick BFTO film grown directly onto the NGO substrate. The stripe domains indicate the in-plane polarization reversal at every
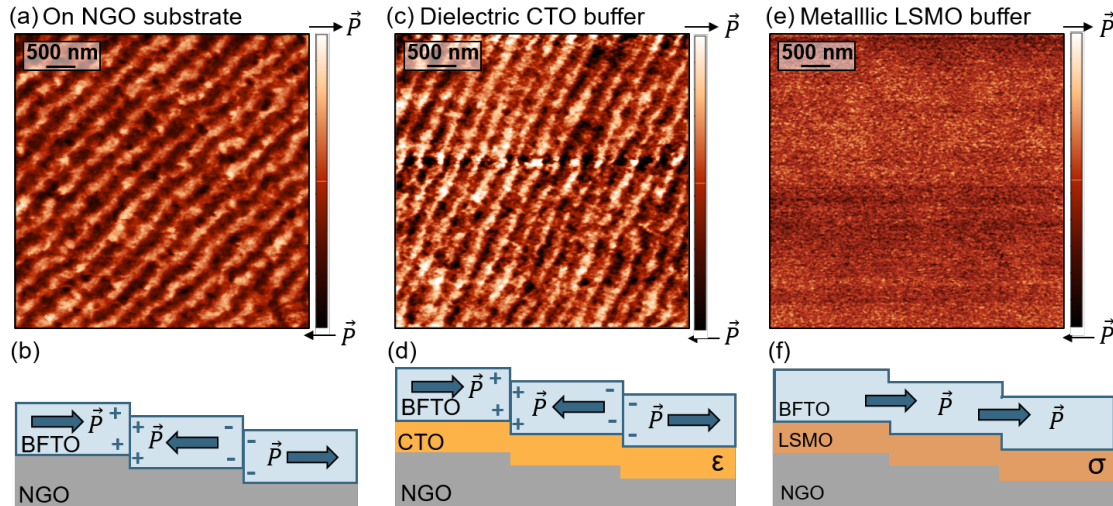
Figure 5.4: Influence of strain and electrostatics on the stripe-domain pattern. (a,b) LPFM image of 1 u.c-thick BFTO layer grown directly onto NGO reveals stripe domains. (c,d) LPFM image recorded on an identical film buffered with dielectric CTO shows that stripe domains are preserved. (e,f) LPFM image of the film buffered with metallic LSMO shows that the domain pattern is no longer observed.

substrate step as schematized in Figure 5.4b.

Insertion of a fully strained dielectric $CaTiO_3$ (CTO) layer of 10 u.c. preserves the stripe-domain pattern in BFTO, shown in Figure 5.4c. The steric OPBs at substrate steps are fully propagated by the coherently strained CTO buffer (Fig. 5.4d). This additionally confirms that the stripe pattern is not caused by the anisotropic epitaxial strain from the substrate as is the case for the stripe-domain BFO films grown on $DyScO_3$ $(110)_o$[85].

However, when 10 u.c. of fully strained, conducting LSMO (x=0.3) buffer are inserted, the domain pattern disappears. We rule out the loss of polarization with ex-situ SHG polarimetry[99] (see section 3.1.3) and, hence, confirm the presence of a uniform in-plane polarization across the entire BFTO film. The uniform polarization in the film and the associated absence of domain walls, sketched in Figure 5.4f, are most likely related to the changes in the interfacial electrostatics. LSMO metallicity enables the supply of screening charges at the interface with BFTO. These carriers can screen the charged vacancies at each structural defect preventing the domain wall formation. While the loss of charged domain walls is clearly disadvantageous for the anticipated use in domain-wall nanocircuits, a single in-plane-polarized domain state can be used for other purposes. The unidirectional in-plane polarization of the BFTO film on LSMO can become instrumental in creating an inversion-symmetry-breaking environment for other ferroelectrics deposited onto it. Indeed, in Chapter 7 we will see how it can induce an unseen domain and domain-wall configuration in a BFO layer grown on top. Most importantly, the knowledge of the BFTO domain pattern

on different buffers allows us to effortlessly switch from ordered stripe domains with charged domain walls to a uniform in-plane polarization, making BFTO attractive for diverse applications.
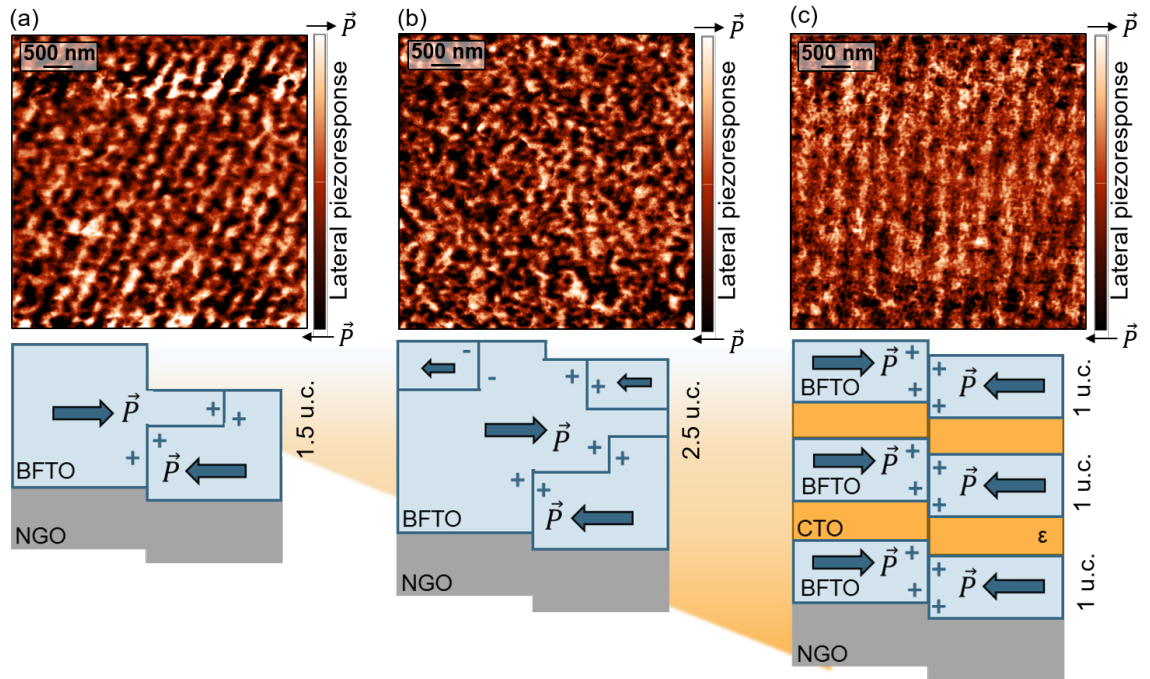
Figure 5.5: Robustness of the engineered ferroelectric stripe domains with increasing film thickness. (a) LPFM image recorded for 1.5-u.c.-thick BFTO grown directly on NGO. (b) LPFM image recorded for 2.5-u.c.-thick BFTO grown directly on NGO. (c) LPFM image recorded for a (BFTO|CTO)$_2$|BFTO superlattice, with 1 u.c. of BFTO and 4 u.c. of CTO in the repeat unit.

Up to this point, we have only considered the OPB-based domain design in ultrathin films of BFTO, in which structural constraints play a decisive role. With increasing film thickness, the weak interlayer coupling and increasing electrostatic energy costs of charged domain walls, however, render the deterministic domain ordering challenging[179]. As a consequence, thicker Aurivillius films show no clear correlation between OPBs and ferroelectric domain walls[109,179]. Specifically, in our films, we see that upon increasing the BFTO thickness by just half a unit cell, the stripe domain pattern gets altered: at 1.5-u.c thickness the stripes start to merge, in this way creating neutral (side-by-side) domain walls instead of the charged ones (Fig. 5.5a). At an even higher thickness of 2.5 u.c. of BFTO (Fig. 5.5b), the stripe domain pattern gets completely lost. We observe the appearance of randomly oriented small in-plane-polarized domains, with only some of their walls remaining charged. This is consistent with the increasing electrostatic cost of maintaining charged domain walls with increasing film volume.

One route to restore the substrate-step imprint in the domain pattern is to sep-

arate the ferroelectric BFTO layers by the insertion of dielectric spacers, creating a dielectric|ferroelectric superlattice[180,181]. The fully epitaxially-strained CTO dielectric inclusions structurally propagate the OPBs through the multilayer thickness, while isolating bound charges in ferroelectric BFTO layers (Fig. 5.4c). This prevents the build-up of electrostatic potential and, hence, the domain disorder despite the increasing thickness. Figure 5.5c shows the PFM image of the domain configuration in the (BFTO|CTO)$_2$|BFTO|NGO multilayer. The characteristic charged-domain-wall ordering of a BFTO monolayer is maintained. An alternative route to the preserved domain pattern despite increasing thickness could be achieved through the use of BFTO compositions with odd n that have an allowed out-of-plane polarization component (see section 4.3). It is worth noting that while the out-of-plane polarization component could enhance the interlayer coupling[140], it would also minimize charge accumulation at the charged domain walls making them less suitable for domain wall nanocircuitry[51,160,182].

5.5 Domain engineering based on structural defect ordering in ferromagnets

As structural defects are pervasive in materials, their controlled appearance at each substrate step could also influence other types of interactions and might impact domain patterns in magnetically ordered compounds, too. LSMO is a colossal magnetoresistive system[78,183] and its magnetic ordering is highly sensitive to both charge doping[94,95,184] as well as structural distortions[184–188] (see section 2.4.4). Previous reports, demonstrating that its magnetic anisotropy can be controlled by substrate topography[189,190] motivate our choice of LSMO (x=0.3) as the model ferromagnetic system to investigate. In this case, however, we no longer expect any appreciable steric OPBs at the interface between LSMO and NGO, because of the similarity between their c-parameters. Nevertheless, LSMO films are ferroelastic[191,192] and the strain induced at the substrate steps could give rise to the formation of ferroelastic domains. As magnetization in LSMO is highly sensitive to any changes in the lattice, the induced ferroelastic domains could alter the magnetic order too.

We grow 10-u.c.-thick LSMO films on NGO (001) substrates. The pseudocubic unit cell of LSMO is under anisotropic epitaxial strain leading to uniaxial in-plane magnetization[88] along $[010]_{NGO} \| [1\bar{1}0]_{pc}$ with a T_C of around 150 K, see Figure 5.6a. The contrast between ferromagnetic domains is measured at 75 K using cryogenic MFM. Figure 5.6c-e show MFM images recorded for LSMO films on the three different NGO substrate morphologies, in analogy to Figure 5.2. Strikingly, the measured ferromagnetic domain configuration is identical to that of the ferroelectric domains in BFTO and, hence, again appears to be dictated by the substrate morphology (see Figures
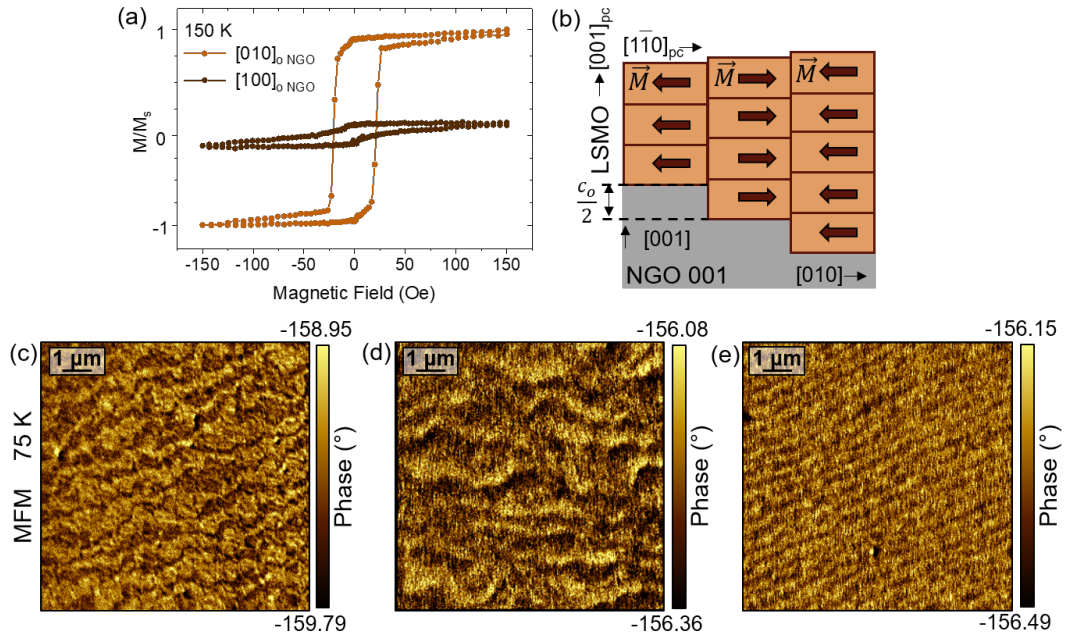
Figure 5.6: Ferromagnetic domain engineering with structural defects at substrate steps.
(a) In-plane uniaxial magnetic anisotropy in LSMO grown on NGO (001). Magnetic hysteresis loops measured at 150 K for a 20-nm-thick LSMO film with an external field applied along the [100] and [010] axes of the substrate. (b) Schematic depicting structural defects in LSMO at every substrate step, which in turn leads to the formation of ferromagnetic domain walls. (c-e) MFM images recorded at 75 K on 10-u.c.-thick LSMO films grown on NGO substrates with three different morphologies, corresponding to Figures 5.2c, e, g, respectively.

5.2c, e, and g for comparison). The ferromagnetic nature of the recorded MFM signal was confirmed by the application of external magnetic fields as well as by heating the films above their T_C. However, it is still under investigation whether the magnetic stray field originates from LSMO domains or domain walls.

Despite the absence of steric OPBs in our LSMO films, LSMO ferroelasticity[191,192] is another source of structural defects. When LSMO films are subject to anisotropic epitaxial strain on NGO (001), they become prone to the formation of twin boundaries along [100]$_{NGO}$ accommodating the shear strain[193]. While twin boundaries in LSMO are usually observed at relatively high film thickness[193], the strain gradient at the substrate steps is likely to trigger the crystal twinning at lower thickness in order to reduce the elastic energy of the system. At the twin boundaries, the octahedral connectivity is lost, hindering the double exchange (see section 2.4.4) between neighboring manganese ions. In conjuncture with the uniaxial magnetic anisotropy perpendicular to the substrate steps, this leads to magnetization reversal at every substrate step, which minimizes the magnetic stray fields, as sketched in Figure 5.6b. Unlike in ferroelectrics, the domain configuration in ferromagnets is only weakly sensitive to the increasing film thickness. This is especially true for in-plane-magnetized films, in which

demagnetizing field plays a negligible role. Hence, we expect the induced domains to be persistent in LSMO over a large thickness range as long as the coherent epitaxial strain is maintained. All this suggests that structural defect ordering at the substrate steps is an effective tool for domain engineering not only in ferroelectrics but also in other classes of ferroic oxides.

5.6   Discussion and outlook

With this work, we proposed a new route to ferroelectric domain engineering via structural defects. Making use of altered structure and susceptibility to non-stoichiometric defects at steric OPBs, we enforced charged domain wall nucleation at every substrate step. In contrast to the commonly used methods for tuning ferroic domain configurations[22,23], we demonstrated extensive control over the domain size, shape, and location by merely tuning the substrate morphology. While our proposed approach is most effective in ultrathin layers, it can be extended to coherently strained dielectric|ferroelectric superlattices. Aside from defining ferroelectric domains, our approach also gives rise to highly defined periodic arrays of charged domain walls that extend over hundreds of microns defining a network of functional elements for nanoscale electronics[51,160,182].

We note that ferroelectric domain engineering through steric OPBs is applicable not only to other classes of layered ferroelectrics with elongated c-lattice parameters[125], but also to classical perovskite ferroelectrics if they are deposited on crystal substrates with disparate out-of-plane lattice parameters[194]. While substrate steps were investigated as a natural way to create and tune ferroelectric domains, artificial means for enforcing the domain wall nucleation can also be envisioned. For instance, one could utilize optical[195] or electron beam[196] lithography to etch out sub-nanometer-height patterns in a substrate. The ferroelectric film deposited after the fabrication would exhibit domain walls following the desired pre-written pattern. Following the analogy to graphoepitaxy[197], during which patterned substrates are used to influence the film crystal ordering, this approach could be coined as graphoferroicity.

With a proof-of-concept experiment employing ferromagnetic LSMO films, we demonstrated that structural defect ordering at substrate steps can be effective for domain engineering in other types of ferroic oxides. Thinking beyond single ferroic orders, an epitaxial combination of the ferroelectric BFTO and ferromagnetic LSMO layers would enable the design of multiferroic spin valves with a complex interaction between the electric and magnetic orders. In particular, an LSMO|BFTO|LSMO trilayer would contain collinear uniaxial in-plane polarization and magnetization and would exhibit a full spatial correlation between ferromagnetic and ferroelectric domains. Such a het-

erostructure holds promise for exotic spintronic applications exploring either domain-wall tunneling effects[198] or lateral differences in tunneling electroresistance[154].

CHAPTER

Achieving zero critical thickness with interfacial polarization continuity

Parts of this chapter are published as:

- E. Gradauskaite, Q. N. Meier, N. Gray, M. Campanini, T. Moran, B. D. Huey, M. D. Rossell, M. Fiebig, M. Trassin. Defeating depolarizing fields with artificial flux closure in ultrathin ferroelectrics, *submitted*.

As seen in the previous chapters, one of the principal assets of in-plane-polarized ferroelectrics is their resilience against depolarizing-field effects, enabling polarization emergence even at sub-unit-cell thickness[118,199]. This is in stark contrast to out-of-plane-polarized layers that exhibit a critical thickness for ferroelectricity of ca. 5 u.c.[30,41] (see section 2.1.4). Even past this thickness, polarization usually only develops if a sufficiently charge-screening environment is provided by metallic electrodes. Despite these limitations, out-of-plane-polarized layers remain the state-of-the-art for integration of ferroelectrics into nanoscale devices[17], allowing simple capacitor architectures that can be miniaturized laterally and require very low voltage for polarization switching.

Here we propose to combine the mutually exclusive benefits of in-plane and out-of-plane-polarized layers in a multilayer architecture in order to combat the detrimental polarization discontinuity at interfaces. At first glance, the epitaxy of in-plane and out-of-plane-polarized layers appears inconceivable in standard perovskite-based systems. This is due to the intrinsic lattice-polarization coupling in epitaxial perovskites, which favors a uniform polarization anisotropy set by the epitaxial substrate strain: tensile leads to in-plane polarization, while compressive enforces out-of-plane polarization. The in-plane polarization in Aurivillius phases, however, arises spontaneously from the unit cell anisotropy and requires no additional substrate strain. The structural

compatibility of Aurivillius and perovskite phases suggests their combination as a possible route to the epitaxy of perpendicular polar anisotropies. This chapter will explore how such heterostructures lead to improved ferroelectric functionality and offer an exciting alternative to metal-based devices.

6.1   Bypassing polar discontinuity at interfaces

The critical thickness for ferroelectricity in out-of-plane-polarized films arises from the discontinuities in polarization at surfaces and interfaces. The surface-bound charges that are not screened lead to a depolarizing field oriented opposite to the polarization. This field can significantly suppress the polarization or, below the critical thickness, even prevent the phase transition to the ferroelectric state entirely. The loss of polarization in the ultrathin regime has become a major challenge for the integration of polar thin films into devices with an increasingly smaller size of active elements. The conventional strategy to fight depolarizing field effects is to use metallic electrodes for screening the bound charge. Metallic electrodes significantly improve the ferroelectric performance and reduce the critical thickness from a few nanometers, measured in the absence of metallicity, to a few unit cells[30,41]. The remaining thickness threshold is rationalized by the finite screening length that metals exhibit, preventing the full compensation of the accumulated bound charge at the ferroelectric surfaces.

While a universal strategy for tackling this deep-rooted problem is yet to be identified, over the last few years there have been reports showcasing specific systems, which display no critical thickness for ferroelectricity. In BFO, a sizeable ($> 4\%$) epitaxial compressive strain[200] was shown to stabilize a super-tetragonal phase at elevated growth temperatures[201]. The significant unit-cell distortion coupled with the increased energy for domain-wall formation was reported to induce polarization from the very first unit cell[201] (Fig. 6.1a). The vast majority of ferroelectrics, however, cannot accommodate such a high epitaxial strain and relax by creating detrimental misfit dislocations, rendering this approach inapplicable.

Coordinating the electrostatic environment of both top and bottom interfaces of a polar film has emerged as another strategy to bypass the polar interfacial discontinuity. The electrostatics of the bottom interface can be engineered with the charged termination of a metallic bottom electrode, i.e. with a localized ionic charge at AO and BO_2 atomic planes of an ABO_3 perovskite oxide (see section 2.1.2 for more details on layer polarization). In the meantime, the top interface is under the influence of adsorbates from the growth atmosphere or the off-stoichiometry of a surface layer. If the contributions of top and bottom surfaces favor the same direction of polarization, they can stabilize it from the first unit cell, see Figure 6.1b. This approach was shown to be successful for Pb-based ferroelectrics as their A-site volatility creates charged defects
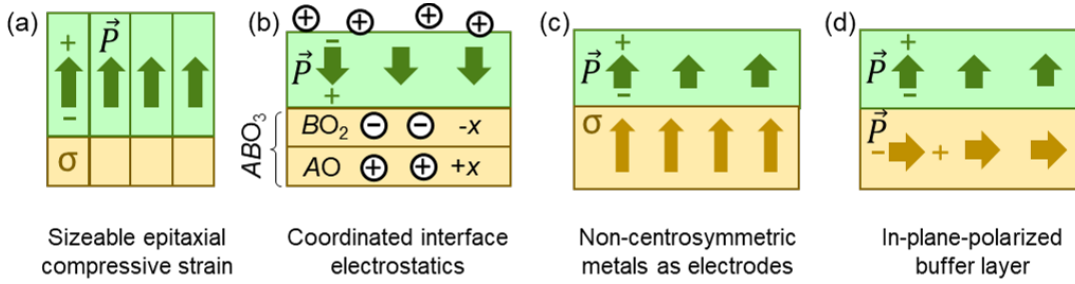
Figure 6.1: Approaches to achieving zero critical thickness in ultrathin ferroelectrics.
Zero critical thickness for ferroelectricity was reported with: (a) high epitaxial compressive strain, (b) coordinated electrostatic environment of both top and bottom interfaces, and (c) "polar metals" used as electrodes. (d) Our proposed approach of using an in-plane-polarized buffer to create polarization continuity at the bottom interface.

at the surface[31,202,203], which unambiguously define the electrostatic contribution of the upper-most layer. Unfortunately, it is hard to predict and control the top-interface electrostatics in ferroelectrics with no volatile elements.

Recent first-principles calculations have revealed that non-centrosymmetric metals, so-called "polar metals", can eliminate the critical thickness for ferroelectricity completely[204]. The introduction of inversion-symmetry-lifting displacements at the ferroelectric interfaces coupled with electrostatic screening (Fig. 6.1c) was shown to be a winning combination to achieve zero critical thickness in a $LiOsO_3|NaNbO_3|LiOsO_3$ capacitor. Such "polar metals" are very scarce as conduction and polarity are deemed to be mutually exclusive[93] and even those that have been discovered to date[205] are structurally incompatible with most of the technologically relevant ferroelectrics, making their implementation in heterostructures elusive.

The aforementioned report of zero critical thickness achieved with "polar metals" suggests that the continuity of polar displacements at interfaces might be just as important as electrostatic screening of bound charges for ferroelectricity to emerge. This shows a need for a strategy shift with regard to stabilizing ferroelectric behavior in the low-thickness range. In line with this, we propose using ultrathin buffer layers that are in-plane-polarized and robust against the depolarizing field as a solution (Fig. 6.1d). This so far overlooked approach of epitaxially combining in-plane- and out-of-plane-polarized layers is likely to create the desired polarization continuity at the interface, mimicking flux-closure domains (see section 2.2) and minimizing surface charge accumulations. Our ability to prepare single-crystalline films of the in-plane-polarized Aurivillius phase that are epitaxially compatible with the out-of-plane-polarized perovskites paves the way for exploring this avenue.

6.2 Epitaxy between Aurivillius and perovskite phases

In order to investigate the effects of polarization continuity at the interface between fer-
roelectrics with perpendicular anisotropies, we first have to establish a route to achieve
epitaxy between the out-of-plane polarized perovskites and the in-plane-polarized Au-
rivillius compounds. The two phases are structurally compatible when their c-axes
are parallel and point out of the film plane, while the perovskite unit cell is rotated
in-plane by 45° with respect to the orthorhombic Aurivillius unit cell. Figure 6.2a
shows a top view of the epitaxial matching between the prototypical out-of-plane po-
larized ferroelectric BTO and the in-plane-polarized BFTO n=4, which are the two
compounds we select for our model heterostructure. The multilayers grown with PLD
are atomically flat (Figure 6.2b) and the inferred epitaxial matching between the two
layers is confirmed using XRD. Figure 6.2c shows ϕ-scans of XRD peaks associated
with the NGO, BFTO, and BTO in-plane reflexes. While the NGO and BFTO unit
cells display a perfect matching, the four-fold symmetry poles, related to the BTO film,
are shifted by 45°. This corroborates the epitaxial matching between the two phases
through a 45° in-plane rotation. BTO films are subject to the compressive epitaxial
strain of -4.1% along $[100]_{\mathrm{NGO}}$ and -2.8% along $[010]_{\mathrm{NGO}}$.

6.3 Zero critical thickness in BTO on an in-plane-polarized buffer

The experimental detection and quantification of critical thickness for ferroelectricity is
rather challenging. As the small sample volume prevents advanced XRD characteriza-
tion of the ferroelectric state, only ex-situ polarization switching, PFM or STEM stud-
ies can be performed as checks for polarization. These measurements, unfortunately,
either require numerous samples of varying thickness[89,206] or are invasive[42,202]. Ac-
cess to the polarization emergence in real-time during the thin film deposition can
overcome this limitation. A pioneering report tracked $PbTiO_3$ unit-cell tetragonality
in situ using X-ray scattering during the deposition[207]. The measurement, however,
required high-intensity synchrotron radiation. In-situ SHG monitoring, in contrast,
can follow polarization emerging in thin films in a laboratory-scale setup[30]. It can be
directly measured in the PLD chamber during the growth of our heterostructures, and,
performed simultaneously with RHEED tracking, provides critical thickness values for
ferroelectricity with unit-cell accuracy (see section 3.1.3).

We start our investigation by monitoring the polarization emergence in BTO when
grown without and with a metallic buffer layer. When a charge-screening environment
is not provided and BTO is grown directly onto an insulating NGO (001) substrate,
more than 6 nm of the material have to be deposited before the onset of the ISHG
signal is detected, as shown in Fig. 6.3a. This suggests a 15 u.c. critical thickness
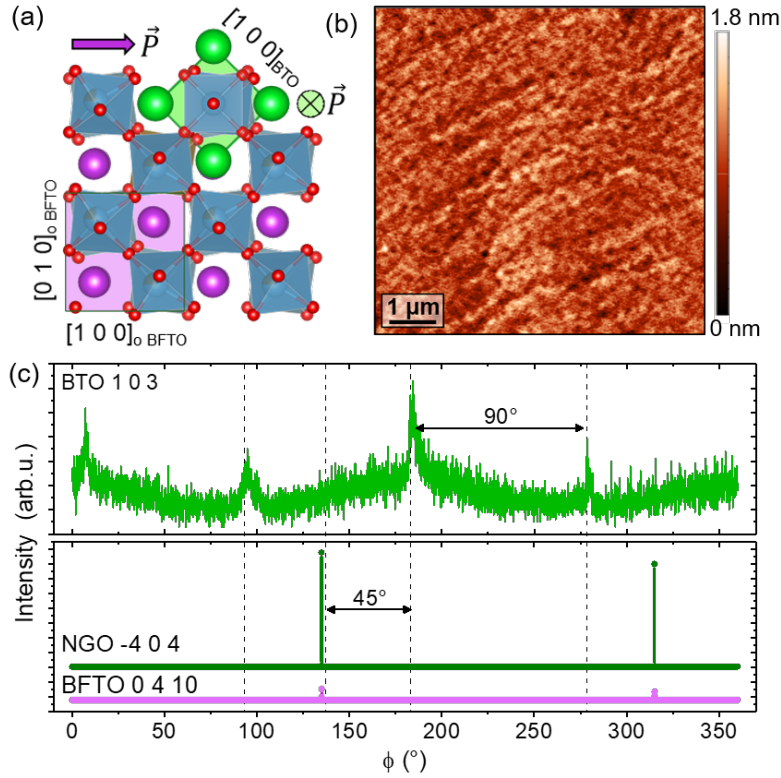
Figure 6.2: Structural analysis of BTO|BFTO|NGO (001) heterostructures. (a) Top view of the epitaxial matching between the BTO and BFTO unit cells. (b) AFM topography scan of the deposited heterostructure. (c) ϕ-scan of NGO (0 4 1), BFTO n=4 (4 0 10), and BTO (103) peaks, in agreement with the epitaxial matching schematized in (a).

for ferroelectricity in these electrostatically unfavorable conditions. For comparison, in Figure 6.3c we show the ISHG yield during the BTO growth on an STO (001) substrate buffered with a standard metallic $La_{0.7}Sr_{0.3}MnO_3$ electrode (LSMO|STO) using identical deposition conditions. The provided charge screening clearly supports the polarization emergence, which now takes place just below the 2-nm-thickness mark. This suggests a significantly improved critical thickness of ca. 4 u.c., consistent with previous reports[30,206,208].

To investigate the impact of the polarization continuity at the bottom interface, we now track the BTO growth on an in-plane-polarized buffer. BTO is deposited on a 0.5-u.c.-thick BFTO layer on NGO (001) (BFTO|NGO). BFTO of this thickness is already ferroelectric and in-plane polarized[118,119,209] (see section 4.4). Strikingly, the increase in the ISHG signal is recorded from the very start of the BTO deposition as shown in Figure 6.3a. This suggests the absence of a critical thickness for the emergence of a spontaneous polarization in BTO on the in-plane-polarized buffer. The identical rate of ISHG increase after passing the critical thickness on both the metallic LSMO and the in-plane-polarized BFTO buffers (Fig. 6.3a) indicates that the BFTO insertion does not affect the polarization value nor the domain state of the BTO film deposited
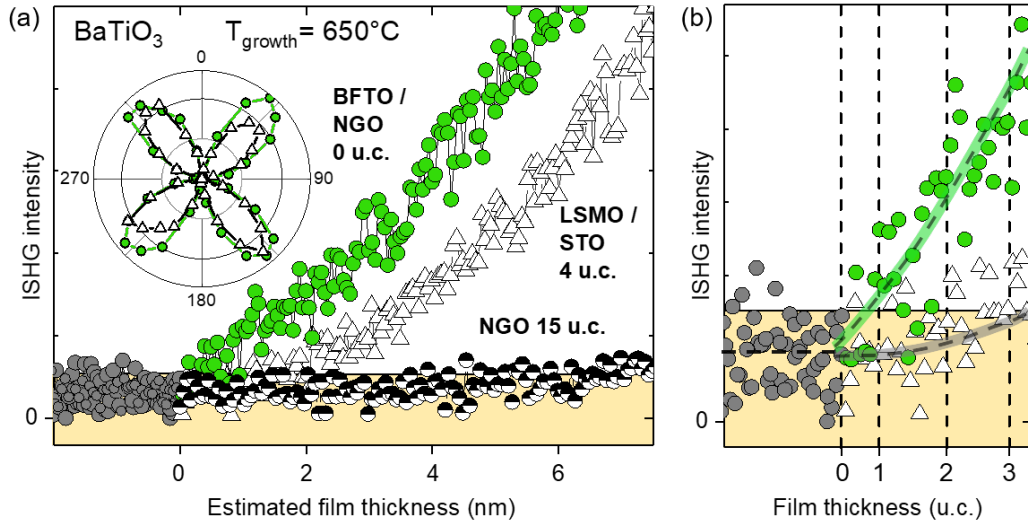
Figure 6.3: Absence of critical thickness for ferroelectricity in BTO grown on 0.5 u.c. of BFTO. (a) ISHG signal tracking the BTO thin-film polarization during the deposition under identical conditions on: an insulating NGO (001) substrate (black), an LSMO electrode on STO (001) (white), and on 0.5 u.c. BFTO on NGO (001) (green). Inset shows the polarimetry scans (polarizer measurements with analyzer set to 0°, see section 3.1.3) of the ISHG signal after the growth completion, recorded for the films grown on LSMO (white) and BFTO (green). (b) The ISHG signal corresponding to the deposition of the first three BTO unit cells on LSMO (white) and on BFTO (green). Dashed lines serve as guides to the eye.

on top. Matching symmetry of SHG polarizer measurements performed in-situ after the growth completion for the two films confirms the expected *4mm* point group of tetragonal BTO, see the inset of Figure 6.3a. The insertion of the in-plane-polarized BFTO, thus, does not change any of the BTO properties but exclusively triggers an early emergence of polarization in the BTO film, as evidenced by the difference in ISHG evolution during the deposition of the first three BTO unit cells, shown in Figure 6.3b.

At first glance, the observed trend for polarization emergence on the two different substrates could be mistaken for a strain effect. NGO as a substrate exerts a nominally higher compressive strain on BTO than STO. Compressive strain is usually associated with a higher spontaneous polarization and ferroelectric T_C[67,81] and could additionally decrease the critical thickness, similarly to Figure 6.1a. The RSM mapping reveals that while BTO is fully strained on STO[30], the BTO layer is partially relaxed on NGO, see Figure 6.4a. This means that the less compressed BTO film shows an earlier onset of polarization, suggesting that the strain-related effects cannot explain the zero BTO critical thickness on the BFTO buffer. In Figure 6.4b we show the comparison of the ISHG signal collected during the BTO growth on the same type of NGO substrate, but on two different buffer materials: metallic LSMO and insulating, in-plane-polarized BFTO. Here, despite the identical strain state, the BFTO buffer supports the emergence of polarization in BTO significantly better than the metallic LSMO, despite the charge screening it provides. All of this allows us to

exclude epitaxial strain as the origin for zero critical thickness in BTO films grown on BFTO and encourages us to consider the in-plane polarization and the buffer structure itself as possible sources of this unusual behavior.
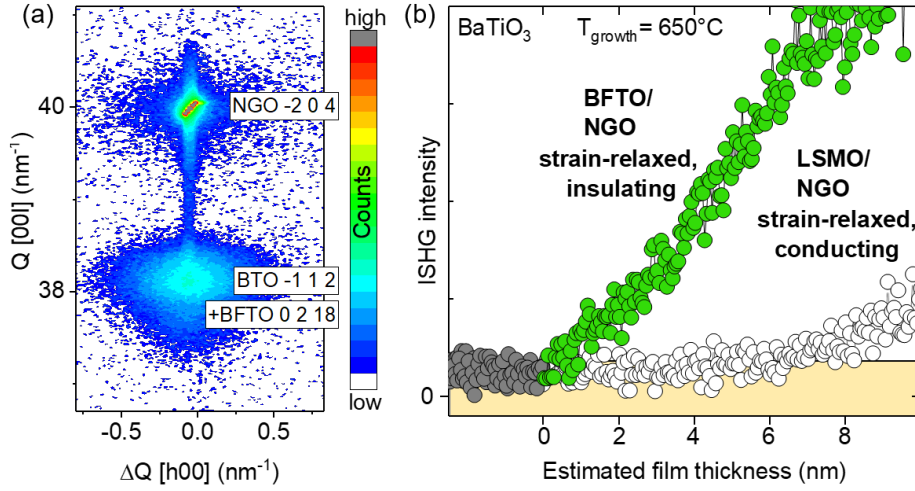
Figure 6.4: Influence of strain relaxation on the critical thickness of BTO. (a) RSM around the substrate peak NGO (-2 0 4) recorded for BTO|BFTO|NGO. (b) The ISHG signal tracking BTO growth on an NGO substrate buffered with metallic LSMO (white) and insulating in-plane-polarized BFTO (green).

While the polarization continuity at the interface can be identified as a macroscopic, all-encompassing driving force for the disappearance of critical thickness in BTO grown on BFTO, we can highlight several microscopic contributions:

(a) *Transfer of inversion-symmetry-lifting displacements.* Polar distortions in the in-plane-polarized layer, such as atomic displacements, tilts, and rotations of perovskite octahedra, could induce ferroelectricity in the out-of-plane-polarized film (Fig. 6.5a). A local microscopic polarization rotation from in-plane to out-of-plane is also highly probable at the interface, considering the already existing out-of-plane off-centering in the uppermost pseudoperovskite layer towards the flourite-like layer in BFTO, at the interface[109] (see section 4.3).

(b) *Minimized stray field* by the partial flux-closure in the heterostructure that minimizes bound charge at the interface and surfaces and, hence, the electrostatic enrgy of the system. To demonstrate this, our heterostructure with perpendicular polar anisotropies can be approximated by an artificial 90° domain wall[210] (Fig. 6.5b).

(c) *Charged domain walls in the BFTO buffer* that appear as a consequence of its in-plane uniaxial anisotropy (see section 5.1). The mobile screening charges at these walls (see section 2.3.2) are available to screen bound charges of the ultrathin polar BTO layer (Fig. 6.5c).

(d) *Layered and charged Aurivillius structure* plays a crucial role too. In addition to spontaneous polarization, BFTO layers are made up of charged ions, which do not add up to zero in each plane - the concept referred to as the layer polarization[28], see section 2.1.2. BFTO films self-terminate with flourite-like planes $[Bi_2O_2]^{2+}$, carrying an accumulation of positive bound charges at the interface, which is not screened due to the insulating nature of the buffer, see Figure 6.5d. These non-screened charges create a field that counteracts the depolarizing field for the upwards polarized BTO.

Therefore, even though the in-plane-polarized BFTO buffer cannot provide a metallic-like screening of the bound charges in the BTO layer, it offers numerous other mechanisms for stabilizing ferroelectricity. These appear to be even more potent than the usual metallicity, enabling the BTO polarization to emerge from the very first unit cell. With this we show that in an adaptively engineered geometry, the depolarizing-field-screening properties of a polarized insulator can even surpass those of a metallic electrode.
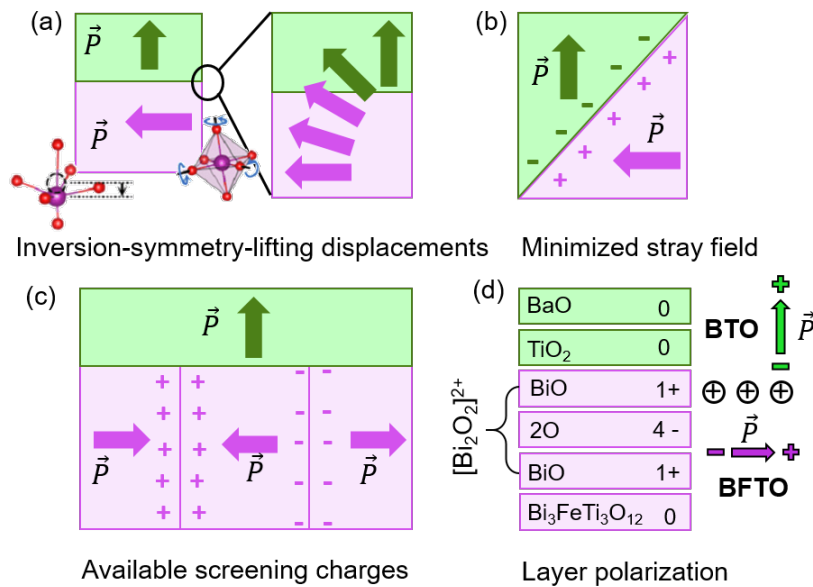
Figure 6.5: Effects stabilizing the BTO out-of-plane polarization on the in-plane-polarized BFTO buffer. (a) Transfer of inversion-symmetry-breaking displacements. (b) Minimized stray field through partial flux-closure. (c) Availability of screening charges from the charged domain walls. (d) Discontinuity in layer polarization at the interface. The resulting positive bound charge at the interface stabilizes the upwards polarized BTO.

6.4 Charged domain walls as a substitute for counterelectrode

To gain a deeper understanding of our heterostructure with its out-of-plane and in-plane-polarized layers, we perform PFM to investigate its domain pattern. The absence of VPFM contrast (Fig. 6.6a) is consistent with a single out-of-plane-polarized domain in the top BTO layer in agreement with the ISHG data. The LPFM (Fig. 6.6b) reveals a pattern of 200-nm-wide stripe domains in the buried 0.5-u.c.-thick BFTO layer. The array of alternating charged TT and HH domain walls is characteristic of the 0.5-u.c.-thick BFTO film[118,209], see section 5.1. Thus, the respective ferroelectric anisotropies seem to persist in the epitaxial bilayer, with the two layers decoupled from one another. The ferroelectric interface between the two polar constituents is reminiscent of a partial flux-closure domain configuration schematized in Figure 6.6c, where polarization discontinuities and resulting bound charge accumulations are considerably minimized (see section 2.2), hence annihilating the depolarizing field effects in the BTO film.
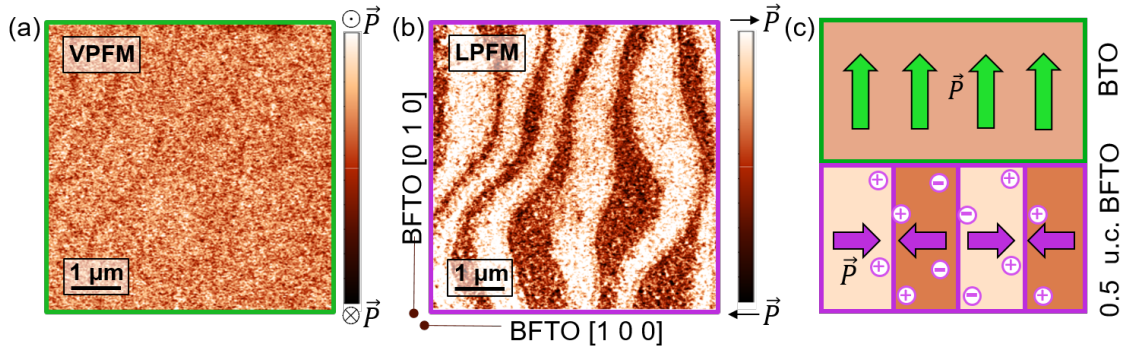
Figure 6.6: Perpendicular polar anisotropies preserved in a BTO|BFTO|NGO heterostructure. VPFM (a) and LPFM (b) scans performed on the heterostructure. (c) Sketch of the deduced domain configuration in the two ferroelectric layers, comparable to a partial flux closure.

Remarkably, we observe that the BTO polarization in our flux-closing heterostructure can be reversibly poled with a biased scanning probe tip (± 5V) when the thickness of the in-plane-polarized buffer is above 2 u.c., see Figure 6.7a. This is rather unexpected since ferroelectric poling ordinarily requires the insertion of a conducting electrode, whereas the BFTO ferroelectric buffer is insulating. A likely explanation could involve the local conduction properties of the charged ferroelectric domain walls[50,142] in the buffer. We thus investigate the thickness dependence of the BFTO domain configuration[118] using tomographic AFM[42].

Figure 6.7b shows the three-dimensional reconstruction of the domain configuration in a 5-u.c.-thick BFTO film. The cross-section of the reconstruction (Fig. 6.7c) reveals that the in-plane-polarized stripe-domain architecture at the bottom interface gradually turns into a random distribution of smaller 180° in-plane-polarized domains

toward the top interface. Most importantly, the domains are columnar throughout the film thickness. Since charged domain walls exhibit different conduction than that of the bulk[50,160], it is reasonable to identify columnar domain walls as conducting channels that thread the film thickness. As the charged-domain-wall density is increasing with thickness and so does the number of total screening charges in the layer, thicker buffer layers enable the BTO polarization switch as shown in the schematic of Figure 6.7d. The local poling experiment additionally reveals an upwards oriented polarization of the pristine BTO films (see Figure 6.7a), which is consistent with the $[Bi_2O_2]^{2+}$ termination of BFTO, preferably screening negative bound charges (see Figure 6.5d). With all this, we establish Aurivillius buffers and their network of columnar charged domain walls as a new platform for metal-free ferroelectric device concepts.
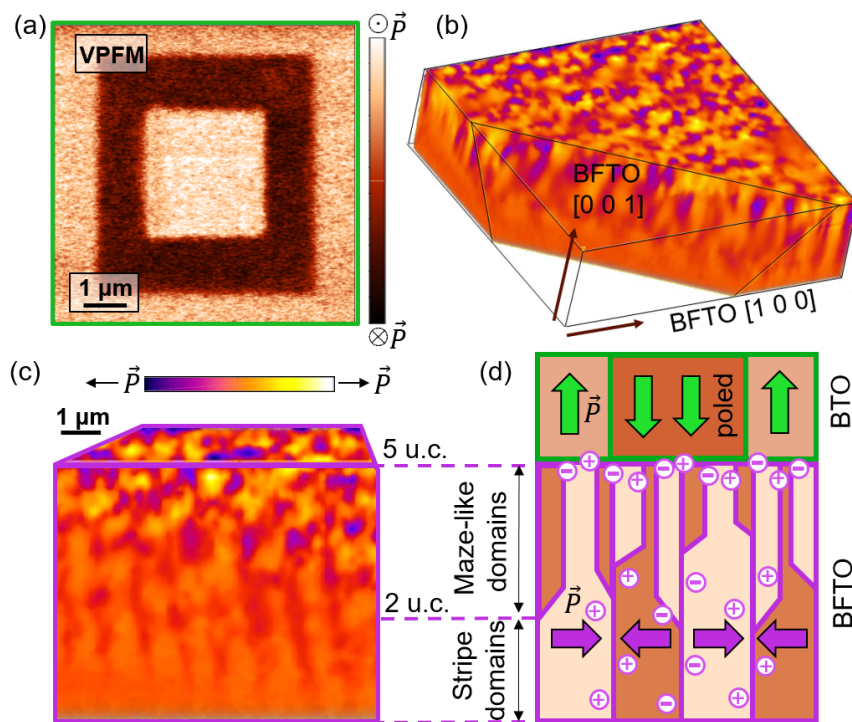
Figure 6.7: Switchability of the BTO polarization in the absence of a metallic bottom electrode. (a) VPFM scan confirming a reversible local polarization switch in BTO grown on 3.5 u.c. of BFTO in the absence of a metallic bottom electrode. (b) Three-dimensional tomographic reconstruction of the spatially resolved piezoresponse in a 5-u.c.-thick BFTO layer.
(c) A cross-section of the reconstruction reveals two different regimes of domain formation. (d) The higher thickness of the BFTO buffer layer results in an increased density of mobile charges at the interface, which enables polarization switching.

6.5 Discussion and outlook

The unconventional epitaxial combination of in-plane- and out-of-plane-polarized ferroelectric layers was explored as a new route for eliminating critical thickness for ferroelectricity. The interfacial polarization continuity between the BTO and BFTO layers stabilizes the BTO out-of-plane polarization from the very first unit cell. This constitutes a paradigm shift in the understanding of ultrathin polar states by showing that polarization continuity at interfaces, encompassing many different aspects ranging from layer polarization to stray-field minimization, could be just as important as electrostatic screening of bound charges. These results not only enrich the fundamental understanding of ultrathin ferroelectric layers but also provide an exciting alternative to metal-based device paradigms from the application point of view, as we showed that the BTO polarization can be reversibly poled in the absence of a metallic electrode but using an in-plane-polarized BFTO buffer instead.

Moving forward, there remains a few ideas and concepts to be investigated further. The demonstrated reversible BTO poling on a thick BFTO buffer with charged domain walls used in place of a bottom electrode relied on the conducting AFM as a top contact. It could, however, be replaced by another BFTO top layer for the conception of a capacitor-like BFTO|BTO|BFTO heterostructure. Such a metal-free capacitor achieved with fatigue-free Aurivillius layers could boost the BTO ferroelectric performance. Charged defects, known to be triggering ferroelectric fatigue[35,175] (see section 2.1.3), are likely to be captured in the layered Aurivillius structure[38], suppressing the onset of the BTO degradation. The use of interdigitated metallic top electrodes on such BFTO-based capacitors could even enable probing whether switching events in the in-plane-polarized BFTO could help to enhance the screening efficiency of bound charges in the BTO layer for its improved switching characteristics.

The new concept of creating polarization continuity in heterostructures with in-plane- and out-of-plane-polarized layers presented here can be extended to other out-of-plane-polarized perovskite ferroelectrics, as will be shown in the next chapter, rendering it a general solution for defeating depolarizing field effects in the ultrathin regime. While in the BTO|BFTO heterostructure both layers preserve their respective polar anisotropy, replacing BTO with a ferroelectric that has its own in-plane polarization components could enable additional domain and domain-wall engineering in the top ferroelectric. Further studies should investigate whether the use of other in-plane-polarized buffers would also result in zero critical thickness in the same way as the Aurivillius phase does. For instance, the Carpy-Galy phases[211,212] are also perovskite-based and exhibit an in-plane polarization, but, unlike Aurivillius compounds, grow in blocks that are neutral in charge. Their integration into heterostructures would allow to discriminate the origins of the uncovered zero critical thickness, by excluding the

discontinuity in layer charges as a possible mechanism.

CHAPTER

Design of domains, domain walls, and their chirality using an in-plane-polarized buffer

Parts of this chapter are published as:

- E. Gradauskaite, Q. N. Meier, N. Gray, M. Campanini, T. Moran, B. D. Huey, M. D. Rossell, M. Fiebig, M. Trassin. Defeating depolarizing fields with artificial flux closure in ultrathin ferroelectrics, *submitted*.

In the previous chapter, we have seen how an insulating, in-plane-polarized BFTO layer can be used in place of a metallic electrode to achieve zero critical thickness for the emergence of ferroelectricity in fully out-of-plane-polarized BTO. The two ferroelectric layers in the heterostructure preserve their respective polar anisotropy, which is favorable for the design of ultrathin memory devices with multi-axial polarization states[17,154]. Nonetheless, interfacing the Aurivillius buffer layer with a perovskite, exhibiting not only out-of-plane but also in-plane polarization components, could enable the coupling between their polar states for new degrees of freedom in the ferroelectric domain and domain-wall engineering.

We, therefore, replace the BTO top layer with a BFO film. BFO is a room-temperature multiferroic magnetoelectric material with a stereochemically active lone-pair as the origin of its polarization (see section 2.4.3). There are eight possible ferroelectric domain states with a spontaneous polarization along the pseudocubic ⟨111⟩-related directions[76], which leads to a rich variety of possible ferroelectric domain and domain-wall configurations[54]. Unlike BTO, BFO thus exhibits both in-plane and out-of-plane polarization components and offers the above-mentioned additional polarization degree of freedom for the design of novel polar states in heterostructures

with Aurivillius layers. In this chapter, we will show how the symmetry-breaking environment provided by the in-plane-polarized BFTO layer can lead to unprecedented domain configurations and domain-wall textures in BFO, which are likely associated with the electric counterpart to the DMI in magnetically ordered materials[213].

7.1 Universality of the approach to zero critical thickness
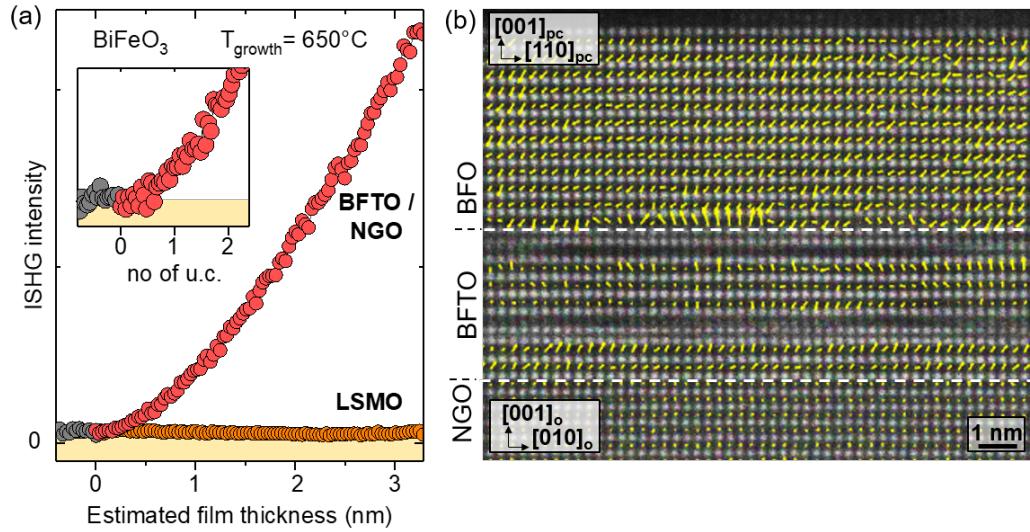
Figure 7.1: Polarization continuity in BFO grown on in-plane-polarized BFTO. (a) ISHG signal tracking the BFO thin-film out-of-plane polarization during its deposition on two different buffers: 1 u.c. of BFTO (red) and 20 u.c. of LSMO (orange), both on NGO (001) substrates. Inset shows the signal collected during the deposition of the first two u.c. of BFO on the BFTO buffer. (b) HAADF-STEM image of the coherently strained BFO|BFTO|NGO heterostructure. Local electric-dipole moments are represented by yellow arrows.

As in the previous chapter, we monitor the ISHG signal during the BFO deposition onto a single-u.c.-thick BFTO layer on NGO (001), see Figure 7.1a. As in the case of BTO, the ISHG yield shows an onset of out-of-plane polarization in the BFO film with the first unit cell deposited (see inset of Fig. 7.1a), thus demonstrating the universality of the approach of using an in-plane-polarized buffer to defeat depolarizing-field effects. The post-growth XRD analysis confirms the (001)-orientation of the BFO film, epitaxially strained on BFTO with the expected 45° in-plane rotation with respect to the BFTO unit cell (see section 6.2). In contrast to BTO, the BFO films remain coherently strained even with the increasing thickness (at least up to 30 nm) with a lattice mismatch of -3.2% and -1.9% along the a- and b-axis of the NGO substrate, respectively. We use atomically resolved HAADF-STEM imaging to map the local electric dipole moments within each unit cell in the BFO|BFTO bilayer with the result shown in Figure 7.1b. Atomic polar displacements in the BFO film, measured from the first

unit cell, in agreement with the ISHG data, confirm the polarization continuity across the interface with a gradual rotation of the electric dipole moments at the BFO|BFTO interface.

To ensure that the disappearance of the BFO critical thickness is not related to compressive epitaxial strain[67,81], which structurally influences the ferroelectric properties and, hence, the ISHG signal (see section 2.5.1), we replace our BFTO buffer with a 20-u.c.-thick, fully strained metallic LSMO (x=0.3) electrode. We observe the suppression of ISHG intensity depicted in Figure 7.1a. In Chapter 6 the insertion of the in-plane-polarized BFTO triggered an early emergence of polarization in the BTO film only, without changing its other ferroelectric properties: the ISHG yield was increasing with the same rate on both the metallic LSMO and the in-plane-polarized BFTO buffers after passing the critical thickness as can be seen in Figure 6.3. Here, with BFO, we observe no ISHG increase at all without the BFTO buffer. This suggests that the in-plane-polarized buffer affects the overall polar properties of the BFO film compared to when it is grown on a metal. XRD studies confirm that both BFO|BFTO and BFO|LSMO heterostructures are coherently strained and STEM imaging shows that in both films BFO has an identical rhombohedral-like unit cell. This implies that structurally the films are equivalent and both should be ferroelectric. The suppressed SHG signal can thus only be explained by the difference in their ferroelectric domain configuration. This calls for further investigations on how the BFO domain pattern is affected by the two buffers.

We start by investigating the BFO domain pattern on the metallic LSMO buffer in the following section. Note that NGO (001) substrates, which are required for epitaxial BFTO films, are not commonly used for the growth of BFO films, hence, the resulting domain configuration is not well established and requires a separate analysis. We then bring additional complexity to the system by inserting 1 u.c. of BFTO between the BFO film and the LSMO electrode and scrutinize the resulting changes to the BFO domain configuration in section 7.3.

7.2   Nanoscale BFO domains on LSMO|NGO (001)

PFM measurements on a 25-nm-thick BFO film grown directly on LSMO reveal a nanoscale domain pattern appearing in both the LPFM and VPFM channels (Fig. 7.2a, b, respectively). The nanoscale domains with alternating out-of-plane polarization components give rise to a vanishing net out-of-plane polarization (P_z=0). This observation explains why we obtain no ISHG signal during the growth (Fig. 7.1a) as the SHG measurement (α=90°, β=90°) probes the net value of P_z (see section 3.1.3) as the ISHG contributions from oppositely out-of-plane-polarized domains interfere destructively.
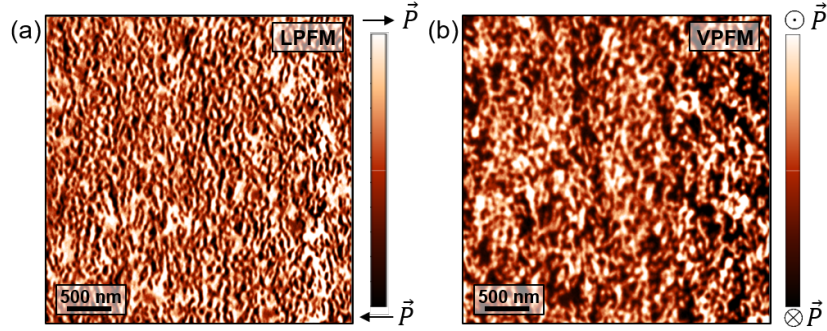
Figure 7.2: BFO domain pattern on LSMO|NGO. Nanoscale domains appear in both the LPFM (a) and the VPFM (b) channels.

Usually, ferroelectric thin films exhibit a uniform out-of-plane polarization when grown on a charge-screening metallic buffer[30]. Therefore, our observation of out-of-plane-polarized domains in BFO on conducting LSMO is highly unusual. Considering the layer polarization in the heterostructure (see section 2.1.2), we would in fact expect the BFO film to be uniformly downwards polarized as the interface between $La_{0.7}Sr_{0.3}O^{+0.7}$ and FeO_2^{-1} atomic planes is negatively charged. Despite this, we detect the presence of domains with both upwards and downwards oriented polarization directions.

To understand the driving force for the unexpected nanoscale domain breakup, we perform further PFM analysis. Here, the pristine BFO domains on LSMO|NGO are too small to be analyzed by PFM to infer the polar anisotropy of the film (see Figure 7.2). Therefore, we locally pole the film using the scanning-probe tip to create domains artificially as shown in Figure 7.3a,b. These created domains are enlarged but still reflect the polar anisotropy of the film. The vectorial PFM (similar to Figure 4.8) reveals that the in-plane projection of the BFO polarization in the film is oriented exclusively along the longer b-axis of the orthorhombic NGO substrate. The anisotropic epitaxial strain induced by NGO, thus, triggers the uniaxial in-plane-polarization in the BFO film.

We combine the knowledge of the polar anisotropy of the film revealed by the poling experiment and the observed contrast at the nanoscale domains to deduce the domain-wall types that appear in the pristine film. As both upwards and downwards polarized domains appear in the pristine film, we conclude that four different ferroelectric BFO domain states are allowed, all contained within the $(110)_{pc}$ plane, shown schematically in Figure 7.3c. We only observe three different BFO domain-wall types out of all the possible domain-wall configurations. These are neutral domain walls with a changing out-of-plane-polarization component: head-to-tail (HT), tail-to-head (TH), or 180° domain walls, sketched in Figure 7.3d. We do not observe any domain walls that preserve a uniform out-of-plane polarization while exhibiting a change in
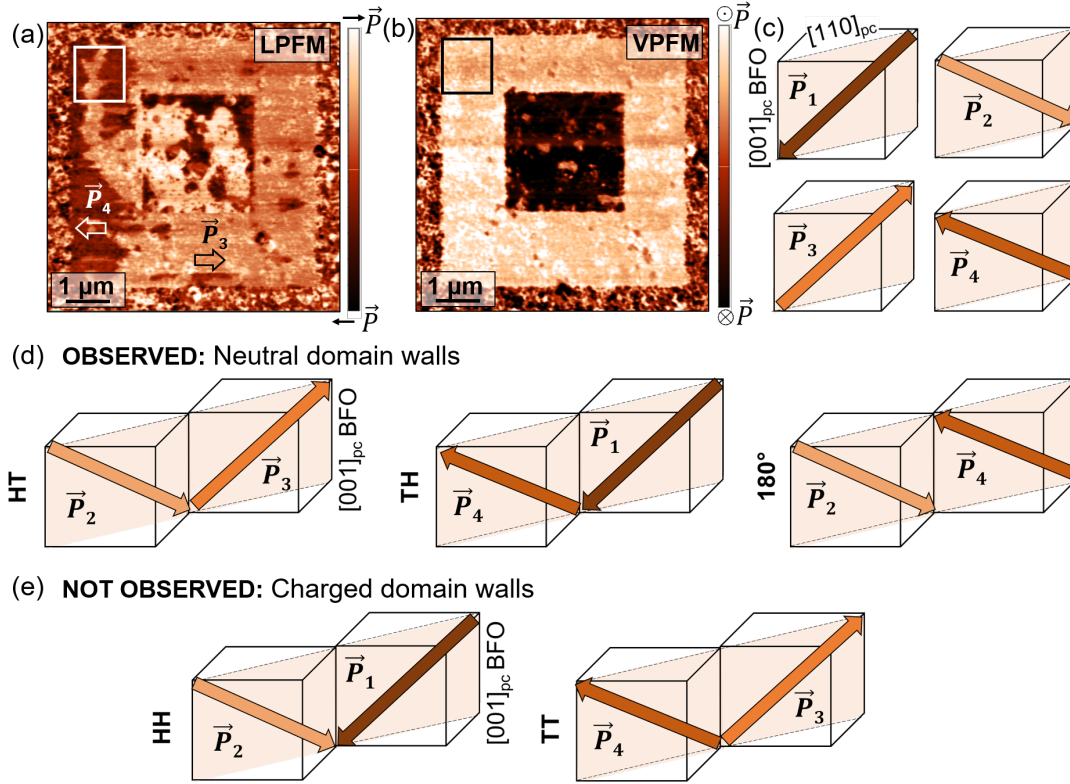
Figure 7.3: Domain configuration and domain-wall types in pristine BFO films grown directly on LSMO|NGO. (a) LPFM and (b) VPFM scans of enlarged domains generated by local electrical poling. Boxes show the areas analyzed with higher resolution in Figure 7.4. (c) Domain states that are found in the pristine BFO film on LSMO. (d) The films exhibit the formation of neutral HT, TH, and 180° domain walls. (e) Charged HH and TT domain walls, which would preserve the same out-of-plane polarization component, are not observed.

the in-plane-polarization component. HH and TT domain walls between $\vec{P}_1$ and $\vec{P}_2$ or $\vec{P}_3$ and $\vec{P}_4$ components would be consistent with such a description (Fig. 7.3e). These domain walls, however, would lead to a charge accumulation, which is electrostatically unfavorable and, hence, are not found in the pristine film. Therefore, it appears that the uniaxial in-plane polar anisotropy in our BFO film causes the formation of out-of-plane-polarized domains in order to bypass any charged-domain-wall formation.

To verify this assumption, we investigate the stability of charged domain walls in the BFO|LSMO written with local electrical poling (marked with $\vec{P}_4$ and $\vec{P}_3$ in Figure 7.3a). Figures 7.4a,b show the zoom-in on these temporarily created charged TT and HH domain walls. We see that the imposed uniform out-of-plane polarization is unstable and the nucleation of domains with oppositely oriented polarization commences after as few as 12 hours, exactly at the contour of the energetically costly, charged domain walls between $\vec{P}_4$ and $\vec{P}_3$ (Fig. 7.4c). This corroborates the resistance of the system against the formation of charged domain walls.

These results show that the uniaxial in-plane polarization in BFO films grown

on NGO (001) triggers the competition between the onset of a uniform out-of-plane polarization and nanodomain formation with neutral domain walls. When deposited onto a metallic LSMO, the BFO film avoids charged domain walls at the cost of losing its net out-of-plane polarization and forming the out-of-plane-polarized nanoscale domains. Let us see how this changes upon the insertion of an ultrathin BFTO buffer just below the BFO film.
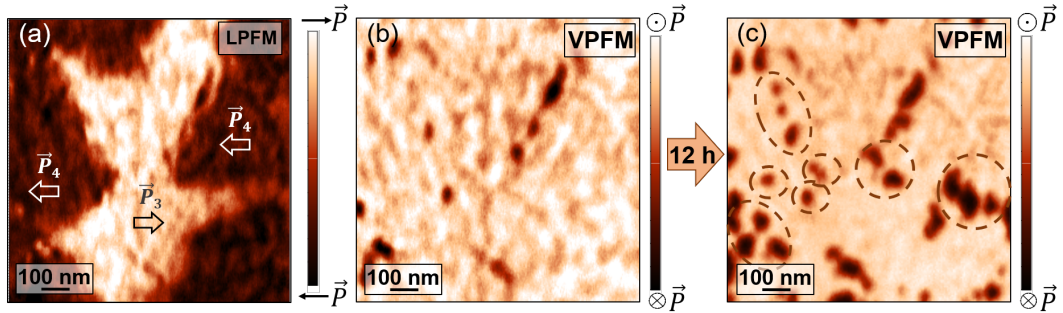
Figure 7.4: Instability of artificially created charged domain walls in BFO on LSMO|NGO. (a) LPFM and (b) VPFM scans of the poled area with charged domain walls, corresponding to the boxes in Figure 7.3a,b. (c) VPFM scan of the same area performed 12 hours later shows a gradual polarization reversal, which nucleates at the contours of the temporarily created charged domain walls.

7.3 Stabilization of net BFO polarization using in-plane polarized buffer

We have already seen that the use of the BFTO buffer can stabilize a non-zero out-of-plane polarization component in BFO (Fig. 7.1). Motivated by this, we now explore whether the configuration of BFO nanoscale domains that appears on LSMO can be tuned by insertion of an in-plane-polarized BFTO buffer between the BFO and LSMO layers. We track the ISHG signal during the deposition of both BFO films, that is without BFTO and with 1 u.c. of BFTO inserted, as shown in Figure 7.5. We now monitor the growth of thicker films (25 nm rather than 3 nm in Figure 7.1a) as we focus on the evolution of domain patterns. We obtain a strong ISHG signal related to the out-of-plane polarization for the BFO grown on BFTO|LSMO|NGO right from the beginning of the deposition (red symbols), while the direct growth on the LSMO-buffered NGO substrate shows a significant suppression of the ISHG signal (orange symbols) in Figure 7.5a in line with section 7.2. The pronounced difference in the ferroelectric properties of the two films in the regime below 10 nm is confirmed with VPFM performed on electrically poled areas (see inset of Figure 7.5a). The lack of ferroelectricity in BFO on the metallic electrode is corroborated by a faint contrast that disappears after a few hours, while the insertion of 1 u.c. of BFTO noticeably

stabilizes the polarization. This contrasting behavior is most likely related to the reduced critical thickness due to the polar continuity at the BFO|BFTO interface, in agreement with section 6.3.
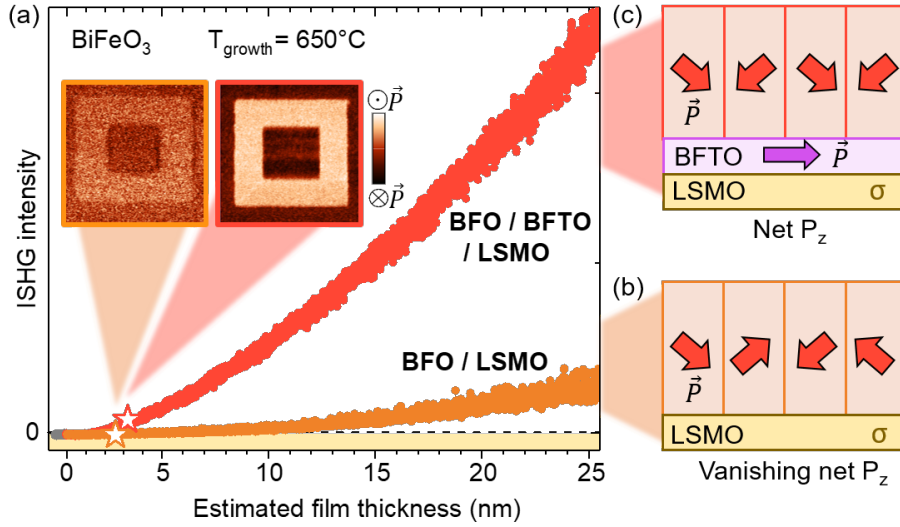
Figure 7.5: Effect of BFTO insertion on the polarization emergence and evolution in BFO. (a) ISHG signal tracking the BFO thin-film polarization during its deposition on LSMO|NGO with and without the insertion of 1 u.c. of BFTO. Inset shows the VPFM images of reversibly poled areas in the two films at the thickness marked with two stars. (b) Sketch of a vanishing net out-of-plane polarization in a 25-nm-thick BFO film buffered with the metallic LSMO. (c) Sketch of a net out-of-plane polarization in a 25-nm-thick BFO film buffered with the in-plane-polarized BFTO.

With the thickness above 12 nm, both BFO films show a finite out-of-plane polarization component P_z associated with the ISHG yield. The intensity of the ISHG signal measured during the growth of BFO growth drastically differs between the two films, however. While we record a strong ISHG signal during the growth of BFO on the in-plane-polarized BFTO buffer, we detect a reduced signal for the BFO films deposited onto the LSMO-buffered substrate. As explained above, this suppression of the ISHG signal is rationalized by the formation of oppositely oriented out-of-plane-polarized nanodomains leading to a reduced value of net P_z (Fig. 7.5b). The BFTO insertion, in contrast, gives rise to a significantly larger ISHG yield and, thus, appears to stabilize a larger value of net P_z. Hence, we can expect a completely different domain configuration in our BFO films on BFTO|LSMO|NGO (Fig. 7.5c).

The PFM analysis of the BFO film grown on the BFTO buffer is shown in Figure 7.6. Large in-plane-polarized domains are detected in the LPFM channel (Fig. 7.6a). The vectorial PFM analysis (similar to Figure 4.8) reveals that the in-plane projection of the BFO polarization is again parallel to the b-axis of the substrate (same as the in-plane polarization axis of BFTO), which we have attributed to the anisotropic epitaxial

strain exerted by the substrate. The VPFM scan reveals a uniformly downward out-of-plane polarization (Fig. 7.6b) (discontinuities that appear at the domain walls will be discussed in the next section) in contrast to a multi-domain configuration observed on LSMO (Fig. 7.2). The uniform out-of-plane polarization in the film is in agreement with the large ISHG yield observed in Figure 7.5a.
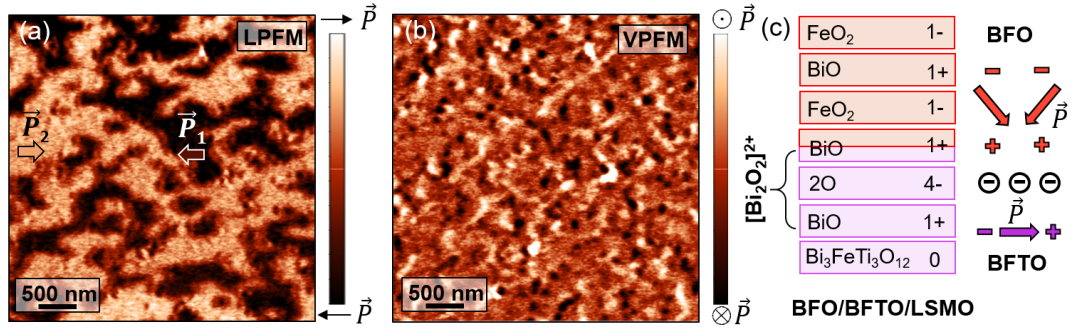
Figure 7.6: BFO domain configuration for growth on BFTO|LSMO|NGO. (a) LPFM scan shows stabilization of two types of in-plane-polarized domains. (b) VPFM scan shows a uniform downwards polarization with some discontinuities at the domain-wall positions. (c) Layer polarization in BFO|BFTO films on LSMO|NGO.

The key to understanding the preference for the uniformly downward polarization is to consider the layer polarization arising from the electrostatics of charged atomic planes in the heterostructure (see section 2.1.2). The BFTO buffer self-terminates with $[Bi_2O_2]^{2+}$ flourite-like plane, as shown in Figure 7.6c. It can be further subdivided into two Bi layers, one of which belongs to the AO plane of the uppermost perovskite of BFTO, while the other becomes the AO plane of the BFO film deposited on top (see Figure 4.6 for more details). This leaves a heavily charged double-oxygen layer carrying an ionic charge of -4 in between. The charge bound to this crystallographic plane cannot be screened due to the insulating nature of BFTO as opposed to the layer polarization in the metallic LSMO. This creates a very strong preference for the downwards polarization in the BFO film so that the film appears to prefer the formation of charged domain walls over that of upwards polarized domains, which we will investigate in the next section.

7.4 Stabilization of non-Ising domain walls in BFO

The insertion of 1 u.c. of in-plane-polarized BFTO not only induces the uniform out-of-plane BFO polarization but also exerts selectivity over the domain states and domain wall types. The strong preference for the downwards polarization combined with the uniaxial in-plane component along the [110]-axis of BFO results in a very unusual selection of the allowed domain states. Out of eight ⟨111⟩-related polarization components

of the pseudocubic BFO unit cell[76], the pristine BFO|BFTO system exhibits only two (Fig. 7.7a), namely those with polarization pointing along $[11\bar{1}]_{\text{pc BFO}}$ or $[\bar{1}1\bar{1}]_{\text{pc BFO}}$, referred to as $\vec{P}_1$ and $\vec{P}_2$, respectively. This gives rise to the formation of in-plane 109° HH and TT charged domain walls, running perpendicular to the uniaxial polarization axes of both BFO and BFTO, as shown schematically in Figure 7.7a. The very same domain walls were shown to be unstable in the film grown directly on the metallic LSMO (see Figure 7.4), demonstrating that the BFTO buffer can be a powerful tool for engineering BFO domain patterns.

The high-resolution LPFM and VPFM scans (Fig. 7.7b,c, respectively) uncover a remarkable feature at the domain walls of the BFO film grown on BFTO. An unexpected out-of-plane signal systematically appears at all charged sections of these walls. This marked behavior, absent in BFO on LSMO|NGO (see Figure 7.4), was consistently observed in BFO layers deposited on BFTO. We verified that it is the intrinsic out-of-plane polarization giving rise to the PFM contrast at the walls and ruled out the possibility of the related artifacts[102,103] (see section 3.2.2.1) by measuring the PFM response upon rotating the sample and changing scanning directions. The appearance of the out-of-plane polarization at the in-plane 109° domain walls points to non-Ising domain walls and a polarization rotation across the walls. Here, the dipole moments are rotating within the plane of the BFO polarization $(110)_{\text{pc}}$, which makes them Néel walls. Previous experimental reports on local polar chiral textures at ferroelectric domain walls involved advanced characterization tools such as non-linear optical imaging[165,214] or HAADF-STEM[215,216]. Here, the unique combination of the uniaxial in-plane polar anisotropy and in-plane 109° walls in BFO provides the ideal experimental setting for the detection of such homogeneously distributed and pronounced ferroelectric textures using standard PFM measurements.

7.5 Polar homochirality as a signature of Dzyaloshinskii-Moriya-like interaction in ferroelectrics

While ferromagnetic walls are usually either Néel or Bloch walls, for a long time it was assumed that all ferroelectric domain walls are Ising-like, in which electric dipole moments locally vanish to minimize the elastic energy related to the lattice-polarization coupling (see section 2.3). Therefore, the observation of the rotational profiles of polarization at BFO domain walls addressed in the previous section is unusual. There is only a handful of experimental observations[165,214,215] of polar Néel or Bloch walls and in these reports both right-handed and left-handed rotation of the local polarization is usually observed with equal probability. Surprisingly, in our BFO films grown on BFTO, we detect only one sense of rotation at the walls making the observed domain-wall texture even more unusual. In particular, an upward polarization component is
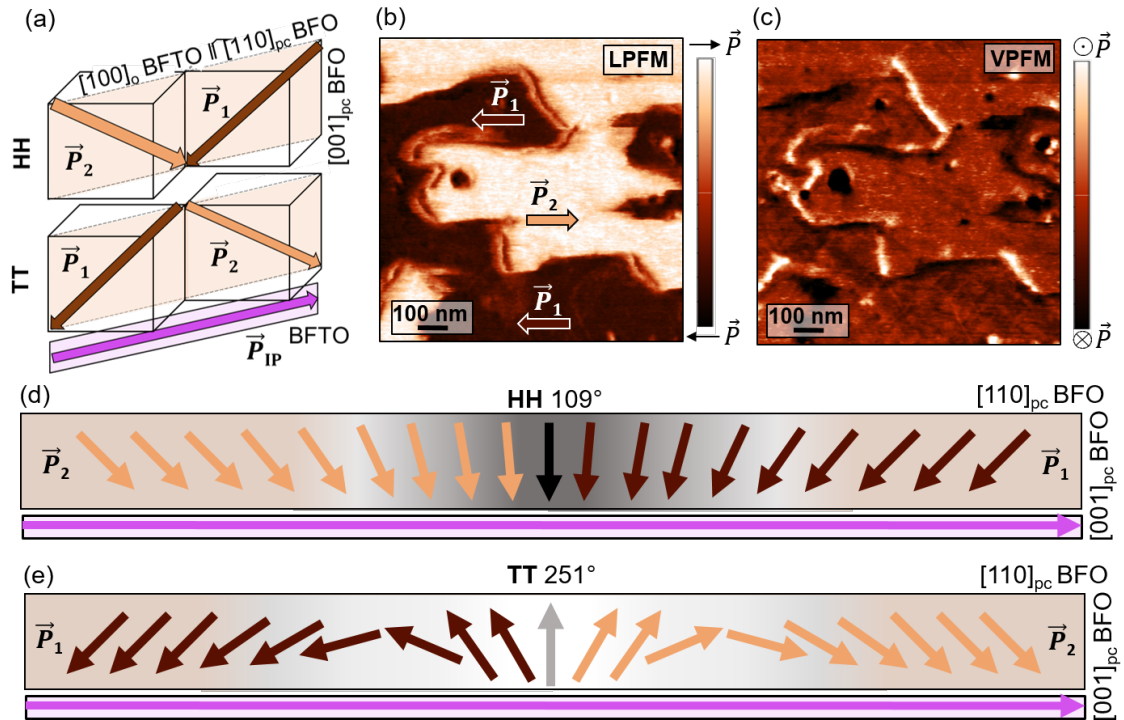
Figure 7.7: Stabilization of homochiral Néel-type 109° domain walls in BFO grown on BFTO|LSMO|NGO. (a) Schematic of 109° HH and TT charged domain walls stabilized by the in-plane-polarized buffer. High-magnification LPFM (b) and VPFM (c) scans show additional out-of-plane polarization components at the charged sections of the domain walls. (d,e) Polarization rotation profiles in the $(110)_{pc}$ plane across the HH (d) and TT (e) domain walls, corresponding to the rotation of electric dipoles via downwards and upwards polarization, respectively. While the polarization reorients over 109° in the HH wall, the TT walls exhibit an unusual rotation of the dipole moments over the longer 251° path.

exclusively detected for the TT walls (bright out-of-plane signal), and a downward component (dark out-of-plane signal) is only observed for the HH walls. This implies a preferred sense of polarization rotation in all charged domain-wall segments of the BFO film and hence a net polar chirality or "homochirality" in our BFO film buffered with BFTO. While in the HH wall the polarization reorients in the form of a direct 109° rotation, in the TT walls the dipolar reorientation prefers a 251° "detour", which would otherwise be energetically costly. This suggests a very pronounced driving force for polar homochirality. Domain walls in ferroelectrics are defined by the angle between the polarization vectors on each side of the wall. Here, in order to highlight the unusual structure of this domain wall and to distinguish it from the well-known appearance of 109° walls in BFO thin films, we propose the notion of a 251° BFO wall.

While ferroelectric domain walls with a preferred chirality are very rare, homochiral domain walls in magnets have already become a crucial component for spintronic applications. The spin texture at such domain walls was shown to enable their deterministic current-driven motion[47]. Such stabilization of a net chirality

at (anti-)ferromagnetic domain walls is usually a consequence of the Dzyaloshinskii-Moriya interaction (DMI)[217,218], which is an antisymmetric exchange interaction that promotes a canted spin configuration with a defined chirality set by the sign of the DM vector instead of the parallel or antiparallel spin alignment promoted by the conventional exchange interaction. The DMI can be described by a microscopic Hamiltonian $H_{DMI} = -\vec{D_{ij}} \cdot (\vec{s_i} \times \vec{s_j})$, where $\vec{D_{ij}}$ is the DM vector defined by the crystal structure. If we consider continuous magnetization with components M_i, rather than spins on single atomic sites $\vec{s_i}$, the term can be rewritten with a set of Lifshitz invariants[219] as $E_{DM} \propto (M_i \cdot \partial_k M_j - M_j \cdot \partial_k M_i)$ (Equation 7.1), where i, j, k are combinations of Cartesian coordinates x, y, z[220]. The Lifshitz invariants[219] used for describing this free-energy term are linear antisymmetric gradient terms of the magnetization components M_i and can be non-zero depending on the crystal symmetry. The DMI can emerge in the bulk of a magnetically ordered material[221], but is also observed in magnetic heterostructures, where it arises from the symmetry breaking at the surfaces or interfaces[47,222]. For instance, in our earlier work[223], we showed that interfaces with non-magnetic layers trigger an interfacial DMI in films of insulating ferrimagnetic $Tm_3Fe_5O_{12}$ (TmIG). The induced interfacial DMI stabilizes its domain-wall homochirality and enables their deterministic current-driven motion for a macroscopic magnetization switching in TmIG.

Here, in close analogy, an interface between BFO and the unidirectional in-plane-polarized BFTO (see section 5.4) breaks the symmetry, and non-collinear polar textures are observed at the BFO domain walls. Based on symmetry arguments, homochiral Néel walls that we observe could be described by an electric equivalent of the DMI component along the $[110]_{pc}$ direction. For this, we can tailor the free-energy term known for the magnetic DMI (see Equation 7.1) to describe the observed homochiral domain walls in BFO by considering antisymmetric interactions between polar displacements P_i rather than magnetization components M_i. This gives rise to a free-energy term describing the DM-like interaction in (anti-)ferroelectrics: $E_{DM}(FEL) \propto (P_i \cdot \partial_k P_j - P_j \cdot \partial_k P_i)$. As we observe $\vec{P}$ along only one in-plane axis x (corresp. $[110]_{pc}$) and the out-of-plane axis z (corresp. $[001]_{pc}$), the terms of the invariant can be reduced to $E_{DM}(BFO|BFTO) \propto (P_x \cdot \partial_x P_z - P_z \cdot \partial_x P_x)$. This free-energy term allows us to reproduce our observation of polar homochirality in BFO with a phase-field simulation shown in Figure 7.8. In the simulation, we combine the derived Lifshitz invariant corresponding to the DM-like interaction and a free-energy landscape that favours the two observed domain states $\vec{P}_1$ and $\vec{P}_2$. The anti-symmetric interaction results in a preferred chirality at the domain walls, favouring downward polarization at the HH walls and upward polarization at the TT walls, similarly to our PFM data shown in Figure 7.7b,c.

For a long time it was assumed that the DMI, characteristic of magnetically or-
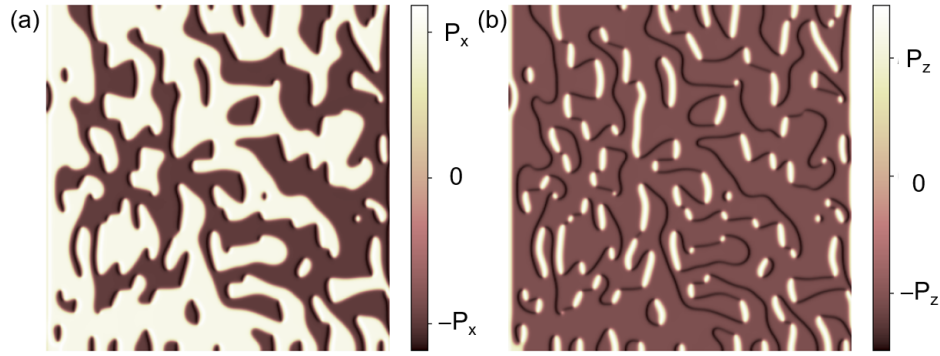
**Figure 7.8: Phase-field simulation of homochiral domain walls in ferroelectric systems
with a non-zero Lifshitz invariant representing a DM-like interaction.** The simulated in-
plane-polarized domains (a) and the emergence of out-of-plane polarization at the domain
walls (b) are comparable to the measured PFM scans of the BFO|BFTO|LSMO|NGO system.

dered systems, had no equivalent phenomenon in electrically ordered materials[224].
However, recent reports[213,225] based on symmetry analysis and first-principles calcu-
lations have now predicted such electrical DM-like terms in a number of ferroelectric
and antiferroelectric systems. While the electric DM-like interaction has a one-to-one
correspondence to the magnetic DMI in terms of symmetry considerations from a phe-
nomenological standpoint[213], its physical origin is of course different. In perovskite
oxides, the polar DM-like interaction is argued to arise from the trilinear interactions
between oxygen-octahedra tilt patterns[213]. Trilinear coupling mechanisms can arise
not only in the bulk of a material, but can also originate from interfaces. Interestingly,
the emergence of "hybrid improper ferroelectricity" in $PbTiO_3$|STO multilayers is also
explained by a trilinear term arising at interfaces that couples two non-polar distortions
and triggers a polar distortion as a result[121]. Similarly, here we could assume that
a combination of interfacial distortions is likely responsible for the electric DM-like
interaction we observe in BFO on BFTO. The ferroelectricity in BFTO arises from
the coupling of three different distortion modes[66], which could propagate over the
interface into the BFO layer. These additional distortions together with the induced
uniaxial in-plane polar anisotropy are likely to cause the appearance of a symmetry
corresponding to that of the magnetic DMI and thus leading to the observed polar
homochirality. This suggests the use of the in-plane polarized BFTO buffer as a route
for the stabilization of polar homochirality, previously shown to be arising from certain
stripe-domain patterns only[226,227].

7.6   Emergence of ferroelectric bubble domains in BFO

Antisymmetric interactions observed in ferromagnetic heterostructures and the interac-
tions we see in our BFO films grown on BFTO have clear similarities: both are induced

by the interfacial symmetry breaking and result in non-collinear domain-wall textures with a uniquely defined chirality. Given this high degree of resemblance, a good starting point for further investigations would be to examine the effects known from magnetic heterostructures in our ferroelectric system. As the interfacial DMI is a surface term, its contribution can be maximized by decreasing the ferromagnet thickness. As a result, the enhanced DMI in ultrathin layers is known to stabilize skyrmions[228]. In our earlier study[229], we showed that skyrmionic bubbles can be stabilized in the aforementioned films of ferrimagnetic and insulating TmIG by significantly decreasing their thickness in order to maximize the interfacial DMI contributions. To tune the balance between different magnetic anisotropies even further, we used ferrimagnetic $Y_3Fe_5O_{12}$ (YIG) as a buffer layer. This soft in-plane-magnetized underlayer helped to reduce the perpendicular magnetic anisotropy in TmIG. The DMI in the TmIG layer was additionally strengthened by the new bottom interface between TmIG|YIG with the same sign of the DM vector as its top interface. These steps allowed us to enforce a delicate balance between different magnetic anisotropies needed to stabilize magnetic skyrmion-like bubbles.
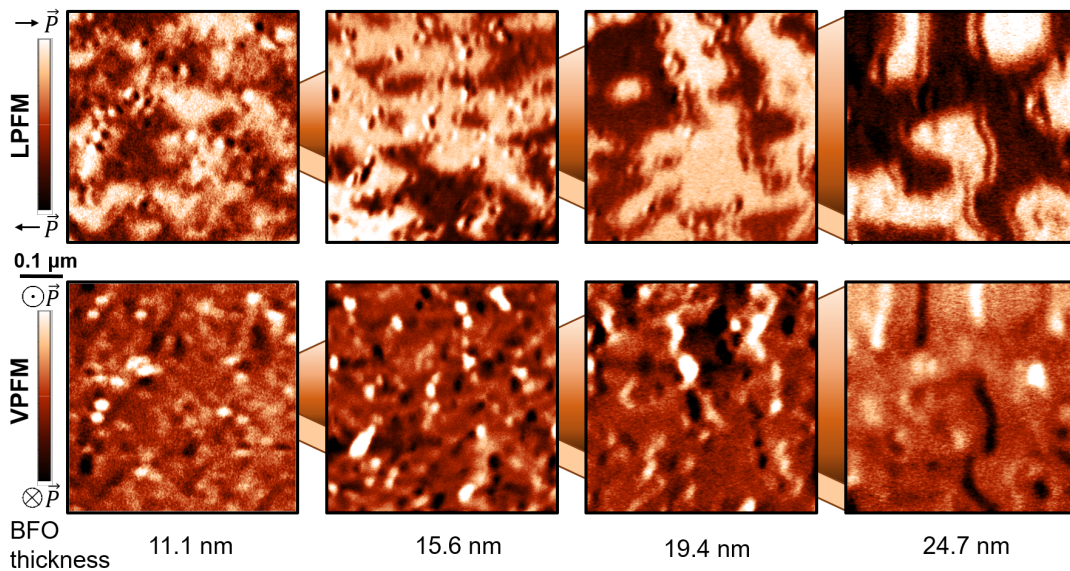
Figure 7.9: Appearance of bubble-like domains in BFO|BFTO upon decreasing the BFO thickness. LPFM and VPFM scans recorded for the heterostructures with different BFO thickness.

A similar approach could be applied to systems with the interfacial polar DM-like interaction. In the BFO|BFTO system only the bottom interface sets the chirality of its polar displacements, hence, there is no need to coordinate different DM-like interfacial contributions. In analogy to our experience with magnets, we reduce the film thickness in an attempt to increase the strength of the antisymmetric interaction and its influence on the domain structure. We investigate how the domain formation is affected by the

decreasing film thickness from the original 24.7 nm, as shown in the Figure 7.9. The
preliminary data reveal that not only do the dimensions of the domains shrink but
also we observe the emergence of point-like features. These bubble-like polar domains
in BFO have upwards polarization in the downwards polarized matrix and exhibit
polarization components pointing both left and right, which could be consistent with
a polar bubble of the skyrmionic nature [224,230]. In future work, it would be crucial
to investigate the response of these bubbles to applied electric fields. Local HAADF-
STEM imaging could also be utilized to map the local electric dipoles in each unit cell
to confirm their non-collinear arrangement. While the PFM-based observation of the
bubble domains alone cannot confirm their skyrmionic nature, the data do not exclude
the possibility that some of the paradigms known for magnetic systems exhibiting the
DMI could be transferred to ferroelectrics with antisymmetric electric interactions.

7.7   Discussion and outlook

In-plane-polarized buffer layers of the Aurivillius phase were established as a powerful
tool for setting the configuration of domain states as well as stabilizing unprecedented
types of domain walls and their textures in multiferroic BFO thin films. Our approach
offers an alternative to currently existing domain-engineering strategies [22] with stabi-
lization of charged domain walls with intricate polar textures as its main asset. Fur-
thermore, the emergence of polar homochirality in BFO domain walls accompanied
by conceptually novel 251° domain walls might constitute one of the first experimen-
tal signatures of the recently proposed electric counterpart to the well-known DMI in
magnetically ordered materials.

From the theoretical standpoint, further studies are required to fully scrutinize the
origins of the observed antisymmetric interaction in BFO|BFTO. The analysis of non-
polar and anti-polar motions in the system could be carried out to identify potential
pathways for trilinear interactions, predicted to trigger the electric counterpart to
the DMI in magnets [213]. For this, we could make use of the DFT-based analysis of
the distortion modes present at the BFO|BFTO interface as well as the experimental
input from the STEM imaging. The identified trilinear interaction would constitute
convincing evidence for the DM-like interaction as the origin of the observed polar
homochirality in BFO|BFTO.

It remains to be explored how the polar chirality in BFO influences its magnetic
order. As BFO is an antiferromagnet with a periodic spin cycloid [70] (see section 2.4.3),
it poses a question of whether the homochirality observed in BFO|BFTO affects the
spin-cycloid behavior as its handedness is determined by the direction of the sponta-
neous polarization. Scanning nitrogen-vacancy (NV) magnetometry could shed light
on how the spin-cycloid propagates at the homochiral ferroelectric domain walls [226,231].

The emerging chirality in the antiferromagntic order could also be detected macroscopically by evaluating the circular dichroism of scattered X-rays[226,227]. The possibility of correlating the chirality of electric dipoles to that of the spin ordering in BFO on BFTO could be key to the creation of antiferromagnetic skyrmions and the possibility to control them electrically with low power.

Further studies should also investigate whether the direction of polarization in the BFTO buffer defines the handedness of the chirality observed at the BFO domain walls. When grown on LSMO, BFTO adopts a single in-plane-polarized domain state (see section 5.4). If the handedness is determined by the direction of the BFTO polarization, then its local reversal could possibly invert the PFM contrast at the domain walls. Identification of areas with opposite handedness in the BFO film grown on top of the poled BFTO layer would verify this assumption.
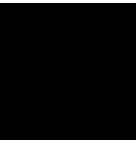
Artificial Magnetoelectric Domain Walls based on Polarization Control at Oxide Interfaces

Parts of this chapter are published as:

- E. Gradauskaite, C.-J. Yang, S. Pal, M. Fiebig, M. Trassin. Magnetoelectric phase control at domain-wall-like interfaces, *in preparation.*

In the previous chapters we have seen how ferroelectric and ferromagnetic order can be controlled by interfacial effects that create a discontinuity in either structure or electrostatics. In this last chapter, we will combine both of these ferroic orders in epitaxial heterostructures to achieve the control of magnetization by acting on the ferroelectric polarization. In ferroelectric random access memories[12], the electric "write" is voltage-driven, hence low-power-consuming and fast, but the electric "read", unfortunately, is destructive and requires a reset step. The magnetic random access memories[15], in contrast, require dissipative currents for writing, but their "read" is non-destructive and straightforward thanks to the established giant magnetoresistance[15]. The quest for combining the best functionalities of both of these memories, namely, the electric "write" and the magnetic "read", fueled the interest in magnetoelectric memories, which enable the electrical control of magnetization via magnetoelectric coupling[8].

Magnetoelectric coupling can be achieved artificially in multiferroic heterostructures[9,23] (see section 2.5.2). While it can be triggered in simple ferroelectric|ferromagnet bilayers, the increasing interest in charged ferroelectric domain walls (see section 2.3.2) motivated us to consider magnetoelectric effects in a special heterostructure with polar layers that adopt the domain-wall-like HH and TT polarization configurations. To artificially design magnetoelectric domain-wall-like objects, we sandwich

an ultrathin ferromagnetic thin film in between two ferroelectric layers and show that its conductivity and magnetic moment strongly depend on the polarization direction of the surrounding layers. Specifically, contrasting properties are achieved for the HH and TT polarization configurations in a close analogy to charged ferroelectric domain walls[142]. Electrical transport and magnetization measurements allow us to identify various phase transitions taking place in our artificial domain-wall-like ferroelectric|ferromagnet|ferroelectric objects upon cooling and relate them to the magnetoelectric charge coupling induced by the ferroelectric layers. With all this, we provide new insights into the electrical control of magnetism at the nanoscale in multiferroic oxide heterostructures.

8.1 Concept of artificial domain walls

Oxide interfaces offer a plethora of phenomena[7,79] that are not found in their bulk constituents. The resulting functionalities, such as superconductivity or magnetoelectric coupling, hold promise for device applications[9,232]. Unfortunately, conventional oxide interfaces lack flexibility once their design is complete owing to their fixed atomic construction, preventing their movement and impeding reversible tuning post-deposition. As an alternative, one could consider ferroelectric domain walls, which are quasi-two-dimensional objects that separate regions of differently oriented electric order within a material and have recently emerged as functional elements for domain wall nanoelectronics[49,51]. Even post-growth domain walls can be created and erased on demand[51,233,234]. Their functionality is determined by the local polarization configuration set by the surrounding domains[49], which can be reversibly manipulated with external fields[48,233]. Nevertheless, charged ferroelectric domain walls suffer from unfavorable electrostatics[50,160] compromising their stability. Merging the functionalities of oxide interfaces and domain walls could combine their respective advantages and enable robust and localized, yet tunable interfacial properties.

We use multiferroic epitaxial heterostructures to achieve domain-wall-like tunability. Artificial charged domain walls can be created with two ferroelectric layers that have opposing out-of-plane polarization directions, while a charge-sensitive functional layer is inserted between them. We select a ferromagnetic layer for the latter, as both its magnetization and conductivity can be modulated by charge doping induced by the adjacent polarity. In this way, the ferromagnetic junction emulates a ferroelectric charged domain wall, where opposite charge accumulation at the interfaces is associated with the HH and TT polarization configurations will trigger contrasting physical properties.

The challenge in achieving such a heterostructure lies in the deterministic design of the polar state in both ferroelectric layers during the growth. In particular, once
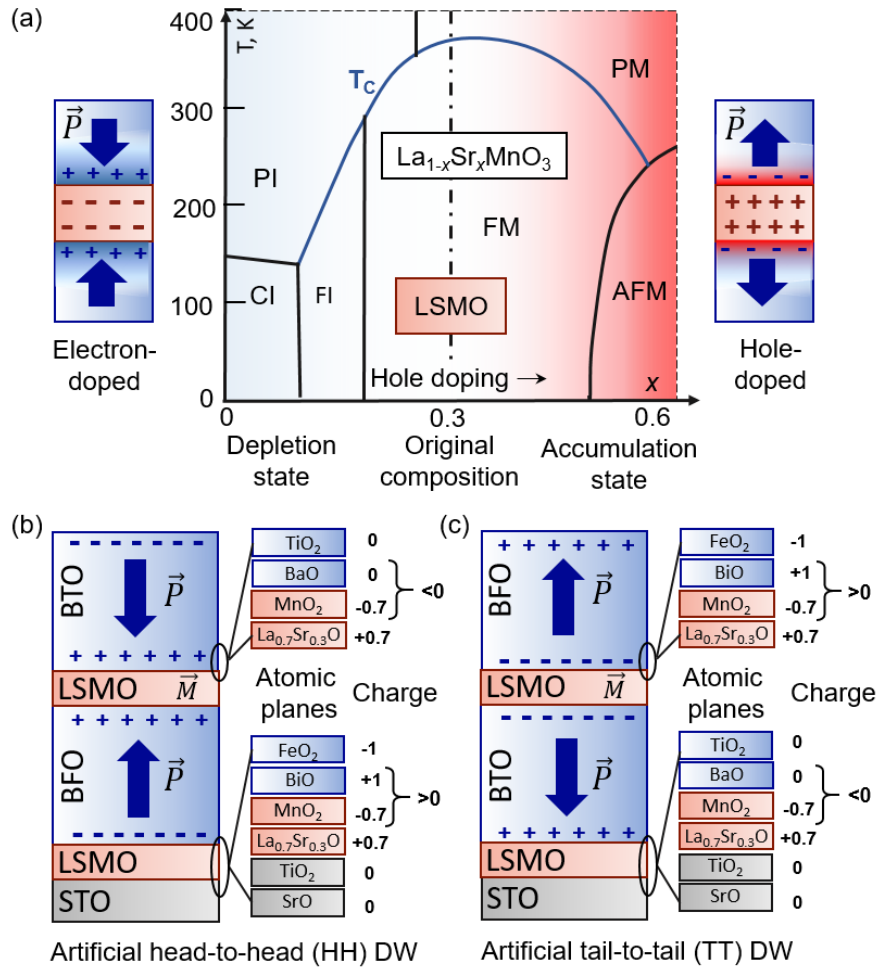
Figure 8.1: The concept of artificial magnetoelectric domain walls. (a) A sketch of the LSMO phase diagram as a function of Sr doping (x). LSMO layers are sandwiched between two ferroelectric layers with opposite polarization directions. The HH polarization configuration results in electron-doped LSMO (blue shading) comparable to reduced Sr doping (x). The TT polarization configuration leads to the hole-doping in the sandwiched LSMO (red shading) comparable to increased Sr doping (x). Abbreviations that denote phases: PM - paramagnetic metal, PI - paramagnetic insulator, FM - ferromagnetic metal, FI - ferromagnetic insulator, AFM - antiferromagnetic metal, CI - spin-canted insulator states. Adapted with permission[43] Copyright 2001, Elsevier Science B.V. (b-c) Sketches of heterostructures resembling artificial HH (b) and TT (c) domain walls.

capped with a metal, polar states can no longer be probed with conventional techniques, making it hard to identify the functional artificial domain wall type, i.e. HH- or TT-like, and the associated interfacial charge accumulation. To overcome this, we propose use of the ISHG monitoring during the heterostructure growth, which allows tracking polar configurations in real-time, as exemplified in our many preceding examples. In complement, we use a combination of SQUID-based magnetometry and terahertz time-domain spectroscopy (THz-TDS) to measure the magnetic moment and conductivity of our heterostructures.

8.2 Design of artificial domain walls

The coexistence of conducting ferromagnetic states with competing insulating or non-magnetic ground states in colossal magnetoresistive manganites[43,235] and the possibility to access them selectively by charge doping motivate our choice of $La_{1-x}Sr_xMnO_3$ (LSMO (x)) system as our active layer to be inserted in the HH and TT configurations of ferroelectric layers. Figure 8.1a shows that variations in the chemical composition of LSMO (x) allow for hole/electron doping and hence for the navigation within the LSMO phase diagram[43,235]. Similar changes to LSMO properties can be achieved through magnetoelectric charge coupling at the interface between LSMO and a ferroelectric[236], see section 2.5.2. When the ferroelectric polarization is pointing towards the LSMO layer, positive bound charges appear at the interface. To screen these charges, negative carriers accumulate in the LSMO on the other side of the interface. In contrast, when the polarization is pointing away from the LSMO, negative bound charges of the ferroelectric are screened with an accumulation of positive carriers in the LSMO.

These charge accumulations result in a reversible control of LSMO physical properties similar to the control exerted by the chemical substitution. These interfacial effects could be maximized by *sandwiching* an LSMO junction in between two ferroelectrics that are both pointing either towards or away from the ferromagnetic layer in the HH or TT polarization configurations, respectively. The local charge accumulation at the two distinct artificial domain wall states effectively acts as electron doping for the HH configuration (depletion state, blue) and hole doping at both interfaces for the TT configuration (accumulation state, red), respectively[94–96] (Fig. 8.1a). A 30%-substituted LSMO ($La_{0.7}Sr_{0.3}MnO_3$, marked by a dashed line) is chosen for our study as it grants a high Curie temperature (T_C) and enables phase transitions upon both electron and hole doping.

Reference magnetic measurements performed on single in-plane-magnetized LSMO layers of 7, 15, and 30 u.c. grown directly on STO substrate and without the interfacial electrostatic doping contributions are shown in Figure 8.2. Even though higher thickness is related to higher T_C values (Fig. 8.2), the interfacial charged doping at interfaces with ferroelectric layers usually extends over a few LSMO unit cells only[33,236,237]. Therefore, a thickness of 15 u.c. appears to be a reasonable compromise, offering room-temperature magnetization, while still allowing for interfacial effects to be dominant[238–241] in the domain-wall-like [ferroelectric|LSMO|ferroelectric] multilayer. Additionally, with our reference measurements, we identify LSMO layers as soft ferromagnets with a coercive field sensitive to the layer thickness, see Figure 8.2b.

BTO and BFO ferroelectrics are selected as the polar building blocks, as they tend to adopt opposing out-of-plane polarization on the same charged buffer layer. This is
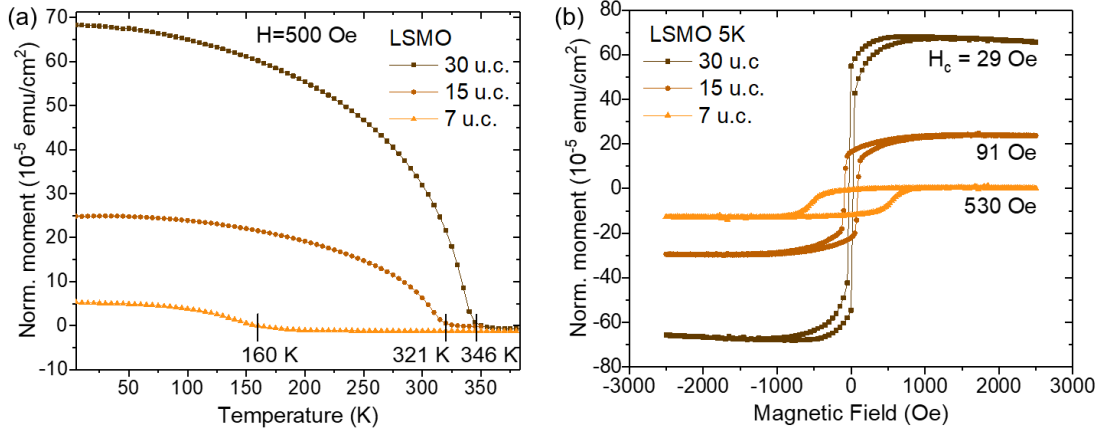
Figure 8.2: Magnetic properties of ultrathin LSMO films measured with the field applied in in-plane. (a) Magnetic moment measured versus temperature. (b) Magnetic hysteresis loops recorded at 5 K.

because BTO is made up of neutral atomic planes, while BFO has a significant layer polarization[28] (see section 2.1.2). If we consider the MnO_2-terminated LSMO buffer layer, the interface between LSMO and BFO will have a net positive charge favoring up polarization, while the interface between LSMO and BTO will have a net negative charge, hence inducing down polarization (Figure 8.1b,c). In this way, we obtain the HH and TT configurations by simply inverting the BFO and BTO growth sequence, as shown in Figure 8.1b,c. Note that an additional LSMO electrode is inserted below the domain-wall-like trilayer [top ferroelectric|LSMO|bottom ferroelectric] in both heterostructures. This is not only to set the polarization directions appropriately but also to provide the electrostatic screening environment for the bottom ferroelectric layer. By making this LSMO buffer exactly as thick as the functional LSMO domain-wall-like layer, we will be able to compare their properties in response to different interfacial contributions, i.e. only a single or two interfaces with a ferroelectric layer. STO (001) is chosen as a substrate as it is shown to reduce the octahedral tilts in LSMO, in this way enhancing its magnetization and T_C[187,242,243].

8.3 Monitoring the growth of artificial domain walls

We grew our HH [BTO|LSMO|BFO] and TT [BFO|LSMO|BTO] heterostructures by PLD on TiO_2-terminated STO (001) substrates. In order to follow the polar state of each layer during the epitaxial design, we use ISHG. The ISHG signal is measured in reflection geometry in order to detect the relevant out-of-plane component of polarization[30] in our HH and TT heterostructures. In addition, RHEED is used to simultaneously monitor the thickness of every layer in the heterostructures.

The in-situ access to polarization throughout the entire multilayer deposition gives
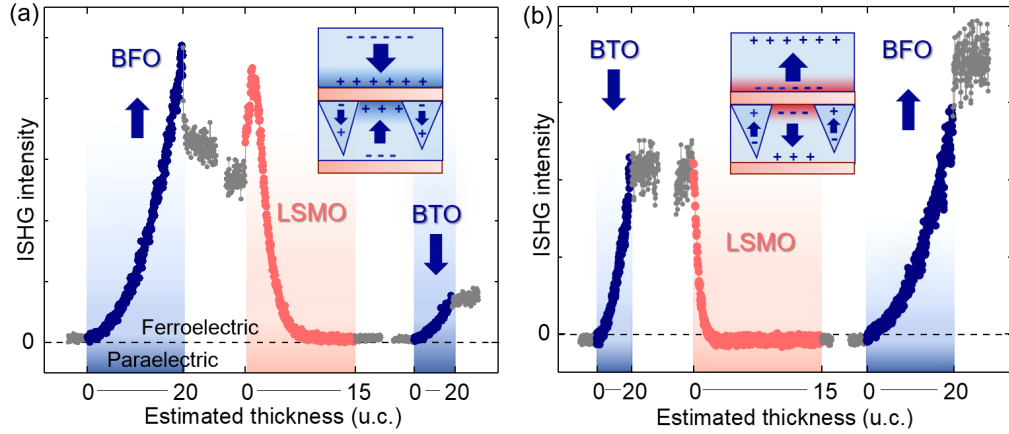
Figure 8.3: ISHG tracking during the deposition of heterostructures with artificial magnetoelectric domain-wall-like elements. Growth of the HH (a) and TT (b) heterostructures monitored with ISHG. Horizontal axes represent the subsequent deposition of the layers comprising each heterostructure. The insets show the polarization configurations in both heterostructures and the resulting interfacial doping of the sandwiched LSMO layers: electron doping (blue shading) and hole doping (red shading).

us essential information on the polarization configuration in our heterostructures. Figure 8.3 shows the ISHG signal collected during the growth of the two heterostructures corresponding to the HH and TT polarization configurations. The signal of the first ferroelectric layer in both heterostructures starts increasing after ca. 5 u.c. of BFO or BTO have been deposited, consistent with the critical thickness for ferroelectricity past which the polarization is increasing continuously[30]. A difference in the ISHG yield obtained for BFO and BTO layers is caused by the different $\chi^{(2)}$ components and their values, see section 3.1.3, as well as dissimilar values of bulk polarization associated with the two compounds.

When the ISHG signal is tracked during the coverage with LSMO, we observe it to drop to the background level in both heterostructures. As the LSMO layer is too thin to explain the observed behavior only by absorption of the laser light, we relate the loss of the intensity to the formation of 180° domains in the capped ferroelectric layer as a response to the low charge-screening efficiency of LSMO at its early growth stages[244,245]. As mentioned earlier, since domains with opposite polarization emit SHG with a 180° phase shift, the observed decrease in the signal is a consequence of the destructive interference between them. During the deposition of the second ferroelectric layer, the ISHG yield reemerges past the critical thickness and continuously increases, suggesting that a single-domain state is stabilized in the second ferroelectric layer. The polarization directions of the constituent layers in the HH and TT heterostructures set via means of the layer polarization were verified with PFM after the deposition.

8.4 Physical properties of artificial domain walls

By simply inspecting the ISHG signal collected during the deposition of the HH and TT heterostructures, we can already deduce that the LSMO junctions behave differently when embedded in different polarization configurations. The ISHG yield corresponding to the BTO layer is significantly diminished in the HH compared to the TT heterostructure despite the identical growth conditions. A likely explanation of the suppressed polarization in BTO is the reduced conductivity and hence the screening efficiency of the LSMO interlayer when it is in the depletion state induced by the HH configuration. This motivates us to investigate the physical properties of the LSMO junctions, specifically their conductivity and magnetization, further.
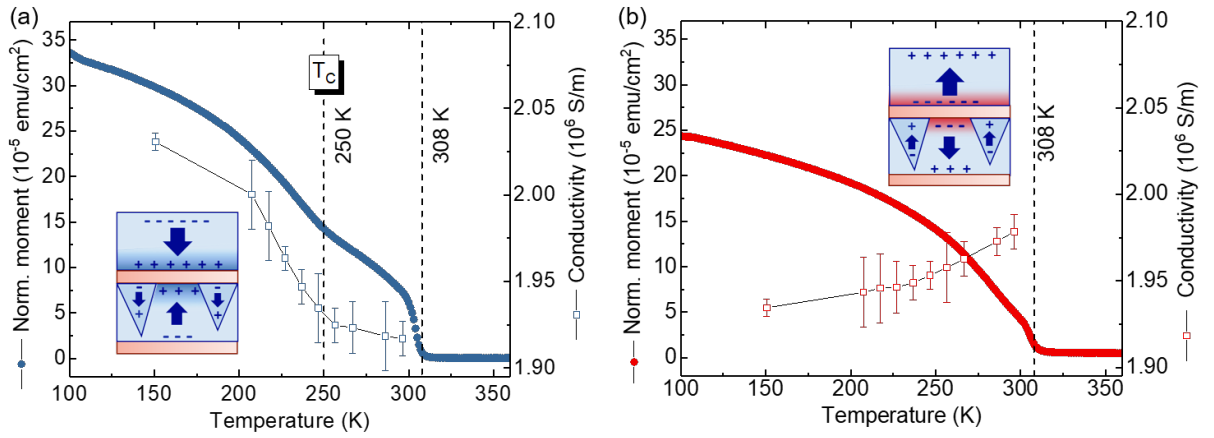
Figure 8.4: Properties of the HH and TT heterostructures measured upon cooling. Changes in magnetization and optical conductivity (error bars correspond to the standard deviation) with respect to the temperature measured for the HH (a) and TT (b) heterostructures. The insets show the polarization configurations in both heterostructures and the resulting interfacial doping of the sandwiched LSMO layers: electron doping (blue shading) and hole doping (red shading).

A combination of SQUID magnetometry and THz-TDS was employed to extract the magnetization and optical conductivity of the LSMO layers directly from the as-grown HH and TT multilayers. Figures 8.4a,b show changes in magnetic moment and conductivity upon cooling down the HH and TT heterostructures, respectively. Both heterostructures exhibit a common magnetic signature with T_C of about 308 K, which can be ascribed to the LSMO buffer layers in both samples. The T_C is comparable to the one measured for a single LSMO layer of 15 u.c. (Fig. 8.2a) in line with insignificant interfacial charge doping arising from the bottom multidomain ferroelectric. In the HH structure, an additional ferromagnetic transition is discernible at 250 K accompanied by a significant increase in conductivity, as evidenced by changes in optical conductivity. After consulting the LSMO phase diagram (Fig. 8.1a), we can ascribe this behavior to the phase transition from PI to FM, consistent with electron doping $\Delta x < 0$ in the

99

artificial HH wall (the sandwiched LSMO layer). No additional phase transitions are captured for the TT sample, in which the magnetic response and conductivity are both dominated by the buffer layer response down to low temperatures. This is consistent with a phase transition from PM to AFM upon cooling the artificial TT wall (the sandwiched LSMO layer), which is hole-doped $\Delta x > 0$. During this phase transition, neither the magnetic moment of the domain-wall-like TT element nor its conductivity change, in agreement with our data.

These measurements reveal that with our artificial HH and TT domain walls, we can span four different phases in LSMO junctions: PM, PI, FM, and AFM, as schematized in Figure 8.5. It is worth noting that aside from the effective electrostatic doping at the interfaces, other factors, such as orbital ordering imposed by epitaxial strain[246], polar discontinuities[247], and orbital hybridization[248] also play a role in the observed changes in magnetization and conductivity. Nevertheless, here we restrict ourselves to the consideration of the bulk LSMO phase diagram since it is sufficient to explain the observed behavior.

Figure 8.5: Magnetoelectric LSMO phase control. Different LSMO phase transitions achieved upon cooling down (−T) the HH and TT heterostructures. Different properties arise from the electron and hole doping, shaded in blue and red, respectively, induced by the adjacent ferroelectric layers. The domain formation in the bottom ferroelectric layers affecting the levels of interfacial doping is depicted schematically.

Aside from changes in conductivity and magnetization, variations in magnetic coercivity can likewise indicate phase transitions in multiferroic heterostructures. Figure 8.6a shows magnetization curves of the HH and TT heterostructures recorded at 300 K. The two very similar magnetization curves are in line with the common magnetic response originating from the bottom LSMO electrodes, while the artificial domain walls are paramagnetic at this temperature. Once cooled down below T_C of the HH domain-wall-like element (250 K), at 200 K, we measure double hysteresis. This suggests the presence of two independent magnetic responses in the HH heterostructure: one of higher coercivity and lower magnetization compared to the other (Fig. 8.6b). The softer magnetic response of the HH heterostructure is very similar to that of the TT heterostructure and, hence, must arise from the bottom LSMO electrode. The harder magnetic response with the lower magnetic moment emerges from the artificial HH wall (the sandwiched LSMO layer) itself. The enhanced coercivity (32 Oe versus 7 Oe) points to a reduction in the effective ferromagnetic layer thickness (see Figure 8.2b and[244]), so that we can assume a partial ferromagnetic ordering in the domain-wall-like LSMO layer. This suggests that the ferromagnetic

phase is in coexistence with the PI phase at the interfaces of the domain-wall-like HH element. The artificial domain-wall-like TT element exhibits no magnetic signature at this temperature, corroborating the inferred antiferromagnetic ordering.
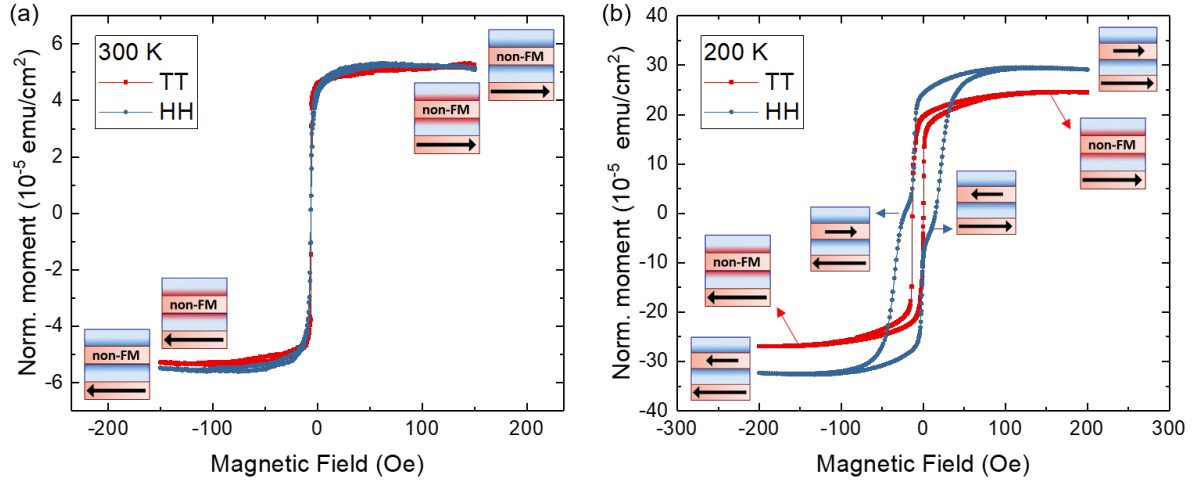
Figure 8.6: Magnetic hysteresis curves of the TT and HH heterostructures. Magnetization dependence on applied magnetic field at 300 K (a) and 200 K (b). Sketches show the heterostructures and the associated configurations of magnetization (black arrows) and their dependence on the magnetic field applied.

8.5   Tailoring electrostatics of interfaces to maximize interfacial magnetoelectric coupling

Even though the results presented up to this point confirm the expected magnetoelectric coupling in our proof-of-concept artificial HH and TT domain walls, the interfacial charge doping of our LSMO junctions may possibly be boosted even further. One major challenge that remains to be overcome are the changing interfacial electrostatic conditions during the growth[67], referred to as transient electrostatics, which give rise to the domain formation in the lower ferroelectric layer. The presence of domains significantly minimizes the charge accumulating at the interfaces of both LSMO layers of the two heterostructures.

The unwanted multidomain formation in the lower ferroelectric layers during the deposition of the HH and TT heterostructures occurs as a result of two effects: (i) the polarization of the bottom ferroelectric layer is suppressed[31,203] even before it is capped with LSMO, making it prone to the domain formation, as sketched in Figure 8.7a. This is because the electrostatic contributions of its top and bottom interfaces cannot screen the bound charges associated with a uniform polarization[31] (see section 2.1.2); (ii) the first few unit cells of the LSMO layer gradually covering

the ferroelectric layer during the deposition are not conducting enough[244] to provide a sufficient electrostatic screening of the bound charges in the lower ferroelectric layer, which breaks up into domains in response[67] (Fig. 8.7a).
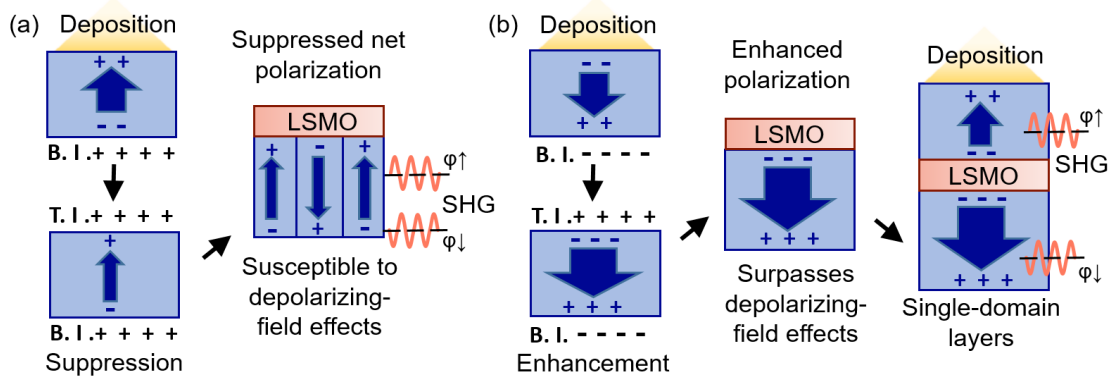
Figure 8.7: Coordinated interfacial electrostatics to overcome transient depolarizing field effects. (a) Mismatch in electrostatics of the top and bottom interfaces results in a suppressed polarization, susceptible to splitting into 180° domains upon the capping with a metal. (b) Coordinated electrostatics of the top and bottom layers enhance the polarization, which can then surpass the depolarizing-field effects and maintain a uniform polarization direction despite the capping with a metal. The arrows show polarization in the ferroelectric layers (blue) with their sizes being proportional to the polarization value in the films, i.e. suppressed or enhanced[31]. T.I. and B.I. correspond to the top and bottom interfaces, respectively, and their electrostatic contributions. SHG waves (sketched in orange) emitted from areas with opposite polarization have a 180° phase shift.

While we cannot act on (ii), we can tune (i) to protect the bottom ferroelectric layer from the breakup into domains. To do this, we strengthen its polarization by coordinating the electrostatic contributions of both of its interfaces[31,203] (see section 6.1) by imposing the interfacial charge accumulations that stabilize and enhance a uniform polarization, as shown in Figure 8.7b. This could allow us to surpass the depolarizing-field effects and maintain a net polarization in the ferroelectric layer during the LSMO capping. During the deposition of such a heterostructure, both ferroelectric layers would now be SHG active and emit interfering SHG waves[30]. Here, the opposite polarization in the two ferroelectric layers should result in destructive interference so that the ISHG yield should decrease gradually during the growth of the second layer. This would bring the ultimate proof of a heterostructure made up of two ferroelectric layers with opposing polarization directions and, hence, exhibiting the maximized interfacial charge doping.

To achieve this, we first have to identify ways to impose opposite charges at both interfaces so that they favor the same polarization direction. While the charges at the bottom interface can be selected with the layer polarization of the buffer (see section 2.1.2), the electrostatics of the top interface can be influenced by charged defects accumulating at the surface if the film is comprised of volatile elements[31] (see

section 6.1). In the case of BFO, the bismuth volatility generates a positively charged off-stoichiometric surface layer[137,174]. Hence, a negatively charged bottom interface would stabilize a robust and uniform downwards pointing polarization in the BFO film. To achieve this, the termination of the LSMO buffer layer has to change from MnO_2 to the La,SrO termination, giving rise to a net negative bound charge at the bottom interface (Fig. 8.8a). Insertion of an SrO-terminated $SrRuO_3$ (SRO) layer between the bottom LSMO and the substrate is instrumental in achieving this: it changes the BO_2 surface termination to the AO termination for all the layers in the heterostructure and, hence, gives rise to electron accumulation at the bottom interface of BFO.

Figure 8.8: Stabilization of uniform polarization in the capped ferroelectric layer. (a) The TT heterostructure achieved with BTO|BFO and the insertion of a 2-u.c.-thick SRO. (b) ISHG monitoring of the TT heterostructure growth. The horizontal axis shows the subsequent deposition of the layers comprising the heterostructure. The rate of the LSMO deposition is increased in order to minimize the time during which the bottom ferroelectric is exposed to a low charge-screening potential. The artificial TT-wall in the heterostructure is hole-doped (red shading). SHG waves (sketched in orange) emitted from the layers with opposite polarization have a 180° phase shift.

For the selected [BTO|LSMO|BFO] configuration with BFO as the bottom layer, the inserted 2-u.c.-thick SRO layer inverts the sequence of atomic planes in the entire heterostructure and consequently the direction of polarization in both BFO and BTO. As a result, the heterostructure now has the TT polarization configuration, shown in Figure 8.8a, for the sequence of ferroelectrics that without SRO was giving rise to the HH configuration (Fig. 8.1b). The ISHG tracking of the growth of this heterostructure is shown in Figure 8.8b. After the BFO deposition has been finished, we observe more than a two-fold increase in the ISHG signal, in line with the coordinated interface contributions that favor a uniform downwards oriented polarization. The momentary dip in the ISHG signal during the deposition of the first few unit cells of LSMO is due to their low charge-screening potential[244], but the signal not only recovers but is

augmented further when the metallicity of the junction is established. We note that a higher LSMO deposition rate is beneficial for preserving the single-domain state in the capped BFO layer, as it shortens the time during which it is exposed to the imperfect metal. During the deposition of the second ferroelectric BTO layer, we see a gradually decreasing ISHG signal. This signifies the destructive interference between the two layers and confirms that both oppositely-polarized ferroelectric layers remain in the single-domain state. This highlights the importance of coordinated interface electrostatics[31] in heterostructures comprising ultrathin ferroelectrics.
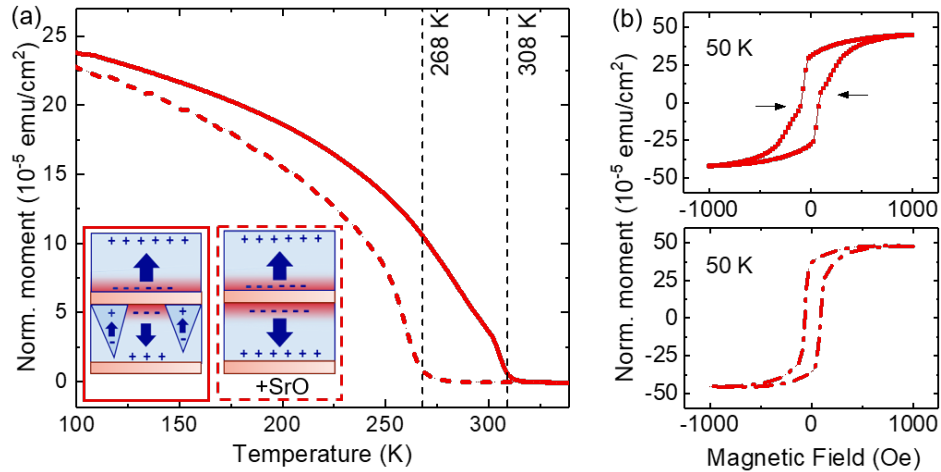
Figure 8.9: Maximized interfacial charge doping due to prevented domain formation in the lower ferroelectric layer. (a) Changes in magnetization with respect to the temperature measured for the TT heterostructures with different domain states in the buried layers, illustrated in the sketches. (b) Magnetic hysteresis curves of the two heterostructures recorded at 50 K. Solid and dashed lines correspond to the heterostructures with the lower ferroelectric layer in the multidomain or single-domain state, respectively. Arrows highlight changes in the magnetic response characteristic of two different ferromagnetic contributions. Artificial TT-walls in the heterostructures are hole-doped (red shading).

The circumvented domain breakup in the lower ferroelectric layer provides a much higher effective charge doping of the LSMO layers in the artificial TT heterostructure, which is reflected in the altered magnetic properties of the system. In Figure 8.9a we compare the magnetic response of the TT heterostructure with (dashed line, corresponding to Figure 8.8b) and without (solid line, corresponding to Figure 8.3b) the single-domain configuration stabilized in the capped layer. The TT heterostructure buffered with SRO shows only one phase transition associated with the buffer LSMO layer as observed for the heterostructure without the SRO buffer, which we rationalized by the antiferromagnetic order in the sandwiched layer. This demonstrates that the magnetic behavior of the TT wall is maintained despite the reversed atomic surface termination and the exchanged deposition sequence of the ferroelectric compounds in the multilayer. This clearly shows that the properties of our artificial magnetoelectric

domain walls are predominantly driven by the electrostatic doping at the interfaces with ferroelectric layers rather than other effects (e.g. interfacial chemistry). The most noticeable change is the lowered value of T_C of the buffer LSMO layer from 308 K to 268 K. This is in line with the stabilized net polarization of the buried layer, giving rise to a higher electron doping of the bottom LSMO layer. This, in turn, points to increased hole doping in the TT-like LSMO junction (the sandwiched LSMO layer). The boost in the electrostatic doping of the TT wall ensures that the domain-wall-like layer stays antiferromagnetically ordered down to very low temperatures. In line with this, we only measure the magnetic response of the buffer LSMO layer at 50 K characterized by a single hysteresis loop, see Figure 8.9b, bottom. A double hysteresis loop with two disparate coercive fields is recorded for the heterostructure with a multidomain bottom ferroelectric layer, see Figure 8.9b, top. This is in line with the coexistence of ferromagnetic order in both LSMO layers at that temperature, as the suppression of magnetization is not as strong due to the lower degree of hole doping in the sandwiched layer.

8.6 Discussion and outlook

In summary, we introduced the concept of artificial magnetoelectric domain walls where the constituents of a multilayer heterostructure serve as domain-wall-like elements that possess tunable magnetization and conductivity. We inserted ultrathin LSMO layers in between BFO and BTO ferroelectric thin films to create an interfacial magnetoelectric charge-based coupling between the polarization directions and the magnetization and conductivity in LSMO. The HH polarization configuration in the heterostructure leads to electron doping in the domain-wall-like LSMO layer, while the TT configuration triggers hole doping. The artificial HH domain wall is insulating and paramagnetic at room temperature, while upon cooling it gradually becomes conducting and ferromagnetic. The artificial TT wall has contrasting properties – at room temperature, it is paramagnetic metallic and undergoes a phase transition to the antiferromagnetic metallic phase at lowered temperatures. We confirmed that the properties of artificial domain walls are independent of the deposition sequence of the selected ferroelectrics BTO and BFO as long as the type of the interfacial charge doping (i.e. electron or hole) is preserved. We investigated how the polar state in the ferroelectric constituents emerges and evolves. After the deposition, we measured the optical conductivity and the magnetic properties of the LSMO layers in the heterostructures using only non-destructive probes. The complementary data sets enabled the unambiguous assignment of the changes in LSMO phases observed in response to different polar states of the adjacent ferroelectric layers. Our work, thus, provides new insights into the electrical control of magnetism in ultrathin multiferroic oxide heterostructures, especially with regard to

the non-invasive polar-state monitoring and manipulation on the atomic level.

Further studies are required to identify a path towards stable single-domain states in the HH heterostructure. While the stabilization of single-domain layers in the TT multilayer was attributed to the Bi volatility, there are no volatile elements in BTO, calling for an alternative approach to that of the coordinated interfacial electrostatics. Further studies could investigate whether switching polarization locally in the HH and TT heterostructures (e.g. with an SPM tip from HH to TH) could locally change the LSMO conduction. This could be of use for printing nanoscale circuitry. The design of superlattices made up of functional domain-wall-like elements could enable a multilevel logic architecture, where each artificial domain wall could be regarded as a separate functional element.

Lastly, some technical aspects should be addressed in order to make these heterostructures of use for device applications. The multilayers would have to undergo a complex patterning procedure in order to fabricate devices with electrodes that enable independent switching of both ferroelectric layers while still providing access to the functional strip of tunable conductivity and magnetization. Additionally, as the room-temperature performance is desired, the operating temperature of the artificial HH and TT domain-wall-like elements (< 300 K in the current state) should be elevated by increasing the LSMO thickness, optimizing its initial Sr-substitution level, or by modifying epitaxial strain.

CHAPTER

Conclusions and Outlook

This thesis presents a collection of results demonstrating how ferroelectric and ferro-magnetic order can be tuned by interface engineering in epitaxial heterostructures of complex oxides. We consider a wide array of interfacial effects, including structural defect formation, interfacial polarization continuity, changes in electrostatics, as well as interfacial symmetry breaking, and we show that they can all be instrumental in setting the properties of the ferroic layers both macroscopically (e.g. polar and magnetic anisotropy, domain configurations) and at the atomic length-scale (e.g. domain-wall chirality).

While interfaces between classical perovskites have already been widely investigated[7,79], we went one step further by epitaxially combining perovskites with layered Aurivillius phases[39,126] while preserving their respective out-of-plane and in-plane polar anisotropies. We showed that this unconventional epitaxy not only improves the existing properties of the out-of-plane-polarized perovskite ferroelectrics, such as critical thickness for ferroelectricity, their domain patterns, but also paves the way for new metal-free device paradigms as well as fundamental concepts, such as the electric equivalent of the DMI known for magnetically ordered systems. Reaching beyond ferroelectric interfaces, we demonstrated magnetoelectric phase control at the interfaces between ultrathin ferromagnetic and ferroelectrics layers, for which we harnessed our accumulated knowledge of ferroelectric domain states and interfacial polarization control.

We started by identifying the Aurivillius phase as a promising compound family for integration into perovskite-based heterostructures. In Chapter 4 we demonstrated that single-crystallinity in BFTO layers of the Aurivillius phase can be achieved by stabilizing a coalescent layer-by-layer growth mode. This growth mode differs from the standard layer-by-layer growth mode seen in perovskites: structural blocks of several nanometers in height corresponding to Aurivillius half-unit cells, rather than single
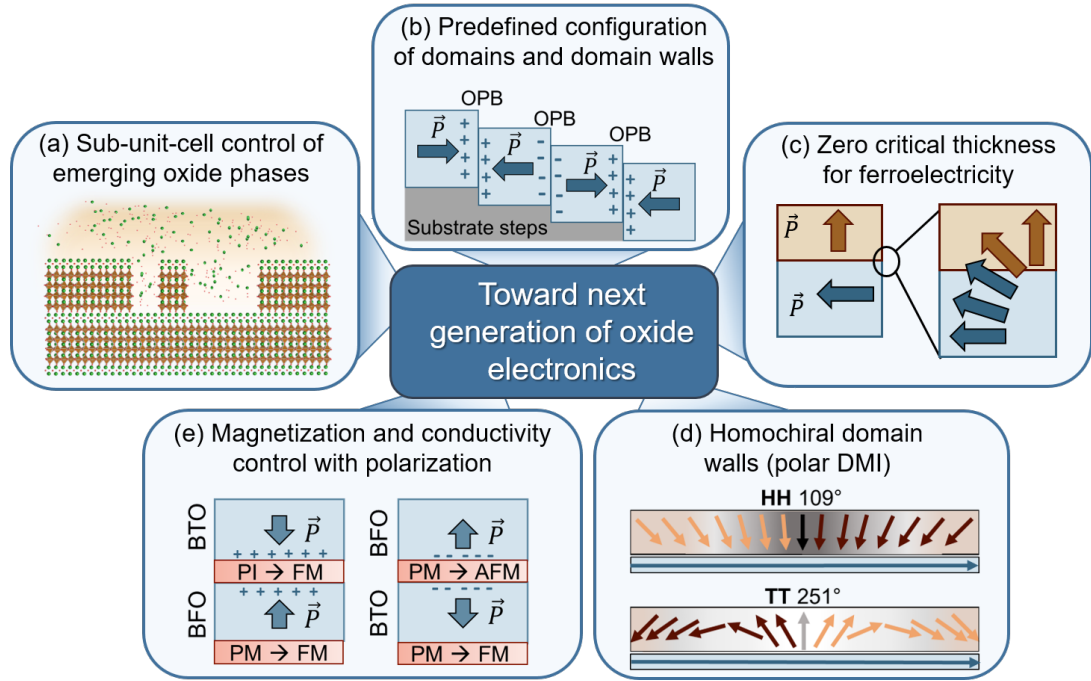
Figure 9.1: The results presented in this thesis hold promise to advance electronics based on complex ferroic oxides. (a-e) Schematic representations of principle achievements covered in Chapters 4 to 8.

perovskite unit cells, coalesce to form full atomically flat layers. Aside from ensuring the phase purity, such growth also enabled control over the thickness and the resulting domain configuration with sub-unit-cell precision (Fig. 9.1a). The achieved single-crystallinity in the BFTO films grants a uniaxial in-plane polarization, which we detected in films starting from a half-unit-cell thickness. Lastly, we demonstrated that the fatigue-free performance associated with the Aurivillius-phase ceramics[38] applies to our ultrathin epitaxial films, as they showed little change in their polar properties even after as many as 10^{10} switching cycles.

A closer look at the domain configuration in the ultrathin BFTO films revealed an unusual formation of charged domain walls, which we investigated in great detail in Chapter 5. We identified structural defects that form at every substrate step and act as nucleation centers for domain walls. This motivated us to propose new means of ferroelectric and ferromagnetic domain engineering, where the domain size and domain-wall position can be predefined by the substrate morphology (Fig. 9.1b).

The meticulous degree of control over both structural and ferroelectric properties of the Aurivillius films allowed us to proceed with their integration into perovskite-based epitaxial heterostructures. In Chapter 6, the in-plane-polarized BFTO buffer layers were shown to create an interfacial polarization continuity required for the out-of-plane BTO polarization to emerge from the very first unit cell (Fig. 9.1c). Charged domain walls in the BFTO buffer enabled electrode-free BTO polarization switching,

setting the stage for metal-free ferroelectric device paradigms.

While the BTO and BFTO layers in the heterostructure explored in Chapter 6 preserve their respective polar anisotropies, in Chapter 7 we include an additional polarization degree of freedom by considering the multiferroic BFO film with both in-plane- and out-of-plane polarization components in place of the out-of-plane-polarized BTO. The use of the in-plane-polarized Aurivillius layers was proven to be a powerful tool in setting the polar anisotropy and the domain configurations in the BFO film. Most importantly, we found that the interfacial symmetry-breaking provided by the ferroelectric buffer triggers the formation of homochiral BFO domain walls (Fig. 9.1d), exemplified by the observation of conceptually novel 251° domain walls. We believe that the net polar chirality in our films could be an experimental signature of the recently proposed electric counterpart to the well-known DMI in magnetically ordered materials.

Lastly, in Chapter 8 we made use of our understanding we had gathered throughout the preceding chapters of how polar states are controlled interfacially for exploiting the interfacial magnetoelectric coupling. We created artificial domain-wall-like elements by inserting ultrathin LSMO junctions in between two ferroelectric layers with opposite polarization directions. We showed that the magnetization and conductivity of the functional LSMO layer can be tuned with the polarization directions of the surrounding layers, as drastically different properties were achieved with the HH and TT polarization configurations (Fig. 9.1e).

Collectively, this thesis not only uncovers routes to enhance the existing ferroic-oxide-based electronics but also proposes new fundamental and device-related concepts. The results highlight the importance of interfacial contributions in epitaxial heterostructures that can exert extensive control over ferroic orders. Additionally, our work on the epitaxy between the perovskite and Aurivillius phases is likely to encourage new approaches to oxide electronics focused on such hybrid heterostructures. In the realm of fundamental understanding, our observed polar homochirality at BFO domain walls deserves particular attention. It would be interesting to conduct some further studies on the underlying mechanism behind the polar DM-like interaction in ferroelectrics induced by in-plane-polarized buffer layers. Given how indispensable the interfacial DMI in magnetically ordered systems has become, the advances introduced by its ferroelectric counterpart can be already foreseen, such as the provided novel route for creating polar topological objects.

Contributions to this thesis

The work presented in this thesis is a result of scientific collaborations. My own contributions and the contributions of our collaborators are outlined below. All work was performed at ETH Zurich unless stated otherwise. The work was initiated and supervised by Morgan Trassin jointly with Manfred Fiebig.

Chapter 4: All samples were grown using PLD by me and by Natascha Gray under my supervision. I performed the structural characterization of the samples using XRD and AFM. The STEM imaging was done by Marco Campanini and Marta D. Rossell at Empa. Top electrodes for electrical characterization were designed and deposited by Banani Biswas and Christof Schneider at Paul Scherrer Institute. I carried out the electrical characterization and the PFM measurements of the samples.

Chapter 5: The PLD growth of the samples was done by me. I performed the AFM- and PFM-based characterization of the samples. The DFT calculations were carried out by Quintin N. Meier at CEA Grenoble. I performed the magnetometry measurements, while the cryogenic MFM measurements of the samples were done by Lukas Kürten.

Chapter 6: The PLD growth, the ISHG characterization, and the structural characterization of the samples were all performed by me. I carried out the PFM analysis, while the AFM tomography measurements were done by Thomas Moran and Bryan D. Huey at the University of Connecticut.

Chapter 7: The PLD growth, the ISHG characterization, and the structural characterization of the samples were performed by me. The STEM studies were carried out at Empa by Marco Campanini and Marta D. Rossell. I performed the PFM analysis of the heterostructures together with Natascha Gray. The phase-field simulations were done by Quintin N. Meier at CEA Grenoble.

Chapter 8: I performed the PLD growth and the ISHG characterization of the samples. The structural and magnetic analysis of the heterostructures was done by me. Optical conductivity measurements were carried out by Chia-Jung Yang and Shovon Pal.

Publications and conference talks

Publications

Publications presented as part of this thesis:

1. N. Strkalj, <u>E. Gradauskaite</u>, J. Nordlander and M. Trassin. Design and Manipulation of Ferroic Domains in Complex Oxide Heterostructures. *Materials* **12**, 3108 (2019).

2. <u>E. Gradauskaite</u>, M. Campanini, B. Biswas, C. W. Schneider, M. Fiebig, M. D. Rossell, M. Trassin. Robust In-Plane Ferroelectricity in Ultrathin Epitaxial Aurivillius Films. *Advanced Materials Interfaces* **7**, 2000202 (2020).

3. <u>E. Gradauskaite</u>, P. Meisenheimer, M. Müller, J. Heron, M. Trassin. Multiferroic heterostructures for spintronics. *Physical Sciences Reviews* **6**, 20190072 (2021).

4. M. F. Sarott*, <u>E. Gradauskaite</u>*, J. Nordlander, N. Strkalj and M. Trassin. In situ monitoring of epitaxial ferroelectric thin-film growth. *Journal of Physics Condensed Matter* **33**, 293001 (2021). *-equal author contributions.

5. <u>E. Gradauskaite</u>, N. Gray, M. Campanini, M. D. Rossell, M. Trassin. Nanoscale Design of High-Quality Epitaxial Aurivillius Thin Films. *Chemistry of Materials* **33**, 9439-9446 (2021).

6. <u>E. Gradauskaite</u>, K. A. Hunnestad, Q. N. Meier, D. Meier, M. Trassin. Ferroelectric domain engineering using structural defect ordering, *Chemistry of Materials* **34**, 6468–6475 (2022).

7. <u>E. Gradauskaite</u>, Q. N. Meier, N. Gray, M. Campanini, T. Moran, B. D. Huey, M. D. Rossell, M. Fiebig, M. Trassin. Defeating depolarizing fields with artificial flux closure in ultrathin ferroelectrics, *submitted*.

8. <u>E. Gradauskaite</u>, C.-J. Yang, S. Pal, M. Fiebig, M. Trassin. Magnetoelectric phase control at domain-wall-like interfaces, *in preparation*.

9. <u>E. Gradauskaite</u>, M. Campanini, M. D. Rossell, M. Trassin. Design of domain walls and their chirality in $BiFeO_3$ through interfacial chemistry, *in preparation*.

Other publications:

10. <u>E. Gradauskaite</u>, J. Gardner, R. M. Smith, F. D. Morrison, S. L. Lee, R. S. Katiyar, J. F. Scott. Lead palladium titanate: A room-temperature multiferroic, *Physical Review B*, **96**, 104104 (2017). (Editor's Suggestion)

11. S. Vélez, J. Schaab, M. S. Wörnle, M. Müller, <u>E. Gradauskaite</u>, P. Welter, C. Gutgsell, C. Nistor, C. L. Degen, M. Trassin, M. Fiebig, P. Gambardella. High-speed domain wall racetracks in a magnetic insulator, *Nature Communications*, **10**, 4750 (2019).

12. D. K. Pradhan, A. K. Mishra, S. Kumari, A. Basu, M. Somayazulu, <u>E. Gradauskaite</u>, Re. M. Smith, J. Gardner, P. W. Turner, A. T. N'Diaye, M. B. Holcomb, R. S. Katiyar, P. Zhou, G. Srinivasan, J. M. Gregg, J. F. Scott. Studies of Multiferroic palladium perovskites, *Scientific Reports*, **10**, 9:1685 (2019).

13. M. Campanini, <u>E. Gradauskaite</u>, M. Trassin, D. Yi, P. Yu, R. Ramesh, R. Erni, M. D. Rossell. Imaging and quantification of charged domain walls in BiFeO$_3$, *Nanoscale*, **12**, 9186–9193 (2020).

14. S. Vélez, S. Ruiz-Gómez, J. Schaab, <u>E. Gradauskaite</u>, M. S. Wornle, P. Welter, B. J. Jacot, C. L. Degen, M. Trassin, M. Fiebig, P. Gambardella. Current-driven dynamics and ratchet effect of skyrmion bubbles in a ferrimagnetic insulator, Nature Nanotechnology, **17**, 834 (2022).

15. J. Nordlander, B. F. Grosso, M. D. Rossell, A. Maillard, <u>E. Gradauskaite</u>, N. A. Spaldin, M. Fiebig, M. Trassin. Electrostatic engineering of the BiFeO$_3$ phase diagram in ultrathin films at the morphotropic phase boundary, *in preparation.*

16. M. Giraldo, H. Sim, A. Simonov, M. Lilienblum, S. Lotfy, <u>E. Gradauskaite</u>, M. D. Rossell, M. Trassin, J.-G. Park, Th. Lottermoser, M. Fiebig. Tuning multiferroic properties in hexagonal YMnO$_3$ by manipulation of the structural order, *in preparation.*

17. I. Efe, <u>E. Gradauskaite</u>, M. Fiebig, M. Trassin. In-Situ Monitoring of Polarization Dynamics During Layered-Ferroelectrics Epitaxial Design, *in preparation.*

18. M. Müller, I. Efe, M. F. Sarott, <u>E. Gradauskaite</u>, M. Trassin. The Evolution of Ferroelectrics, *in preparation.*

Conference talks

1. German Physical Society (DPG) Spring meeting, Berlin, Germany (2018).
   "Pd doped $PbTiO_3$: A New Room Temperature Multiferroic".

2. German Physical Society (DPG) Spring meeting, Regensburg, Germany (2019).
   "Artificial Multiferroic Domain Walls in Oxide Heterostructures"

3. F2CP2 2019 Joint Conference ISAF-ICE-EMF-IWPM-PFM, Lausanne, Switzerland (2019).
   "Artificial Multiferroic Domain Walls in Oxide Heterostructures"

4. Electronic Materials and Applications, Orlando, USA (2020).
   "Robust In-Plane Ferroelectricity in Ultrathin Epitaxial Aurivillius Films"

5. Electronic Materials and Applications, virtual meeting (2021).
   "Integration of In-Plane Polarized Epitaxial Aurivillius Films into Perovskite Heterostructures"

6. German Physical Society (DPG) virtual meeting (2021).
   "Defeating Depolarizing Fields with Artificial Flux Closure in Ultrathin Ferroelectrics" (Selected contributed talk)

7. QUOROM - 5 virtual meeting (2021).
   "Defeating Depolarizing Fields with Artificial Flux Closure in Ultrathin Ferroelectrics" (Selected contributed talk)

8. 1st EPS Structural Dynamics Afternoon Online Workshop. Topic: Topological Features in Ferroic Systems (2022).
   "Stabilization of Polar Homochirality at $BiFeO_3$ Domain Walls" (Invited talk)

9. ISAF-PFM-ECAPD Joint Conference, Tours, France (2022).
   "Interfacial Stabilization of Homochiral Ferroelectric Domain Walls in $BiFeO_3$" (Invited Young Ferroelectric Investigator talk)

10. German Physical Society (DPG) meeting, Regensbrug, Germany (2022).
    "Interfacial Stabilization of Homochiral Ferroelectric Domain Walls in $BiFeO_3$"

Bibliography

[1] T. N. Theis and P. M. Solomon, "It 's Time to Reinvent the Transistor!," *Science*, no. March, pp. 1600–1601, 2010.

[2] S. Salahuddin and S. Datta, "Use of negative capacitance to provide voltage amplification for low power nanoscale devices," *Nano Letters*, vol. 8, no. 2, pp. 405–410, 2008.

[3] D. E. Nikonov and I. A. Young, "Benchmarking of Beyond-CMOS Exploratory Devices for Logic Integrated Circuits," *IEEE Journal on Exploratory Solid-State Computational Devices and Circuits*, vol. 1, pp. 3–11, dec 2015.

[4] M. Bibes, J. E. Villegas, and A. Barthélémy, "Ultrathin oxide films and interfaces for electronics and spintronics," *Advances in Physics*, vol. 60, pp. 5–84, feb 2011.

[5] M. Coll, J. Fontcuberta, M. Althammer, M. Bibes, H. Boschker, A. Calleja, G. Cheng, M. Cuoco, R. Dittmann, B. Dkhil, I. El Baggari, M. Fanciulli, I. Fina, E. Fortunato, C. Frontera, S. Fujita, V. Garcia, S. T. Goennenwein, C. G. Granqvist, J. Grollier, R. Gross, A. Hagfeldt, G. Herranz, K. Hono, E. Houwman, M. Huijben, A. Kalaboukhov, D. J. Keeble, G. Koster, L. F. Kourkoutis, J. Levy, M. Lira-Cantu, J. L. MacManus-Driscoll, J. Mannhart, R. Martins, S. Menzel, T. Mikolajick, M. Napari, M. D. Nguyen, G. Niklasson, C. Paillard, S. Panigrahi, G. Rijnders, F. Sánchez, P. Sanchis, S. Sanna, D. G. Schlom, U. Schroeder, K. M. Shen, A. Siemon, M. Spreitzer, H. Sukegawa, R. Tamayo, J. van den Brink, N. Pryds, and F. M. Granozio, "Towards Oxide Electronics: a Roadmap," *Applied Surface Science*, vol. 482, pp. 1–93, 2019.

[6] D. Elbio, "Complexity in Strongly Correlated Electronic Systems," *Science*, vol. 309, no. July, pp. 257–262, 2005.

[7] P. Zubko, S. Gariglio, M. Gabay, P. Ghosez, and J.-M. Triscone, "Interface Physics in Complex Oxide Heterostructures," *Annual Review of Condensed Matter Physics*, vol. 2, no. 1, pp. 141–165, 2011.

[8] C. A. Fernandes Vaz and U. Staub, "Artificial multiferroic heterostructures," *Journal of Materials Chemistry C*, vol. 1, no. 41, pp. 6731–6742, 2013.

[9] M. Trassin, "Low energy consumption spintronics using multiferroic heterostructures," *Journal of Physics Condensed Matter*, vol. 28, no. 3, p. 033001, 2016.

[10] D. A. Thompson and J. S. Best, "Future of magnetic data storage technology," *IBM Journal of Research and Development*, vol. 44, no. 3, pp. 311–322, 2000.

[11] J. F. Scott and C. A. Paz de Araujo, "Ferroelectric Memories," *Science*, vol. 246, no. 4936, pp. 1400–1405, 1989.

[12] J. F. Scott, *Ferroelectric Memories*. New York: Springer - Verlag Berlin Heidelberg, 2000.

[13] D. C. Ralph and M. D. Stiles, "Spin transfer torques," *Journal of Magnetism and Magnetic Materials*, vol. 320, no. 7, pp. 1190–1216, 2008.

[14] I. M. Miron, G. Gaudin, S. Auffret, B. Rodmacq, A. Schuhl, S. Pizzini, J. Vogel, and P. Gambardella, "Current-driven spin torque induced by the Rashba effect in a ferromagnetic metal layer," *Nature Materials*, vol. 9, no. 3, pp. 230–234, 2010.

[15] A. Fert and F. N. Van Dau, "Spintronics, from giant magnetoresistance to magnetic skyrmions and topological insulators," *Comptes Rendus Physique*, vol. 20, no. 7-8, pp. 817–831, 2019.

[16] F. Trier, P. Noël, J. V. Kim, J. P. Attané, L. Vila, and M. Bibes, "Oxide spin-orbitronics: spin–charge interconversion and topological spin textures," *Nature Reviews Materials*, vol. 7, no. 4, pp. 258–274, 2022.

[17] V. Garcia and M. Bibes, "Ferroelectric tunnel junctions for information storage and processing," *Nature Communications*, vol. 5, p. 4289, 2014.

[18] A. Chanthbouala, V. Garcia, R. O. Cherifi, K. Bouzehouane, S. Fusil, X. Moya, S. Xavier, H. Yamada, C. Deranlot, N. D. Mathur, M. Bibes, A. Barthélémy, and J. Grollier, "A ferroelectric memristor," *Nature Materials*, vol. 11, no. 10, pp. 860–864, 2012.

[19] S. Lequeux, J. Sampaio, V. Cros, K. Yakushiji, A. Fukushima, R. Matsumoto, H. Kubota, S. Yuasa, and J. Grollier, "A magnetic synapse: Multilevel spin-torque memristor with perpendicular anisotropy," *Scientific Reports*, vol. 6, p. 31510, 2016.

[20] S. Manipatruni, D. E. Nikonov, and I. A. Young, "Beyond CMOS computing with spin and polarization," *Nature Physics*, vol. 14, no. 4, pp. 338–343, 2018.

[21] S. Manipatruni, D. E. Nikonov, C.-C. Lin, T. A. Gosavi, H. Liu, B. Prasad, Y.-L. Huang, E. Bonturim, R. Ramesh, and I. A. Young, "Scalable energy-efficient magnetoelectric spin–orbit logic," *Nature*, vol. 565, pp. 35–42, 2019.

[22] N. Strkalj, E. Gradauskaite, J. Nordlander, and M. Trassin, "Design and manipulation of ferroic domains in complex oxide heterostructures," *Materials*, vol. 12, no. 3108, p. 3108, 2019.

[23] E. Gradauskaite, P. Meisenheimer, M. Müller, J. Heron, and M. Trassin, "Multiferroic heterostructures for spintronics," *Physical Sciences Reviews*, vol. 6, no. 2, p. 20190072, 2021.

[24] C. Kittel, *Introduction to Solid State Physics*. John Wiley and Sonds, Inc, 8th ed. ed., 2005.

[25] S. Blundell, *Magnetism in Condensed Matter*. New York: Oxford University Press, 2001.

[26] A. K. Tagantsev, L. Eric Cross, and J. Fousek, "Domains in Ferroic Crystals and Thin Films," 2010.

[27] K. M. Rabe, C. H. Ahn, and J.-M. Triscone, *Physics of Ferroelectrics. A Modern Perspective*. Berlin: Springer - Verlag Berlin Heidelberg, 2007.

[28] N. A. Spaldin, I. Efe, M. D. Rossell, and C. Gattinoni, "Layer and spontaneous polarizations in perovskite oxides and their interplay in multiferroic bismuth ferrite," *The Journal of Chemical Physics*, vol. 154, p. 154702, 2021.

[29] P. Yu, W. Luo, D. Yi, J. X. Zhang, M. D. Rossell, C.-H. Yang, L. You, G. Singh-Bhalla, S. Y. Yang, Q. He, Q. M. Ramasse, R. Erni, L. W. Martin, Y. H. Chu, S. T. Pantelides, S. J. Pennycook, and R. Ramesh, "Interface control of bulk ferroelectric polarization," *Proceedings of the National Academy of Sciences*, vol. 109, no. 25, pp. 9710–9715, 2012.

[30] G. De Luca, N. Strkalj, S. Manz, C. Bouillet, M. Fiebig, and M. Trassin, "Nanoscale design of polarization in ultrathin ferroelectric heterostructures," *Nature Communications*, vol. 8, no. 1, p. 1419, 2017.

[31] N. Strkalj, C. Gattinoni, A. Vogel, M. Campanini, R. Haerdi, A. Rossi, M. D. Rossell, N. A. Spaldin, M. Fiebig, and M. Trassin, "In-situ monitoring of interface proximity effects in ultrathin ferroelectrics," *Nature Communications*, vol. 11, p. 5815, 2020.

[32] V. Leca, D. H. A. Blank, and G. Rijnders, "Termination control of $NdGaO_3$ crystal surfaces by selective chemical etching," *arXiv*, 2012.

[33] X. Hong, A. Posadas, and C. H. Ahn, "Examining the screening limit of field effect devices via the metal-insulator transition," *Applied Physics Letters*, vol. 86, no. 14, p. 142501, 2005.

[34] W. L. Warren, B. A. Tuttle, and D. Dimos, "Ferroelectric fatigue in perovskite oxides," *Applied Physics Letters*, vol. 67, no. November 2018, p. 1426, 1995.

[35] J. F. Scott and M. Dawber, "Oxygen-vacancy ordering as a fatigue mechanism in perovskite ferroelectrics," *Applied Physics Letters*, vol. 76, no. 25, p. 3801, 2000.

[36] C. Brennan, "Model of ferroelectric fatigue due to defect/domain interactions," *Ferroelectrics*, vol. 150, no. 1, pp. 199–208, 1993.

[37] M. Dawber and J. F. Scott, "A model for fatigue in ferroelectric perovskite thin films," *Applied Physics Letters*, vol. 76, no. 8, pp. 1060–1062, 2000.

[38] C. A-Paz de Araujo, J. D. Cuchiaro, L. D. McMillian, M. C. Scott, and J. F. Scott, "Fatigue-free ferroelectric capacitors with platinum electrodes," *Nature*, vol. 374, pp. 627–629, 1995.

[39] B. Aurivillius, "Mixed Bismuth Oxides with Layer Lattices. 1. The Structure Type of $CaNb_2Bi_2O_9$," *Arkiv. Kemi.*, vol. 1, pp. 463–480, 1949.

[40] E. Almahmoud, I. Kornev, and L. Bellaiche, "Dependence of Curie temperature on the thickness of an ultrathin ferroelectric film," *Physical Review B - Condensed Matter and Materials Physics*, vol. 81, no. 6, pp. 1–5, 2010.

[41] J. Junquera and P. Ghosez, "Critical thickness for ferroelectricity in perovskite ultrathin films," *Nature*, vol. 422, no. 6931, pp. 506–509, 2003.

[42] J. J. Steffes, R. A. Ristau, R. Ramesh, and B. D. Huey, "Thickness scaling of ferroelectricity in $BiFeO_3$ by tomographic atomic force microscopy," *Proceedings of the National Academy of Sciences of the United States of America*, vol. 116, no. 7, pp. 2413–2418, 2019.

[43] E. Dagotto, T. Hotta, and A. Moreo, "Colossal magnetoresistant materials: the key role of phase separation," *Physics Reports*, vol. 344, pp. 1–153, apr 2001.

[44] C. N. Rao, A. Arulraj, P. N. Santosh, and A. K. Cheetham, "Charge-Ordering in Manganates," *Chemistry of Materials*, vol. 10, no. 10, pp. 2714–2722, 1998.

[45] I. B. Bersuker, "Pseudo-Jahn-teller effect - A two-state paradigm in formation, deformation, and transformation of molecular systems and solids," *Chemical Reviews*, vol. 113, no. 3, pp. 1351–1390, 2013.

[46] G. F. Nataf, M. Guennou, J. M. Gregg, D. Meier, J. Hlinka, E. K. Salje, and J. Kreisel, "Domain-wall engineering and topological defects in ferroelectric and ferroelastic materials," *Nature Reviews Physics*, vol. 2, no. 11, pp. 634–648, 2020.

[47] S. Emori, U. Bauer, S. M. Ahn, E. Martinez, and G. S. Beach, "Current-driven dynamics of chiral ferromagnetic domain walls," *Nature Materials*, vol. 12, no. 7, pp. 611–616, 2013.

[48] S. S. P. Parkin, M. Hayashi, and L. Thomas, "Magnetic Domain-Wall Racetrack Memory," *Science*, vol. 320, pp. 190–194, 2008.

[49] D. Meier, "Functional domain walls in multiferroics," *Journal of Physics Condensed Matter*, vol. 27, no. 46, p. 463003, 2015.

[50] J. Seidel, L. W. Martin, Q. He, Q. Zhan, Y. H. Chu, A. Rother, M. E. Hawkridge, P. Maksymovych, P. Yu, M. Gajek, N. Balke, S. V. Kalinin, S. Gemming, F. Wang, G. Catalan, J. F. Scott, N. A. Spaldin, J. Orenstein, and R. Ramesh, "Conduction at domain walls in oxide multiferroics," *Nature Materials*, vol. 8, no. 3, pp. 229–234, 2009.

[51] G. Catalan, J. Seidel, R. Ramesh, and J. F. Scott, "Domain wall nanoelectronics," *Reviews of Modern Physics*, vol. 84, no. 1, pp. 119–156, 2012.

[52] D. Meier and S. M. Selbach, "Ferroelectric domain walls for nanotechnology," *Nature Reviews Materials*, vol. 7, no. 3, pp. 157–173, 2022.

[53] M. Campanini, E. Gradauskaite, M. Trassin, D. Yi, P. Yu, R. Ramesh, R. Erni, and M. D. Rossell, "Imaging and quantification of charged domain walls in $BiFeO_3$," *Nanoscale*, vol. 12, pp. 9186–9193, 2020.

[54] G. Catalan and J. F. Scott, "Physics and Applications of Bismuth Ferrite," *Advanced Materials*, vol. 21, pp. 2463–2485, 2009.

[55] R. E. Newnham, R. W. Wolfe, and J. F. Dorrian, "Structural basis of ferroelectricity in the bismuth titanate family," *Materials Research Bulletin*, vol. 6, no. 10, pp. 1029–1039, 1971.

[56] Y. Ding, J. S. Liu, H. X. Qin, J. S. Zhu, and Y. N. Wang, "Why lanthanum-substituted bismuth titanate becomes fatigue free in a ferroelectric capacitor with platinum electrodes," *Applied Physics Letters*, vol. 78, no. 26, pp. 4175–4177, 2001.

[57] M. A. Zurbuchen, W. Tian, X. Q. Pan, D. Fong, S. K. Streiffer, M. E. Hawley, J. Lettieri, Y. Jia, G. Asayama, S. J. Fulk, D. J. Comstock, S. Knapp, A. H. Carim, and D. G. Schlom, "Morphology, structure, and nucleation of out-of-phase boundaries (OPBs) in epitaxial films of layered oxides," *Journal of Materials Research*, vol. 22, no. 6, pp. 1439–1471, 2007.

[58] H. Funakubo, "Degradation-free dielectric property using bismuth layer-structured dielectrics having natural superlattice structure," *Journal of the Ceramic Society of Japan*, vol. 116, no. 1360, pp. 1249–1254, 2008.

[59] N. A. McDowell, K. S. Knight, and P. Lightfoot, "Unusual high-temperature structural behaviour in ferroelectric Bi_2WO_6," *Chem. Eur. J.*, vol. 12, pp. 1493–1499, 2006.

[60] A. Faraz, N. Deepak, M. Schmidt, M. E. Pemble, and L. Keeney, "A study of the temperature dependence of the local ferroelectric properties of c - axis oriented $Bi_6Ti_3Fe_2O_{18}$ Aurivillius phase thin films : Illustrating the potential of a novel lead-free pe," *AIP Advances*, vol. 5, no. 8, p. 087123, 2015.

[61] M. Krzhizhanovskaya, S. Filatov, V. Gusarov, P. Paufler, R. Bubnova, M. Morozov, and D. C. Meyer, "Aurivillius phases in the $Bi_4Ti_3O_{12}$/$BiFeO_3$ system: Thermal behaviour and crystal structure," *Zeitschrift fur Anorganische und Allgemeine Chemie*, vol. 631, no. 9, pp. 1603–1608, 2005.

[62] N. A. Lomanova, M. I. Morozov, V. L. Ugolkov, and V. V. Gusarov, "Properties of Aurivillius phases in the $Bi_4Ti_3O_{12}$-$BiFeO_3$ system," *Inorganic Materials*, vol. 42, no. 2, pp. 189–195, 2006.

[63] D. Song, J. Yang, B. Yang, L. Chen, F. Wang, and X. Zhu, "Evolution of structure and ferroelectricity in Aurivillius $Bi_4Bi_{n-3}Fe_{n-3}Ti_3O_{3n+3}$ thin films," *Journal of Materials Chemistry C*, vol. 6, no. 32, p. 8618, 2018.

[64] S. Sun and X. Yin, "Progress and perspectives on aurivillius[U+2010]type layered ferroe-lectric oxides in binary $Bi_4Ti_3O_{12}$-$BiFeO_3$ system for multifunc-tional applications," *Crystals*, vol. 11, no. 1, pp. 1–35, 2021.

[65] L. Keeney, T. Maity, M. Schmidt, A. Amann, N. Deepak, N. Petkov, S. Roy, M. E. Pemble, and R. W. Whatmore, "Magnetic Field-Induced Ferroelectric Switching in Multiferroic Aurivillius Phase Thin Films at Room Temperature," *Journal of the American Ceramic Society*, vol. 96, no. 8, pp. 2339–2357, 2013.

[66] A. Y. Birenbaum and C. Ederer, "Potentially multiferroic Aurivillius phase $Bi_5FeTi_3O_{15}$: Cation site preference, electric polarization, and magnetic coupling from first principles," *Physical Review B*, vol. 90, no. 21, p. 214109, 2014.

[67] N. Strkalj, G. De Luca, M. Campanini, S. Pal, J. Schaab, C. Gattinoni, N. A. Spaldin, M. D. Rossell, M. Fiebig, and M. Trassin, "Depolarizing-Field Effects in Epitaxial Capacitor Heterostructures," *Physical Review Letters*, vol. 123, no. 14, p. 147601, 2019.

[68] J. Wang, J. B. Neaton, H. Zheng, V. Nagarajan, S. B. Ogale, B. Liu, D. Viehland, V. Vaithyanathan, D. G. Schlom, U. V. Waghmare, N. A. Spaldin, K. M. Rabe, M. Wuttig, and R. Ramesh, "Epitaxial BiFeO$_3$ multiferroic thin film heterostructures," *Science*, vol. 299, no. 5613, pp. 1719–1722, 2003.

[69] J. X. Zhang, Q. He, M. Trassin, W. Luo, D. Yi, M. D. Rossell, P. Yu, L. You, C. H. Wang, C. Y. Kuo, J. T. Heron, Z. Hu, R. J. Zeches, H. J. Lin, A. Tanaka, C. T. Chen, L. H. Tjeng, Y. H. Chu, and R. Ramesh, "Microscopic origin of the giant ferroelectric polarization in tetragonal-like BiFeO$_3$," *Physical Review Letters*, vol. 107, no. 14, pp. 1–5, 2011.

[70] S. R. Burns, O. Paull, J. Juraszek, V. Nagarajan, and D. Sando, "The Experimentalist's Guide to the Cycloid, or Noncollinear Antiferromagnetism in Epitaxial BiFeO$_3$," *Advanced Materials*, vol. 2003711, pp. 1–51, 2020.

[71] T. Zhao, A. Scholl, F. Zavaliche, K. Lee, M. Barry, A. Doran, M. P. Cruz, Y. H. Chu, C. Ederer, N. A. Spaldin, R. R. Das, D. M. Kim, S. H. Baek, C. B. Eom, and R. Ramesh, "Electrical control of antiferromagnetic domains in multiferroic BiFeO$_3$ films at room temperature," *Nature Materials*, vol. 5, no. 10, pp. 823–829, 2006.

[72] Y.-H. Chu, L. W. Martin, M. B. Holcomb, M. Gajek, S.-J. Han, Q. He, N. Balke, C.-H. Yang, D. Lee, W. Hu, Q. Zhan, P.-L. Yang, A. Fraile-Rodríguez, A. Scholl, S. X. Wang, and R. Ramesh, "Electric-field control of local ferromagnetism using a magnetoelectric multiferroic.," *Nature Materialsaterials*, vol. 7, no. 6, pp. 478–82, 2008.

[73] J. T. Heron, M. Trassin, K. Ashraf, M. Gajek, Q. He, S. Y. Yang, D. E. Nikonov, Y. H. Chu, S. Salahuddin, and R. Ramesh, "Electric-field-induced magnetization reversal in a ferromagnet-multiferroic heterostructure," *Physical Review Letters*, vol. 107, no. 21, pp. 1–5, 2011.

[74] D. Sando, F. Appert, B. Xu, O. Paull, S. R. Burns, C. Carrétéro, B. Dupé, V. Garcia, Y. Gallais, A. Sacuto, M. Cazayous, B. Dkhil, J. M. Le Breton, A. Barthélémy, M. Bibes, L. Bellaiche, V. Nagarajan, and J. Juraszek, "A magnetic phase diagram for nanoscale epitaxial BiFeO$_3$ films," *Applied Physics Reviews*, vol. 6, no. 4, p. 041404, 2019.

[75] F. Bai, J. Wang, M. Wuttig, J. F. Li, N. Wang, A. P. Pyatakov, A. K. Zvezdin, L. E. Cross, and D. Viehland, "Destruction of spin cycloid in (111)$_c$ -oriented BiFeO$_3$ thin films by epitiaxial constraint: Enhanced polarization and release of latent magnetization," *Applied Physics Letters*, vol. 86, no. 3, pp. 1–3, 2005.

[76] S. K. Streiffer, C. B. Parker, A. E. Romanov, M. J. Lefevre, L. Zhao, J. S. Speck, W. Pompe, C. M. Foster, and G. R. Bai, "Domain patterns in epitaxial rhombohedral ferroelectric films. I. Geometry and experiments," *Journal of Applied Physics*, vol. 83, no. 5, pp. 2742–2753, 1998.

[77] A. P. Ramirez, "Colossal magnetoresistance," *Journal of Physics Condensed Matter*, vol. 9, no. 39, pp. 8171–8199, 1997.

[78] E. Dagotto, T. Hotta, and A. Moreo, "Colossal magnetoresistant materials: The key role of phase separation," *Physics Report*, vol. 344, no. 1-3, pp. 1–153, 2001.

[79] H. Y. Hwang, Y. Iwasa, M. Kawasaki, B. Keimer, N. Nagaosa, and Y. Tokura, "Emergent phenomena at oxide interfaces," *Nature Materials*, vol. 11, no. 2, pp. 103–113, 2012.

[80] D. G. Schlom, L. Q. Chen, C. B. Eom, K. M. Rabe, S. K. Streiffer, and J. M. Triscone, "Strain tuning of ferroelectric thin films," *Annual Review of Materials Research*, vol. 37, pp. 589–626, 2007.

[81] A. R. Damodaran, E. Breckenfeld, Z. Chen, S. Lee, and L. W. Martin, "Enhancement of Ferroelectric Curie Temperature in $BaTiO_3$ Films via Strain-Induced Defect Dipole Alignment," *Advanced Materials*, vol. 26, pp. 6341–6347, 2014.

[82] J. H. Haeni, P. Irvin, W. Chang, R. Uecker, P. Reiche, Y. L. Li, S. Choudhury, W. Tian, M. E. Hawley, B. Craigo, A. K. Tagantsev, X. Q. Pan, S. K. Streiffer, L. Q. Chen, S. W. Kirchoefer, J. Levy, and D. G. Schlom, "Room-temperature ferroelectricity in strained $SrTiO_3$," *Nature*, vol. 430, no. 7001, pp. 758–761, 2004.

[83] J. Lee, N. Sai, T. Cai, Q. Niu, and A. A. Demkov, "Interfacial magnetoelectric coupling in tricomponent superlattices," *Physical Review B - Condensed Matter and Materials Physics*, vol. 81, no. 14, pp. 1–5, 2010.

[84] C. Becher, L. Maurel, U. Aschauer, M. Lilienblum, C. Magén, D. Meier, E. Langenberg, M. Trassin, J. Blasco, I. P. Krug, P. A. Algarabel, N. A. Spaldin, J. A. Pardo, and M. Fiebig, "Strain-induced coupling of electrical polarization and structural defects in $SrMnO_3$ films," *Nature Nanotechnology*, vol. 10, no. 8, pp. 661–665, 2015.

[85] Y. H. Chu, Q. He, C. H. Yang, P. Yu, L. W. Martin, P. Shafer, and R. Ramesh, "Nanoscale control of domain architectures in $BiFeO_3$ thin films," *Nano Letters*, vol. 9, no. 4, pp. 1726–1730, 2009.

[86] M. Kubota, A. Tsukazaki, F. Kagawa, K. Shibuya, Y. Tokunaga, M. Kawasaki, and Y. Tokura, "Stress-induced perpendicular magnetization in epitaxial iron garnet thin films," *Applied Physics Express*, vol. 5, no. 10, pp. 14–17, 2012.

[87] M. Kubota, K. Shibuya, Y. Tokunaga, F. Kagawa, A. Tsukazaki, Y. Tokura, and M. Kawasaki, "Systematic control of stress-induced anisotropy in pseudomorphic iron garnet thin films," *Journal of Magnetism and Magnetic Materials*, vol. 339, pp. 63–70, 2013.

[88] H. Boschker, M. Mathews, E. P. Houwman, H. Nishikawa, A. Vailionis, G. Koster, G. Rijnders, and D. H. Blank, "Strong uniaxial in-plane magnetic anisotropy of (001)- and (011)-oriented $La_{0.67}Sr_{0.33}MnO_3$ thin films on $NdGaO_3$ substrates," *Physical Review B - Condensed Matter and Materials Physics*, vol. 79, p. 214425, 2009.

[89] Y. H. Chu, T. Zhao, M. P. Cruz, Q. Zhan, P. L. Yang, L. W. Martin, M. Huijben, C. H. Yang, F. Zavaliche, H. Zheng, and R. Ramesh, "Ferroelectric size effects in multiferroic $BiFeO_3$ thin films," *Applied Physics Letters*, vol. 90, no. 25, p. 252906, 2007.

[90] D. Sando, M. J. Han, V. Govinden, O. Paull, F. Appert, C. Carrétéro, J. Fischer, A. Barthélémy, M. Bibes, V. Garcia, S. Fusil, B. Dkhil, J. Juraszek, Y. Zhu, X. L. Ma, and V. Nagarajan, "Interfacial Strain Gradients Control Nanoscale Domain Morphology in Epitaxial $BiFeO_3$ Multiferroic Films," *Adv. Func. Mat.*, p. 2000343, 2020.

[91] N. Waterfield Price, A. M. Vibhakar, R. D. Johnson, J. Schad, W. Saenrang, A. Bombardi, F. P. Chmiel, C. B. Eom, and P. G. Radaelli, "Strain Engineering a Multiferroic Monodomain in Thin-Film $BiFeO_3$," *Physical Review Applied*, vol. 11, no. 2, p. 024035, 2019.

[92] A. Agbelele, D. Sando, C. Toulouse, C. Paillard, R. D. Johnson, R. Rüffer, A. F. Popkov, C. Carrétéro, P. Rovillain, J. M. Le Breton, B. Dkhil, M. Cazayous, Y. Gallais, M. A. Méasson, A. Sacuto, P. Manuel, A. K. Zvezdin, A. Barthélémy, J. Juraszek, and M. Bibes, "Strain and Magnetic Field Induced Spin-Structure Transitions in Multiferroic $BiFeO_3$," *Advanced Materials*, vol. 29, no. 9, p. 1602327, 2017.

[93] N. A. Hill, "Why Are There so Few Magnetic Ferroelectrics ?," *J. Phys. Chem. B*, vol. 104, p. 6694, 2000.

[94] H. J. A. Molegraaf, J. Hoffman, C. A. F. Vaz, S. Gariglio, D. van der Marel, C. H. Ahn, and J.-M. Triscone, "Magnetoelectric Effects in Complex Oxides with Competing Ground States," *Advanced Materials*, vol. 21, no. 34, pp. 3470–3474, 2009.

[95] C. A. Vaz, J. Hoffman, Y. Segal, J. W. Reiner, R. D. Grober, Z. Zhang, C. H. Ahn, and F. J. Walker, "Origin of the magnetoelectric coupling effect

in $Pb(Zr_{0.2}Ti_{0.8})O_3/La_{0.8}Sr_{0.2}MnO_3$ multiferroic heterostructures," *Physical Review Letters*, vol. 104, no. 12, p. 127202, 2010.

[96] C. A. F. Vaz, J. Hoffman, Y. Segal, M. S. J. Marshall, J. W. Reiner, Z. Zhang, R. D. Grober, F. J. Walker, and C. H. Ahn, "Control of magnetism in $Pb(Zr_{0.2}Ti_{0.8})O_3/La_{0.8}Sr_{0.2}MnO_3$ multiferroic heterostructures," *Journal of Applied Physics*, vol. 109, no. 7, p. 07D905, 2011.

[97] C. A. Vaz, F. J. Walker, C. H. Ahn, and S. Ismail-Beigi, "Intrinsic interfacial phenomena in manganite heterostructures," *Journal of Physics Condensed Matter*, vol. 27, p. 123001, 2015.

[98] M. F. Sarott, E. Gradauskaite, J. Nordlander, N. Strkalj, and M. Trassin, "In situ monitoring of epitaxial ferroelectric thin-film growth," *Journal of Physics Condensed Matter*, vol. 33, no. 29, p. 293001, 2021.

[99] J. Nordlander, G. De Luca, N. Strkalj, M. Fiebig, and M. Trassin, "Probing ferroic states in oxide thin films using optical second harmonic generation," *Applied Sciences*, vol. 8, no. 4, p. 570, 2018.

[100] C. Becher, M. Trassin, M. Lilienblum, C. T. Nelson, S. J. Suresha, D. Yi, P. Yu, R. Ramesh, M. Fiebig, and D. Meier, "Functional ferroic heterostructures with tunable integral symmetry," *Nature Communications*, vol. 5, p. 4295, 2014.

[101] A. Gruverman, M. Alexe, and D. Meier, "Piezoresponse force microscopy and nanoferroic phenomena," *Nature Communications*, vol. 10, no. 1, p. 1661, 2019.

[102] J. Guyonnet, H. Béa, F. Guy, S. Gariglio, S. Fusil, K. Bouzehouane, J. M. Triscone, and P. Paruch, "Shear effects in lateral piezoresponse force microscopy at 180° ferroelectric domain walls," *Applied Physics Letters*, vol. 95, p. 132902, 2009.

[103] E. B. Lochocki, S. Park, N. Lee, S. W. Cheong, and W. Wu, "Piezoresponse force microscopy of domains and walls in multiferroic $HoMnO_3$," *Applied Physics Letters*, vol. 99, p. 232901, 2011.

[104] R. K. Vasudevan, Y. Matsumoto, X. Cheng, A. Imai, S. Maruyama, H. L. Xin, M. B. Okatan, S. Jesse, S. V. Kalinin, and V. Nagarajan, "Deterministic arbitrary switching of polarization in a ferroelectric thin film," *Nature Communications*, vol. 5, p. 4971, 2014.

[105] A. Crassous, T. Sluka, A. K. Tagantsev, and N. Setter, "Polarization charge as a reconfigurable quasi-dopant in ferroelectric thin films," *Nature Nanotechnology*, vol. 10, no. 7, pp. 614–618, 2015.

[106] J. F. Scott, "Ferroelectrics go bananas," *Journal of Physics Condensed Matter*, vol. 20, no. 2, pp. 15–17, 2008.

[107] E. Gradauskaite, J. Gardner, R. M. Smith, F. D. Morrison, S. L. Lee, R. S. Katiyar, and J. F. Scott, "Lead palladium titanate: A room-temperature multiferroic," *Physical Review B*, vol. 96, no. 10, p. 104104, 2017.

[108] Y. Noguchi, T. Matsumoto, and M. Miyayama, "Impact of defect control on the polarization properties in $Bi_4Ti_3O_{12}$ ferroelectric single crystals," *Japanese Journal of Applied Physics*, vol. 44, p. L570, 2005.

[109] M. Campanini, M. Trassin, C. Ederer, R. Erni, and M. D. Rossell, "Buried In-Plane Ferroelectric Domains in Fe-Doped Single-Crystalline Aurivillius Thin Films," *ACS Applied Electronic Materials*, vol. 1, pp. 1019–1028, 2019.

[110] J. Song, Y. Zhou, and B. D. Huey, "3D structure-property correlations of electronic and energy materials by tomographic atomic force microscopy," *Applied Physics Letters*, vol. 118, no. 8, p. 080501, 2021.

[111] J. Song, Y. Zhou, N. P. Padture, and B. D. Huey, "Anomalous 3D nanoscale photoconduction in hybrid perovskite semiconductors revealed by tomographic atomic force microscopy," *Nature Communications*, vol. 11, no. 1, p. 3308, 2020.

[112] H. J. Joyce, J. L. Boland, C. L. Davies, S. A. Baig, and M. B. Johnston, "A review of the electrical properties of semiconductor nanowires: Insights gained from terahertz conductivity spectroscopy," *Semiconductor Science and Technology*, vol. 31, no. 10, p. 103003, 2016.

[113] D. M. A. Mackenzie, P. R. Whelan, P. Bøggild, P. U. Jepsen, A. Redo-Sanchez, D. Etayo, N. Fabricius, and D. H. Petersen, "Quality assessment of terahertz time-domain spectroscopy transmission and reflection modes for graphene conductivity mapping," *Optics Express*, vol. 26, no. 7, p. 9220, 2018.

[114] A. M. Ulatowski, L. M. Herz, and M. B. Johnston, "Terahertz Conductivity Analysis for Highly Doped Thin-Film Semiconductors," *Journal of Infrared, Millimeter, and Terahertz Waves*, vol. 41, no. 12, pp. 1431–1449, 2020.

[115] M. Giraldo, Q. N. Meier, A. Bortis, D. Nowak, N. A. Spaldin, M. Fiebig, M. C. Weber, and T. Lottermoser, "Magnetoelectric coupling of domains, domain walls and vortices in a multiferroic with independent magnetic and electric order," *Nature Communications*, vol. 12, no. 1, p. 3093, 2021.

[116] J. A. Mundy, B. F. Grosso, C. A. Heikes, D. F. Segedin, Z. Wang, Y. T. Shao, C. Dai, B. H. Goodge, Q. N. Meier, C. T. Nelson, B. Prasad, F. Xue, S. Ganschow, D. A. Muller, L. F. Kourkoutis, L. Q. Chen, W. D. Ratcliff, N. A. Spaldin,

R. Ramesh, and D. G. Schlom, "Liberating a hidden antiferroelectric phase with interfacial electrostatic engineering," *Science Advances*, vol. 8, no. 5, p. eabg5860, 2022.

[117] F. Xue, J. J. Wang, G. Sheng, E. Huang, Y. Cao, H. H. Huang, P. Munroe, R. Mahjoub, Y. L. Li, V. Nagarajan, and L. Q. Chen, "Phase field simulations of ferroelectrics domain structures in $PbZr_xTi_{1-x}O_3$ bilayers," *Acta Materialia*, vol. 61, no. 8, pp. 2909–2918, 2013.

[118] E. Gradauskaite, M. Campanini, B. Biswas, C. W. Schneider, M. Fiebig, M. D. Rossell, and M. Trassin, "Robust In-Plane Ferroelectricity in Ultrathin Epitaxial Aurivillius Films," *Advanced Materials Interfaces*, vol. 7, no. 14, p. 2000202, 2020.

[119] E. Gradauskaite, N. Gray, M. Campanini, M. D. Rossell, and M. Trassin, "Nanoscale Design of High-Quality Epitaxial Aurivillius Thin Films," *Chemistry of Materials*, vol. 33, no. 23, pp. 9439–9446, 2021.

[120] M. Li, H. Tan, and W. Duan, "Hexagonal rare-earth manganites and ferrites: A review of improper ferroelectricity, magnetoelectric coupling, and unusual domain walls," *Physical Chemistry Chemical Physics*, vol. 22, no. 26, pp. 14415–14432, 2020.

[121] E. Bousquet, M. Dawber, N. Stucki, C. Lichtensteiger, P. Hermet, S. Gariglio, J. M. Triscone, and P. Ghosez, "Improper ferroelectricity in perovskite oxide artificial superlattices," *Nature*, vol. 452, no. 7188, pp. 732–736, 2008.

[122] M. H. Park, Y. H. Lee, T. Mikolajick, U. Schroeder, and C. S. Hwang, "Review and perspective on ferroelectric HfO_2-based thin films for memory applications," *MRS Communications*, vol. 8, no. 3, pp. 795–808, 2018.

[123] Z. Guan, H. Hu, X. Shen, P. Xiang, N. Zhong, J. Chu, and C. Duan, "Recent Progress in Two-Dimensional Ferroelectric Materials," *Advanced Electronic Materials*, vol. 6, no. 1, p. 1900818, 2020.

[124] W. J. Xu, S. Kopyl, A. Kholkin, and J. Rocha, "Hybrid organic-inorganic perovskites: Polar properties and applications," *Coordination Chemistry Reviews*, vol. 387, pp. 398–414, 2019.

[125] N. A. Benedek, J. M. Rondinelli, H. Djani, P. Ghosez, and P. Lightfoot, "Understanding ferroelectricity in layered perovskites: New ideas and insights from theory and experiments," *Dalton Transactions*, vol. 44, no. 23, pp. 10543–10558, 2015.

[126] A. Moure, "Review and Perspectives of Aurivillius Structures as a Lead-Free Piezoelectric System," *Applied Sciences*, vol. 8, no. 1, p. 62, 2018.

[127] N. Deepak, P. F. Zhang, L. Keeney, M. E. Pemble, and R. W. Whatmore, "Atomic vapor deposition of bismuth titanate thin films," *Journal of Applied Physics*, vol. 113, no. 187207, p. 187207, 2013.

[128] L. Keeney, Z. Saghi, M. O'Sullivan, J. Alaria, M. Schmidt, and L. Colfer, "Persistence of Ferroelectricity Close to Unit-Cell Thickness in Structurally Disordered Aurivillius Phases," *Chemistry of Materials*, vol. 32, no. 24, pp. 10511–10523, 2020.

[129] J. Lettieri, M. A. Zurbuchen, Y. Jia, D. G. Schlom, S. K. Streiffer, and M. E. Hawley, "Epitaxial growth of $SrBi_2Nb_2O_9$ on (110) $SrTiO_3$ and the establishment of a lower bound on the spontaneous polarization of $SrBi_2Nb_2O$," *Applied Physics Letters*, vol. 77, no. 19, pp. 3090–3092, 2000.

[130] H. N. Lee, D. Hesse, N. Zakharov, and U. Gösele, "Ferroelectric $Bi_{3.25}La_{0.75}Ti_3O_{12}$ films of uniform a-axis orientation on silicon substrates," *Science*, vol. 296, no. 5575, pp. 2006–2009, 2002.

[131] C. Wang, X. Ke, J. Wang, R. Liang, Z. Luo, Y. Tian, D. Yi, Q. Zhang, J. Wang, X. F. Han, G. Van Tendeloo, L. Q. Chen, C. W. Nan, R. Ramesh, and J. Zhang, "Ferroelastic switching in a layered-perovskite thin film," *Nature Communications*, vol. 7, p. 10636, 2016.

[132] J. Jeong, J. Mun, S. Das, J. Kim, J. R. Kim, W. Peng, M. Kim, and T. W. Noh, "Growth and Atomically Resolved Polarization Mapping of Ferroelectric Bi_2WO_6 Thin Films," *ACS Applied Electronic Materials*, vol. 3, no. 2, pp. 1023–1030, 2021.

[133] L. Vasylechko, L. Akselrud, W. Morgenroth, U. Bismayer, A. Matkovskii, and D. Savytskii, "Crystal structure of $NdGaO_3$ at 100 K and 293 K based on synchrotron data," *Journal of Alloys and Compounds*, vol. 297, no. 1-2, pp. 46–52, 2000.

[134] C. H. Hervoches, A. Snedden, R. Riggs, S. H. Kilcoyne, P. Manuel, and P. Lightfoot, "Structural behavior of the four-layer aurivillius-phase ferroelectrics $SrBi_4Ti_4O_{15}$ and $Bi_5Ti_3FeO_{15}$," *Journal of Solid State Chemistry*, vol. 164, no. 2, pp. 280–291, 2002.

[135] S. K. Patri, R. N. Choudhary, and B. K. Samantaray, "Studies of structural, dielectric and impedance properties of $Bi_9Fe_5Ti_3O_{27}$ ceramics," *Journal of Electroceramics*, vol. 20, no. 2, pp. 119–126, 2008.

[136] J. A. Venables, G. D. T. Spiller, and M. Hanbücken, "Nucleation and growth of thin films," *Rep. Prog. Phys.*, vol. 47, pp. 399–459, 1984.

[137] H. Béa, M. Bibes, A. Barthélémy, K. Bouzehouane, E. Jacquet, A. Khodan, J. P. Contour, S. Fusil, F. Wyczisk, A. Forget, D. Lebeugle, D. Colson, and M. Viret, "Influence of parasitic phases on the properties of $BiFeO_3$ epitaxial thin films," *Applied Physics Letters*, vol. 87, no. 7, pp. 3–5, 2005.

[138] L. Xie, L. Li, C. A. Heikes, Y. Zhang, Z. Hong, P. Gao, C. T. Nelson, F. Xue, E. Kioupakis, L. Chen, D. G. Schlom, P. Wang, and X. Pan, "Giant Ferroelectric Polarization in Ultrathin Ferroelectrics via Boundary-Condition Engineering," *Advanced Materials*, vol. 29, p. 1701475, 2017.

[139] A. Snedden, C. H. Hervoches, and P. Lightfoot, "Ferroelectric phase transitions in $SrBi_4Ti_4O_{15}$ and $Bi_5Ti_3FeO_{15}$: A powder neutron diffraction study," *Physical Review B - Condensed Matter and Materials Physics*, vol. 67, no. 9, pp. 3–6, 2003.

[140] K. Moore, E. N. O'Connell, S. M. Griffin, C. Downing, L. Colfer, M. Schmidt, V. Nicolosi, U. Bangert, L. Keeney, and M. Conroy, "Charged Domain Wall and Polar Vortex Topologies in a Room-Temperature Magnetoelectric Multiferroic Thin Film," *ACS Applied Materials Interfaces*, vol. 14, no. 4, pp. 5525–5536, 2022.

[141] R. Nath, S. Hong, J. A. Klug, A. Imre, M. J. Bedzyk, R. S. Katiyar, and O. Auciello, "Effects of cantilever buckling on vector piezoresponse force microscopy imaging of ferroelectric domains in $BiFeO_3$ nanostructures," *Applied Physics Letters*, vol. 96, no. 16, p. 163101, 2010.

[142] D. Meier, J. Seidel, A. Cano, K. Delaney, Y. Kumagai, M. Mostovoy, N. A. Spaldin, R. Ramesh, and M. Fiebig, "Anisotropic conductance at improper ferroelectric domain walls," *Nature Materials*, vol. 11, no. 4, pp. 284–288, 2012.

[143] G. Koster, "Reflection high-energy electron diffraction (rheed) for in situ characterization of thin film growth," in *In Situ Characterization of Thin Film Growth* (G. Rijnders and G. Koster, eds.), pp. 3–28, Cambridge: Woodhead Publishing Limited, 2011.

[144] C. L. Jermain, H. Paik, S. V. Aradhya, R. A. Buhrman, D. G. Schlom, and D. C. Ralph, "Low-damping sub-10-nm thin films of lutetium iron garnet grown by molecular-beam epitaxy," *Applied Physics Letters*, vol. 109, no. 19, p. 192408, 2016.

[145] B. B. Krichevtsov, S. V. Gastev, S. M. Suturin, V. V. Fedorov, A. M. Korovin, V. E. Bursian, A. G. Banshchikov, M. P. Volkov, M. Tabuchi, and N. S. Sokolov,

"Magnetization reversal in YIG/GGG(111) nanoheterostructures grown by laser molecular beam epitaxy," *Science and Technology of Advanced Materials*, vol. 18, no. 1, pp. 351–363, 2017.

[146] J. Nordlander, M. D. Rossell, M. Campanini, M. Fiebig, and M. Trassin, "Epitaxial integration of improper ferroelectric hexagonal YMnO$_3$ thin films in heterostructures," *Physical Review Materials*, vol. 4, no. 12, pp. 1–6, 2020.

[147] S. Homkar, D. Preziosi, X. Devaux, C. Bouillet, J. Nordlander, M. Trassin, F. Roulland, C. Lefèvre, G. Versini, S. Barre, C. Leuvrey, M. Lenertz, M. Fiebig, G. Pourroy, and N. Viart, "Ultrathin regime growth of atomically flat multiferroic gallium ferrite films with perpendicular magnetic anisotropy," *Physical Review Materials*, vol. 3, no. 12, pp. 1–10, 2019.

[148] R. G. Palgrave, P. Borisov, M. S. Dyer, S. R. McMitchell, G. R. Darling, J. B. Claridge, M. Batuk, H. Tan, H. Tian, J. Verbeeck, J. Hadermann, and M. J. Rosseinsky, "Artificial Construction of the Layered Ruddlesden − Popper Manganite La$_2$Sr$_2$Mn$_3$O$_{10}$ by Reflection High Energy Electron Diffraction Monitored Pulsed Laser Deposition," *Journal of the American Chemical Society*, vol. 134, no. 18, pp. 7700–7714, 2012.

[149] Y. F. Nie, Y. Zhu, C. H. Lee, L. F. Kourkoutis, J. A. Mundy, J. Junquera, P. Ghosez, D. J. Baek, S. Sung, X. X. Xi, K. M. Shen, D. A. Muller, and D. G. Schlom, "Atomically precise interfaces from non-stoichiometric deposition," *Nature Communications*, vol. 5, p. 4530, 2014.

[150] S. N. Ruddlesden and P. Popper, "New compounds of the K$_2$NIF$_4$ type," *Acta Crystallographica*, vol. 10, no. 8, pp. 538–539, 1957.

[151] A. J. Jacobson, J. W. Johnson, and J. T. Lewandowski, "Interlayer Chemistry between Thick Transition-Metal Oxide Layers: Synthesis and Intercalation Reactions of K[Ca$_2$Na$_{n-3}$Nb$_n$O$_{3n+1}$] ($3 \leq n \leq 7$)," *Inorganic Chemistry*, vol. 24, no. 23, pp. 3727–3729, 1985.

[152] M. Gajek, M. Bibes, S. Fusil, K. Bouzehouane, J. Fontcuberta, A. Barthélémy, and A. Fert, "Tunnel junctions with multiferroic barriers," *Nature Materials*, vol. 6, no. 4, pp. 296–302, 2007.

[153] J. P. Velev, C. G. Duan, J. D. Burton, A. Smogunov, M. K. Niranjan, E. Tosatti, S. S. Jaswal, and E. Y. Tsymbal, "Magnetic tunnel junctions with ferroelectric barriers: Prediction of four resistance states from first principles," *Nano Letters*, vol. 9, no. 1, pp. 427–432, 2009.

[154] H. Shen, J. Liu, K. Chang, and L. Fu, "In-Plane Ferroelectric Tunnel Junction," *Physical Review Applied*, vol. 11, p. 024048, 2019.

[155] E. Gradauskaite, K. A. Hunnestad, Q. N. Meier, D. Meier, and M. Trassin, "Ferroelectric Domain Engineering Using Structural Defect Ordering," *Chemistry of Materials*, vol. 34, pp. 6468–6475, 2022.

[156] V. Garcia, M. Bibes, L. Bocher, S. Valencia, F. Kronast, A. Crassous, X. Moya, S. Enouz-Vedrenne, A. Gloter, D. Imhoff, C. Deranlot, N. Mathur, S. Fusil, K. Bouzehouane, and A. Barthélémy, "Ferroelectric Control of Spin Polarization," *Science*, vol. 327, no. 5969, pp. 1106–1110, 2010.

[157] D. J. Kim, H. Lu, S. Ryu, C. W. Bark, C. B. Eom, E. Y. Tsymbal, and A. Gruverman, "Ferroelectric tunnel memristor," *Nano Letters*, vol. 12, no. 11, pp. 5697–5702, 2012.

[158] P. Sharma, Q. Zhang, D. Sando, C. H. Lei, Y. Liu, J. Li, V. Nagarajan, and J. Seidel, "Nonvolatile ferroelectric domain wall memory," *Science Advances*, vol. 3, no. 6, p. e1700512, 2017.

[159] P. Sharma, D. Sando, Q. Zhang, X. Cheng, S. Prosandeev, R. Bulanadi, S. Prokhorenko, L. Bellaiche, L. Q. Chen, V. Nagarajan, and J. Seidel, "Conformational Domain Wall Switch," *Advanced Functional Materials*, vol. 29, no. 18, p. 1807523, 2019.

[160] D. Meier, J. Seidel, A. Cano, K. Delaney, Y. Kumagai, M. Mostovoy, N. A. Spaldin, R. Ramesh, and M. Fiebig, "Anisotropic conductance at improper ferroelectric domain walls," *Nature Materials*, vol. 11, no. 4, pp. 284–288, 2012.

[161] J. R. Whyte and J. M. Gregg, "A diode for ferroelectric domain-wall motion," *Nature Communications*, vol. 6, p. 7361, 2015.

[162] L. Feigl, P. Yudin, I. Stolichnov, T. Sluka, K. Shapovalov, M. Mtebwa, C. S. Sandu, X. K. Wei, A. K. Tagantsev, and N. Setter, "Controlled stripes of ultrafine ferroelectric domains," *Nature Communications*, vol. 5, p. 4677, 2014.

[163] M. F. Sarott, M. Fiebig, and M. Trassin, "Tracking ferroelectric domain formation during epitaxial growth of $PbTiO_3$ films," *Applied Physics Letters*, vol. 117, p. 132901, 2020.

[164] L. W. Martin, Y. H. Chu, M. B. Holcomb, M. Huijben, P. Yu, S. J. Han, D. Lee, S. X. Wang, and R. Ramesh, "Nanoscale control of exchange bias with $BiFeO_3$ thin films," *Nano Letters*, vol. 8, no. 7, pp. 2050–2055, 2008.

[165] G. De Luca, M. D. Rossell, J. Schaab, N. Viart, M. Fiebig, and M. Trassin, "Domain Wall Architecture in Tetragonal Ferroelectric Thin Films," *Advanced Materials*, vol. 29, no. 7, p. 1605145, 2017.

[166] P. S. Bednyakov, T. Sluka, A. K. Tagantsev, D. Damjanovic, and N. Setter, "Formation of charged ferroelectric domain walls with controlled periodicity," *Scientific Reports*, vol. 5, pp. 11–14, 2015.

[167] N. Deepak, P. Carolan, L. Keeney, M. E. Pemble, and R. W. Whatmore, "Tunable nanoscale structural disorder in Aurivillius phase, $n = 3$ $Bi_4Ti_3O_{12}$ thin films and their role in the transformation to $n = 4...$," *Journal of Materials Chemistry C*, vol. 3, no. 22, pp. 5727–5732, 2015.

[168] X. K. Wei, A. K. Tagantsev, A. Kvasov, K. Roleder, C. L. Jia, and N. Setter, "Ferroelectric translational antiphase boundaries in nonpolar materials," *Nature Communications*, vol. 5, 2014.

[169] Y. Zhang, M. G. Han, D. Sando, L. Wu, N. Valanoor, and Y. Zhu, "Antiphase-Boundary-Engineered Domain Switching in a (110)-Oriented $BiFeO_3$ Film," *ACS Applied Electronic Materials*, vol. 3, no. 7, pp. 3226–3233, 2021.

[170] J. Kim, J. Mun, C. M. Palomares García, B. Kim, R. S. Perry, Y. Jo, H. Im, H. G. Lee, E. K. Ko, S. H. Chang, S. B. Chung, M. Kim, J. W. Robinson, S. Yonezawa, Y. Maeno, L. Wang, and T. W. Noh, "Superconducting Sr_2RuO_4 Thin Films without Out-of-Phase Boundaries by Higher-Order Ruddlesden-Popper Intergrowth," *Nano Letters*, vol. 21, no. 10, pp. 4185–4192, 2021.

[171] H. Nakajima, K. Kurushima, S. Mine, H. Tsukasaki, M. Matsuoka, B. Gao, S.-W. Cheong, and S. Mori, "Charged domain boundaries stabilized by translational symmetry breaking in the hybrid improper ferroelectric $Ca_{3-x}Sr_xTi_2O_7$," *Communications Materials*, vol. 2, no. 1, p. 109, 2021.

[172] J. C. Jiang, Y. Lin, C. L. Chen, C. W. Chu, and E. I. Meletis, "Microstructures and surface step-induced antiphase boundaries in epitaxial ferroelectric $Ba_{0.6}Sr_{0.4}TiO_3$ thin film on MgO," *Journal of Applied Physics*, vol. 91, no. 5, pp. 3188–3192, 2002.

[173] U. Aschauer, R. Pfenninger, S. M. Selbach, T. Grande, and N. A. Spaldin, "Strain-controlled oxygen vacancy formation and ordering in $CaMnO_3$," *Physical Review B - Condensed Matter and Materials Physics*, vol. 88, no. 5, p. 054111, 2013.

[174] M. Alexe, J. F. Scott, C. Curran, N. D. Zakharov, D. Hesse, and A. Pignolet, "Self-patterning nano-electrodes on ferroelectric thin films for gigabit memory applications," *Applied Physics Letters*, vol. 73, no. 11, pp. 1592–1594, 1998.

[175] C. Park and D. Chadi, "Microscopic study of oxygen-vacancy defects in ferroelectric perovskites," *Physical Review B - Condensed Matter and Materials Physics*, vol. 57, no. 22, p. R13961, 1998.

[176] U. Petralanda, M. Kruse, H. Simons, and T. Olsen, "Oxygen Vacancies Nucleate Charged Domain Walls in Ferroelectrics," *Physical Review Letters*, vol. 127, no. 11, p. 117601, 2021.

[177] M. M. Yang, A. Bhatnagar, Z. D. Luo, and M. Alexe, "Enhancement of Local Photovoltaic Current at Ferroelectric Domain Walls in $BiFeO_3$," *Scientific Reports*, vol. 7, no. February, p. 43070, 2017.

[178] B. B. Yang, D. P. Song, R. H. Wei, X. W. Tang, L. Hu, J. Yang, W. H. Song, J. M. Dai, X. B. Zhu, and Y. P. Sun, "Ni doping dependent dielectric, leakage, ferroelectric and magnetic properties in $Bi_7Fe_{3-x}Ni_xTi_3O_{21}$ thin films," *Applied Surface Science*, vol. 440, pp. 484–490, 2018.

[179] M. A. Zurbuchen, G. Asayama, D. G. Schlom, and S. K. Streiffer, "Ferroelectric Domain Structure of $SrBi_2Nb_2O_9$ Epitaxial Thin Films," *Physical Review Letters*, vol. 88, no. 10, p. 107601, 2002.

[180] A. K. Yadav, C. T. Nelson, S. L. Hsu, Z. Hong, J. D. Clarkson, C. M. Schlepuëtz, A. R. Damodaran, P. Shafer, E. Arenholz, L. R. Dedon, D. Chen, A. Vishwanath, A. M. Minor, L. Q. Chen, J. F. Scott, L. W. Martin, and R. Ramesh, "Observation of polar vortices in oxide superlattices," *Nature*, vol. 530, no. 7589, pp. 198–201, 2016.

[181] N. Strkalj, M. Bernet, M. F. Sarott, J. Schaab, T. Weber, M. Fiebig, and M. Trassin, "Stabilization and manipulation of in-plane polarization in a ferroelectric|dielectric superlattice," *Journal of Applied Physics*, vol. 129, no. 17, 2021.

[182] J. Schaab, S. H. Skjærvø, S. Krohns, X. Dai, M. E. Holtz, A. Cano, M. Lilienblum, Z. Yan, E. Bourret, D. A. Muller, M. Fiebig, S. M. Selbach, and D. Meier, "Electrical half-wave rectification at ferroelectric domain walls," *Nature Nanotechnology*, vol. 13, no. 11, pp. 1028–1034, 2018.

[183] Y. Tokura, *Colossal Magnetoresistive Oxides.* Boca Raton: CRC Press, 2000.

[184] S. R. Spurgeon, J. D. Sloppy, D. M. Kepaptsoglou, P. V. Balachandran, S. Nejati, J. Karthik, A. R. Damodaran, C. L. Johnson, H. Ambaye, R. Goyette, V. Lauter, Q. M. Ramasse, J. C. Idrobo, K. K. S. Lau, S. E. Lofland, J. M. Rondinelli, L. W. Martin, and M. L. Taheri, "Thickness-dependent crossover from charge-to strain-mediated magnetoelectric coupling in ferromagnetic/piezoelectric oxide heterostructures," *ACS Nano*, vol. 8, no. 1, pp. 894–903, 2014.

[185] D. Pesquera, G. Herranz, A. Barla, E. Pellegrin, F. Bondino, E. Magnano, F. Sánchez, and J. Fontcuberta, "Surface symmetry-breaking and strain effects

on orbital occupancy in transition metal perovskite epitaxial films," *Nature Communications*, vol. 3, pp. 1–7, 2012.

[186] E. J. Moon, P. V. Balachandran, B. J. Kirby, D. J. Keavney, R. J. Sichel-Tissot, C. M. Schlepütz, E. Karapetrova, X. M. Cheng, J. M. Rondinelli, and S. J. May, "Effect of interfacial octahedral behavior in ultrathin manganite films," *Nano Letters*, vol. 14, no. 5, pp. 2509–2514, 2014.

[187] Z. Liao, M. Huijben, Z. Zhong, N. Gauquelin, S. Macke, R. J. Green, S. Van Aert, J. Verbeeck, G. Van Tendeloo, K. Held, G. A. Sawatzky, G. Koster, and G. Rijnders, "Controlled lateral anisotropy in correlated manganite heterostructures by interface-engineered oxygen octahedral coupling," *Nature Materials*, vol. 15, no. 4, pp. 425–431, 2016.

[188] M. Huijben, G. Koster, Z. L. Liao, and G. Rijnders, "Interface-engineered oxygen octahedral coupling in manganite heterostructures," *Applied Physics Reviews*, vol. 4, no. 4, pp. 0–23, 2017.

[189] P. Perna, L. Méchin, M. Saïb, J. Camarero, and S. Flament, "Imaging the magnetization reversal of step-induced uniaxial magnetic anisotropy in vicinal epitaxial $La_{0.7}Sr_{0.3}MnO_3$ films," *New Journal of Physics*, vol. 12, p. 103033, 2010.

[190] P. Perna, D. Maccariello, F. Ajejas, R. Guerrero, L. Méchin, S. Flament, J. Santamaria, R. Miranda, and J. Camarero, "Engineering Large Anisotropic Magnetoresistance in $La_{0.7}Sr_{0.3}MnO_3$ Films at Room Temperature," *Advanced Functional Materials*, vol. 27, no. 26, p. 1700664, 2017.

[191] J. Santiso, L. Balcells, Z. Konstantinovic, J. Roqueta, P. Ferrer, A. Pomar, B. Martínez, and F. Sandiumenge, "Thickness evolution of the twin structure and shear strain in LSMO films," *CrystEngComm*, vol. 15, no. 19, pp. 3908–3918, 2013.

[192] B. Paudel, K. T. Kang, Y. Sharma, H. Nakotte, D. Yarotski, and A. Chen, "Symmetry mismatch controlled ferroelastic domain ordering and the functional properties of manganite films on cubic miscut substrates," *Physical Chemistry Chemical Physics*, vol. 23, no. 31, pp. 16623–16628, 2021.

[193] D. Lan, P. Chen, C. Liu, X. Wu, P. Yang, X. Yu, J. Ding, J. Chen, and G. M. Chow, "Interfacial control of domain structure and magnetic anisotropy in $La_{0.67}Sr_{0.33}MnO_3$ manganite heterostructures," *Physical Review B*, vol. 104, no. 12, 2021.

[194] Z. Wang, H. Guo, S. Shao, M. Saghayezhian, J. Li, R. Fittipaldi, A. Vecchione, P. Siwakoti, Y. Zhu, J. Zhang, and E. W. Plummer, "Designing antiphase bound-

aries by atomic control of heterointerfaces," *Proceedings of the National Academy of Sciences of the United States of America*, vol. 115, no. 38, pp. 9485–9490, 2018.

[195] B. J. Lin, "Optical lithography-present and future challenges," *Comptes Rendus Physique*, vol. 7, no. 8, pp. 858–874, 2006.

[196] C. Li, G. Habler, L. C. Baldwin, and R. Abart, "An improved FIB sample preparation technique for site-specific plan-view specimens: A new cutting geometry," *Ultramicroscopy*, vol. 184, pp. 310–317, 2018.

[197] D. J. Wallis, N. D. Browning, S. Sivananthan, P. D. Nellist, and S. J. Pennycook, "Atomic layer graphoepitaxy for single crystal heterostructures," *Applied Physics Letters*, vol. 70, no. 23, p. 3113, 1997.

[198] G. Sanchez-Santolino, J. Tornos, D. Hernandez-Martin, J. I. Beltran, C. Munuera, M. Cabero, A. Perez-Muñoz, J. Ricote, F. Mompean, M. Garcia-Hernandez, Z. Sefrioui, C. Leon, S. J. Pennycook, M. C. Muñoz, M. Varela, and J. Santamaria, "Resonant electron tunnelling assisted by charged domain walls in multiferroic tunnel junctions," *Nature Nanotechnology*, vol. 12, no. 7, pp. 655–662, 2017.

[199] L. Keeney, R. J. Smith, M. Palizdar, M. Schmidt, A. J. Bell, J. N. Coleman, and R. W. Whatmore, "Ferroelectric Behavior in Exfoliated 2D Aurivillius Oxide Flakes of Sub-Unit Cell Thickness," *Advanced Electronic Materials*, vol. 6, p. 1901264, 2020.

[200] R. J. Zeches, M. D. Rossell, J. X. Zhang, A. J. Hatt, Q. He, C.-H. Yang, A. Kumar, C. H. Wang, A. Melville, C. Adamo, G. Sheng, Y.-H. Chu, J. F. Ihlefeld, R. Erni, C. Ederer, V. Gopalan, L. Q. Chen, D. G. Schlom, N. A. Spaldin, L. W. Martin, and R. Ramesh, "A Strain-Driven Morphotropic Phase Boundary in BiFeO$_3$," *Science*, vol. 326, no. 5955, p. 977, 2009.

[201] J. Nordlander, A. Maillard, M. Fiebig, and M. Trassin, "Emergence of ferroelectricity at the morphotropic phase boundary of ultrathin BiFeO$_3$," *ArXiv*, 2020.

[202] P. Gao, Z. Zhang, M. Li, R. Ishikawa, B. Feng, H. J. Liu, Y. L. Huang, N. Shibata, X. Ma, S. Chen, J. Zhang, K. Liu, E. G. Wang, D. Yu, L. Liao, Y. H. Chu, and Y. Ikuhara, "Possible absence of critical thickness and size effect in ultrathin perovskite ferroelectric films," *Nature Communications*, vol. 8, p. 15549, 2017.

[203] C. Gattinoni, N. Strkalj, R. Härdi, M. Fiebig, M. Trassin, and N. A. Spaldin, "Interface and surface stabilization of the polarization in ferroelectric thin films," *Proceedings of the National Academy of Sciences of the United States of America*, vol. 117, no. 46, pp. 28589–28595, 2020.

[204] D. Puggioni, G. Giovannetti, and J. M. Rondinelli, "Polar metals as electrodes to suppress the critical-thickness limit in ferroelectric nanocapacitors," *Journal of Applied Physics*, vol. 124, no. 17, p. 174102, 2018.

[205] W. X. Zhou and A. Ariando, "Review on ferroelectric/polar metals," *Japanese Journal of Applied Physics*, vol. 59, p. SI0802, 2020.

[206] Y. S. Kim, D. H. Kim, J. D. Kim, Y. J. Chang, T. W. Noh, J. H. Kong, K. Char, Y. D. Park, S. D. Bu, J. G. Yoon, and J. S. Chung, "Critical thickness of ultrathin ferroelectric $BaTiO_3$ films," *Applied Physics Letters*, vol. 86, no. 10, p. 102907, 2005.

[207] D. D. Fong, G. B. Stephenson, S. K. Streiffer, J. A. Eastman, O. Auciello, P. H. Fuoss, and C. Thompson, "Ferroelectricity in ultrathin perovskite films," *Science*, vol. 304, no. 5677, pp. 1650–1653, 2004.

[208] D. A. Tenne, P. Turner, J. D. Schmidt, M. Biegalski, Y. L. Li, L. Q. Chen, A. Soukiassian, S. Trolier-Mckinstry, D. G. Schlom, X. X. Xi, D. D. Fong, P. H. Fuoss, J. A. Eastman, G. B. Stephenson, C. Thompson, and S. K. Streiffer, "Ferroelectricity in ultrathin $BaTiO_3$ films: Probing the size effect by ultraviolet raman spectroscopy," *Physical Review Letters*, vol. 103, no. 17, 2009.

[209] L. Keeney, Z. Saghi, M. O'Sullivan, J. Alaria, M. Schmidt, and L. Colfer, "Persistence of Ferroelectricity Close to Unit-Cell Thickness in Structurally Disordered Aurivillius Phases," *Chemistry of Materials*, vol. 32, no. 24, pp. 10511–10523, 2020.

[210] Y. Ishibashi and E. Salje, "A Theory of Ferroelectric 90 Degree Domain Wall," *Journal of the Physical Society of Japan*, vol. 71, no. 11, pp. 2800–2803, 2002.

[211] F. Lichtenberg, A. Herrnberger, K. Wiedenmann, and J. Mannhart, "Synthesis of perovskite-related layered $A_nB_nO_{3n+2} = ABO_X$ type niobates and titanates and study of their structural, electric and magnetic properties," *Progress in Solid State Chemistry*, vol. 29, no. 1-2, pp. 1–70, 2001.

[212] M. Núñez Valdez and N. A. Spaldin, "Origin and evolution of ferroelectricity in the layered rare-earth-titanate, $R_2Ti_2O_7$, Carpy-Galy phases," *Polyhedron*, vol. 171, pp. 181–192, 2019.

[213] H. J. Zhao, P. Chen, S. Prosandeev, S. Artyukhin, and L. Bellaiche, "Dzyaloshinskii–Moriya-like interaction in ferroelectrics and antiferroelectrics," *Nature Materials*, vol. 20, no. 3, pp. 341–345, 2021.

[214] S. Cherifi-Hertel, H. Bulou, R. Hertel, G. Taupier, K. D. H. Dorkenoo, C. Andreas, J. Guyonnet, I. Gaponenko, K. Gallo, and P. Paruch, "Non-Ising and

chiral ferroelectric domain walls revealed by nonlinear optical microscopy," *Nature Communications*, vol. 8, p. 15768, 2017.

[215] X. K. Wei, C. L. Jia, T. Sluka, B. X. Wang, Z. G. Ye, and N. Setter, "Néel-like domain walls in ferroelectric Pb(Zr,Ti)O$_3$ single crystals," *Nature Communications*, vol. 7, p. 12385, 2016.

[216] Z. Hong, S. Das, C. Nelson, A. Yadav, Y. Wu, J. Junquera, L. Q. Chen, L. W. Martin, and R. Ramesh, "Vortex Domain Walls in Ferroelectrics," *Nano Letters*, vol. 21, no. 8, pp. 3533–3539, 2021.

[217] I. E. Dzyaloshinskii, "Theory of Helicoidal Structures in Antiferromagnets. I. Nonmetals," *Jetp*, vol. 19, no. 4, pp. 960–971, 1964.

[218] A. N. Bogdanov, U. K. Rößler, M. Wolf, and K. H. Müller, "Magnetic structures and reorientation transitions in noncentrosymmetric uniaxial antiferromagnets," *Physical Review B - Condensed Matter and Materials Physics*, vol. 66, no. 21, p. 214410, 2002.

[219] L. D. Landau and E. M. Lifshitz, *Statistical Physics: Volume 5.* Oxford: Pergamon Press, 2nd ed., 1969.

[220] U. K. Rößler, A. N. Bogdanov, and C. Pfleiderer, "Spontaneous skyrmion ground states in magnetic metals," *Nature*, vol. 442, no. 7104, pp. 797–801, 2006.

[221] I. E. Dzyaloshinskii, "A Thermodynamic Theory of "weak" ferromagnetism of antiferromagnetics," *J. Phys. Chem. Solids*, vol. 4, pp. 241–255, 1958.

[222] A. Crépieux and C. Lacroix, "Dzyaloshinsky-Moriya interactions induced by symmetry breaking at a surface," *Journal of Magnetism and Magnetic Materials*, vol. 182, no. 3, pp. 341–349, 1998.

[223] S. Vélez, J. Schaab, M. S. Wörnle, M. Müller, E. Gradauskaite, P. Welter, C. Gutgsell, C. Nistor, C. L. Degen, M. Trassin, M. Fiebig, and P. Gambardella, "High-speed domain wall racetracks in a magnetic insulator," *Nature Communications*, vol. 10, p. 4750, 2019.

[224] M. A. Goncalves, C. Escorihuela-Sayalero, P. Garcia-Fernandez, J. Junquera, and J. Iniguez, "Theoretical guidelines to create and tune electric skyrmions," *Science Advances*, vol. 5, p. eaau7023, 2019.

[225] K. C. Erb and J. Hlinka, "Vector, bidirector, and Bloch skyrmion phases induced by structural crystallographic symmetry breaking," *Physical Review B*, vol. 102, no. 2, p. 024110, 2020.

[226] J.-Y. Chauleau, T. Chirac, S. Fusil, V. Garcia, W. Akhtar, J. Tranchida, P. Thibaudeau, I. Gross, C. Blouzon, A. Finco, M. Bibes, B. Dkhil, D. D. Khalyavin, P. Manuel, V. Jacques, N. Jaouen, and M. Viret, "Electric and antiferromagnetic chiral textures at multiferroic domain walls," *Nature Materials*, vol. 19, no. 4, pp. 386–390, 2020.

[227] S. Fusil, J.-Y. Chauleau, X. Li, J. Fischer, P. Dufour, C. Léveillé, C. Carrétéro, N. Jaouen, M. Viret, A. Gloter, and V. Garcia, "Polar Chirality in $BiFeO_3$ Emerging from A Peculiar Domain Wall Sequence," *Advanced Electronic Materials*, vol. 2101155, p. 2101155, 2022.

[228] A. Fert, V. Cros, and J. Sampaio, "Skyrmions on the track," *Nature Nanotechnology*, vol. 8, no. 3, pp. 152–156, 2013.

[229] S. Vélez, S. Ruiz-Gómez, J. Schaab, E. Gradauskaite, M. S. Wörnle, P. Welter, B. J. Jacot, C. L. Degen, M. Trassin, M. Fiebig, and P. Gambardella, "Current-driven dynamics and ratchet effect of skyrmion bubbles in a ferrimagnetic insulator," *Nature Nanotechnology*, vol. 17, pp. 834–841, 2022.

[230] Y. Zhang, J. Wang, M. P. Sahoo, T. Shimada, and T. Kitamura, "Strain-induced ferroelectricity and lattice coupling in $BaSnO_3$ and $SrSnO_3$," *Physical Chemistry Chemical Physics*, vol. 19, no. 38, pp. 26047–26055, 2017.

[231] I. Gross, W. Akhtar, V. Garcia, L. J. Martínez, S. Chouaieb, K. Garcia, C. Carrétéro, A. Barthélémy, P. Appel, P. Maletinsky, J. V. Kim, J. Y. Chauleau, N. Jaouen, M. Viret, M. Bibes, S. Fusil, and V. Jacques, "Real-space imaging of non-collinear antiferromagnetic order with a single-spin magnetometer," *Nature*, vol. 549, no. 7671, pp. 252–256, 2017.

[232] C. A. Vaz, "Electric field control of magnetism in multiferroic heterostructures," *Journal of Physics Condensed Matter*, vol. 24, no. 33, 2012.

[233] J. R. Whyte, R. G. McQuaid, P. Sharma, C. Canalias, J. F. Scott, A. Gruverman, and J. M. Gregg, "Ferroelectric domain wall injection," *Advanced Materials*, vol. 26, no. 2, pp. 293–298, 2014.

[234] P. Sharma, Q. Zhang, D. Sando, C. H. Lei, Y. Liu, J. Li, V. Nagarajan, and J. Seidel, "Nonvolatile ferroelectric domain wall memory," *Science Advances*, vol. 3, no. 6, pp. 1–9, 2017.

[235] Y. Tokura, "Critical features of colossal magnetoresistive manganites," *Reports on Progress in Physics*, vol. 69, no. 3, pp. 797–851, 2006.

[236] J. D. Burton and E. Y. Tsymbal, "Prediction of electrically induced magnetic reconstruction at the manganite/ferroelectric interface," *Physical Review B - Condensed Matter and Materials Physics*, vol. 80, no. 17, p. 174406, 2009.

[237] J. M. Rondinelli, M. Stengel, and N. A. Spaldin, "Carrier-mediated magnetoelectricity in complex oxide heterostructures," *Nature Nanotechnology*, vol. 3, no. 1, pp. 46–50, 2008.

[238] I. V. Ovchinnikov and K. L. Wang, "Theory of electric-field-controlled surface ferromagnetic transition in metals," *Physical Review B - Condensed Matter and Materials Physics*, vol. 79, no. 2, p. 020402(R), 2009.

[239] H. Lu, T. A. George, and Y. Wang, "Electric modulation of magnetization at the $BaTiO_3$ / $La_{0.67}Sr_{0.33}MnO_3$ interfaces," *Applied Physics Letters*, vol. 100, p. 232904, 2012.

[240] S. R. Spurgeon, P. V. Balachandran, D. M. Kepaptsoglou, A. R. Damodaran, J. Karthik, S. Nejati, L. Jones, H. Ambaye, V. Lauter, Q. M. Ramasse, K. K. Lau, L. W. Martin, J. M. Rondinelli, and M. L. Taheri, "Polarization screening-induced magnetic phase gradients at complex oxide interfaces," *Nature Communications*, vol. 6, p. 6735, 2015.

[241] T. L. Meyer, A. Herklotz, V. Lauter, J. W. Freeland, J. Nichols, E. J. Guo, S. Lee, T. Z. Ward, N. Balke, S. V. Kalinin, M. R. Fitzsimmons, and H. N. Lee, "Enhancing interfacial magnetization with a ferroelectric," *Physical Review B*, vol. 94, p. 174432, 2016.

[242] Z. Liao, N. Gauquelin, R. J. Green, S. Macke, J. Gonnissen, S. Thomas, Z. Zhong, L. Li, L. Si, S. Van Aert, P. Hansmann, K. Held, J. Xia, J. Verbeeck, G. Van Tendeloo, G. A. Sawatzky, G. Koster, M. Huijben, and G. Rijnders, "Thickness Dependent Properties in Oxide Heterostructures Driven by Structurally Induced Metal–Oxygen Hybridization Variations," *Advanced Functional Materials*, vol. 27, no. 17, pp. 1–9, 2017.

[243] P. Chen, Z. Huang, C. Li, B. Zhang, N. Bao, P. Yang, X. Yu, S. Zeng, C. Tang, X. Wu, J. Chen, J. Ding, S. J. Pennycook, A. Ariando, T. V. Venkatesan, and G. M. Chow, "Binary Controls on Interfacial Magnetism in Manganite Heterostructures," *Advanced Functional Materials*, vol. 28, no. 33, 2018.

[244] M. Huijben, L. W. Martin, Y. H. Chu, M. B. Holcomb, P. Yu, G. Rijnders, D. H. Blank, and R. Ramesh, "Critical thickness and orbital ordering in ultrathin $La_{0.7}Sr_{0.3}MnO_3$ films," *Physical Review B - Condensed Matter and Materials Physics*, vol. 78, no. 9, p. 094413, 2008.

[245] N. Strkalj, G. De Luca, M. Campanini, S. Pal, J. Schaab, C. Gattinoni, N. A. Spaldin, M. D. Rossell, M. Fiebig, and M. Trassin, "Depolarizing-Field Effects in Epitaxial Capacitor Heterostructures," *Physical Review Letters*, vol. 123, no. 14, p. 147601, 2019.

[246] Z. Fang, I. V. Solovyev, and K. Terakura, "Phase diagram of tetragonal manganites," *Physical Review Letters*, vol. 84, no. 14, pp. 3169–3172, 2000.

[247] H. Boschker, J. Verbeeck, R. Egoavil, S. Bals, G. Van Tendeloo, M. Huijben, E. P. Houwman, G. Koster, D. H. A. Blank, and G. Rijnders, "Preventing the reconstruction of the polar discontinuity at oxide heterointerfaces," *Advanced Functional Materials*, vol. 22, no. 11, pp. 2235–2240, 2012.

[248] A. Tebano, C. Aruta, S. Sanna, P. G. Medaglia, G. Balestrino, A. A. Sidorenko, R. De Renzi, G. Ghiringhelli, L. Braicovich, V. Bisogni, and N. B. Brookes, "Evidence of orbital reconstruction at interfaces in ultrathin $La_{0.67}Sr_{0.33}MnO_3$ Films," *Physical Review Letters*, vol. 100, no. 13, pp. 2–5, 2008.

Data accessibility

Data presented in this thesis is archived in the Ferroic Results directory at:
\3-PhD\2022\EGradauskaite\Data

A zipped archive is also available in ETH Zurich's Research Collection. The folders are organized according to the chapters of the thesis. Illustrations are provided as png files. Where applicable, the Origin file and the dat file containing the plotted data are provided.

Elzbieta Gradauskaite | CV

Vladimir-Prelog-Weg 4, HCI E 482.2, 8093 Zürich, Switzerland

✉ elzbieta.gradauskaite@mat.ethz.ch   •   Born on 02.08.1993

Education

ETH Zürich (Switzerland)   **2018–2022**

Doctoral Studies, Department of Materials   *Zürich*

PhD Thesis: *"Interfacial Control of Ferroic Order in Oxide Heterostructures"*

Supervisor: Prof. Manfred Fiebig, Prof. Morgan Trassin

Research group: Multifunctional Ferroic Materials

University of St Andrews (UK)   **2012–2017**

MSci (Hons) Chemistry and Physics   *St Andrews*

with Honours of the First Class

Master Thesis (MSci): *"Pd doped $PbTiO_3$: Room Temperature Magnetoelectric Multiferroic"*

Supervisor: Prof. James F. Scott

Grade Point Average: 18.4 / 20.0

Vilnius Lyceum (Lithuania)   **2007–2012**

High School   *Vilnius*

Grade Point Average: 9.9 / 10.0

Employment History

ETH Zürich (Switzerland)   **January 2018–December 2022**

PhD student/Research assistant   *Zürich*

Supervisor: Prof. Manfred Fiebig, Prof. Morgan Trassin

○ The growth of ferroic oxide thin films and heterostructures by pulsed laser deposition. In-situ monitoring using optical second harmonic generation and reflection high-energy electron diffraction.

○ Structural characterization with X-ray diffraction, scanning probe microscopy.

○ Functional characterization using electrical and magnetic measurements down to cryogenic temperature.

IT'IS Foundation (Switzerland)   **October 2017–December 2017**

Research Intern   *Zürich*

Supervisor: Dr. Myles H. Capstick

○ Development and testing of systems for measuring dielectric properties of conductive liquids in the low frequency regime using multi-electrode techniques.

○ Prior to the measurements, electromagnetic fields were simulated using Sim4Life platform.

○ Designed software for FFT-based electrochemical impedance spectroscopy using Python.

Paul Scherrer Institute (Switzerland)   **July 2017–September 2017**

Research assistant   *Villigen*

Supervisor: Prof. Thomas Jung

○ Investigation of self-assembly and magnetic order of 2D spin lattices on surfaces.

○ Sample preparation in ultra-high vacuum and characterization using X-ray photoelectron spectroscopy (XPS), scanning tunneling microscopy (STM), X-ray Absorption Spectroscopy (XAS) and X-ray magnetic circular dichroism (XMCD).

German Electron Synchrotron (DESY) (Germany)   **July 2016–September 2016**
Internship in X-ray Physics and Nanoscience Group (DESY Nanolab)   *Hamburg*
Supervisor: Dr. Heshmat Noei
- Practical project on alumina supported platinum nanoparticle system, investigated by carbon monoxide and indole adsorption at cryogenic temperatures in ultra-high vacuum.
- Techniques used included Auger Electron Spectroscopy (AES), XPS and Infrared Reflection-Absorption Spectroscopy (IRRAS).
- Attended 8-week lecture course on Photon Science and Particle Physics.

Helmholtz-Centre Dresden-Rossendorf (HZDR) (Germany)   **May 2016–July 2016**
Internship at the Elbe positron source, Positron Annihilation Beamline   *Dresden*
Supervisor: Dr. Oskar Liedke
- Practical work in the beamlines of the Elbe Positron Source.
- Project on chemical disorder induced magnetism in $Fe_{60}Al_{40}$ and its reversibility.
- Sample preparation using different annealing techniques and sample characterization with SPM, magneto-optic Kerr effect (MOKE) and Positron Annihilation Spectroscopy.

Swiss Light Source (Paul Scherrer Institute) (Switzerland)   **June 2015–August 2015**
Internship at X-treme Beamline   *Villigen*
Supervisor: Dr. Jan Dreiser
- Experimental project on properties of the functionalized Erbium single-ion magnets deposited on metallic surfaces.
- Spatial and magnetic properties were investigated at low temperatures and high magnetic fields.
- Samples were prepared under ultra-high vacuum and characterized using STM and spectroscopic techniques available at the beamline: XAS and XMCD/XNLD.

Teaching activities

Lab Course for second-semester materials science students   **2022 spring semester**
Material Characterization II. Scanning probe microscopy.   *ETH Zürich*

Supervision of Master student semester project   **2021 spring semester**
Natascha Gray, "Growth of thin films of the Aurivillius homologues"   *ETH Zürich*

Teaching assistant for Master course in Physics   **2020 spring semester**
"Crystal optics in intense light fields"   *ETH Zürich*

Supervision of Master student semester project   **2019 spring semester**
Pascal Studer, "Growth of Bi_2WO_6 thin flms"   *ETH Zürich*

Teaching assistant for Master course in Materials Science   **2019–2021**
"Multifunctional ferroic materials: growth and characterisation"   *ETH Zürich*

Lab Course for fifth-semester materials science students   **2018 fall semester**
Praktikum V. Growth and characterization of ferroelectric thin films.   *ETH Zürich*

Awards and Honors

Shortlisted as ISAF Ferroelectric Young Investigator Speaker   **2022**
International Symposium on Applications of Ferroelectrics 2022, Tours

Best poster award at ISOE 2021   **2021**
International School of Oxide Electronics 2021, Cargèse

Best oral presentation award at EMA 2020   **2020**
Conference of Electronic Materials and Applications (The American Ceramics Society), Orlando

MPhys Project Prize   **2017**
Awarded for the best Master's project in Physics.

Europe Winner of the International Undergraduate Awards   **2017**
For Master thesis chosen as the best in Europe in the category of Mathematics and Physics

Brewster Prize   **2017**
Awarded for the best graduating student in Physics

Forrester Prize   **2017**
Awarded for the best graduating student in Chemistry

The Principal's Scholarship for Academic Excellence   **2017**
Awarded to the fifty final-year students across the University whose grades are the highest

Neil Arnott prize   **2016**
Awarded to the most outstanding student in fourth-year Physics

Elizabeth Soutar prize   **2015**
Awarded to the best student in third-year Chemistry

Placed on the Deans' List for academic excellence   **Every term 2012-2017**
Awarded to undergraduate students who achieve an outstanding overall result